UNIVERSITY OF CALIFORNIA

SANTA BARBARA

MOCVD Growth and Electrical Characterization of AlInGaN Heterojunctions

A dissertation submitted in partial satisfaction of the

requirements for the degree of

Doctor of Philosophy

in

Electrical and Computer Engineering

by

Matthew A. Laurent

Committee in charge:
Professor Umesh K. Mishra, *Chair*
Professor Steven P. DenBaars
Professor Arthur C. Gossard
Dr. Stacia Keller

March 2016

The dissertation of

Matthew A. Laurent is approved:

_____

Prof. Steven P. DenBaars

_____

Prof. Arthur C. Gossard

_____

Dr. Stacia Keller

_____

Prof. Umesh K. Mishra, *Committee Chair*

December 2015

MOCVD Growth and Electrical Characterization of AlInGaN Heterojunctions

by

Matthew A. Laurent

This thesis is dedicated to my parents Arthur and Elaine Laurent, and the memory of my grandparents: Nono and Nona (Pierre and Alice). I love you all.

ACKNOWLEDGMENTS

I consider myself very fortunate to have been a part of a truly wonderful group of friends, colleagues, and research group over the past six and a half years. Over this time, many people have helped me get to where I am today, or lent their wisdom to me so that I may succeed. First of all, I would like to thank my advisor and committee. Umesh has a unique personality that combines infectious excitement with strong resolve in the face of steep challenges, and he seems to impart these important traits unto his students. He has been much more than advisor to me over the years – he has been a mentor who has encouraged me to succeed, and also always made me feel as if my problems, regardless of size, were important. I owe him many thanks that I can't hope to repay, so I will instead do my best to pay it forward. I think he'd like that more, anyway.

Now on to the rest of my committee. Stacia Keller was practically a second advisor to me. She is an undeniable force in the field of MOCVD, which is coupled with an undeniable laugh and indefatigable positivity. I've learned so much from her that extended far beyond the field of MOCVD. Her insight into designing intelligent experiments has had a far reaching impact to every experiment I've done, and her influence can be found on every page of this thesis. Beyond that, she has always provided insight into the areas that surrounded my life in grad school: remaining persistent in the face of broken lab equipment and dealing with the uncertainty of breaking new scientific ground. Thank you, Stacia.

I would like to thank the rest of my committee, Professors Steven DenBaars and Arthur Gossard. Steve, aside from outfitting an impressive crystal growth lab, was particularly instrumental at the beginning stages of my project. His intuition for MOCVD and his clued-in nature to the state-of-the-art helped guide me when my project was still very ill-defined.

Professor Gossard and I did not become acquainted until my qualifying exam, but since then he has been a wealth of knowledge and wisdom. The discussion sections in each chapter can be attributed to his perspective on scientific publishing. His astute observations, and my opportunities to discuss my research with him, propelled me to think longer and harder about my results than I would have without his influence.

Next I would like to thank my closest colleagues from the Mishra Group. Geetak and Trey, you guys helped me think through some truly confusing results. On top of that, not everyone has the luxury of being good friends with their closest colleagues. Inside the lab and out, it was always fun to be with you guys (even if temperature-dependent measurements are no fun at all). I also need to thank Geetak for all of his help with device fabrication, and Trey for his help with quantum mechanical simulations. To include Elaheh and Haoran in this would complete the HET Team! As a team, we all had a solid 1.5 years of collaboration and feedback that was so effective, we often predicted and preempted project goals (not to mention Umesh's expectations). We all ran together as a well-oiled machine, and it has been so much fun.

Many of my other group mates provided me with some critical assistance throughout the years. When I was first beginning, Carl Neufeld took me under his wing, which was fortunate, because I was clueless. I feel very lucky to still be close friends with him today, and that he's still willing to sit through practice runs of my conference presentations! Dan Denninghoff taught me how to take imperfect data and fill in the gaps to make it publication worthy. He helped me increase the thoroughness of my experimental work, which resulted in my first conference presentation back in 2011. Srabanti Chowdhury has always been influential to me, from the early days when she was my Device Physics TA to now when we can have hours-long conversations about device engineering and solid state physics.

More recently, I need to thank Steven Wienecke, Onur Koksaldi, and Matt Guidry for critical help with my experiments. Outside the cleanroom, the Mishra group is always fun. Jeong would never turn me down when I suggested it was coffee time, and I think she doesn't realize just how important this was to me. Joking around with her in the office, and discussing the peculiar nature of grad student life kept me going even when my research wasn't going anywhere. Cory, Silvia, Brian, Maher, Davide, Chirag – all of you were great to bounce ideas off of, but it was always more fun when our conversations would go wildly off-topic. You guys are actually a major reason why I wrote 95% of my thesis over at Goleta Coffee!

I also want to give a direct nod to the growers I spent most of my time with: Haoran, Silvia, Cory, Anchal, Humberto, Alex, Dan, Roy, Stacy, and Erin. There's an unusual kind of bond you build with people that are pulling the same crazy hours right alongside you, and struggling through similar problems. Roy taught me all of the hands-on skills that I still use today in the MOCVD lab. Haoran and Silvia – it was always entertaining to cross paths with you at odd hours in the early morning. Silvia, your free food detection skills are legendary. To Erin: it was satisfying to see our research efforts overlap so closely toward the end of our PhD work. I spent most of my PhD working on things alone and often felt adrift, so this meant a lot to me. David Whitlatch and I have spent countless hours troubleshooting and repairing the Veeco MOCVD reactor, and became good friends in the process (misery loves company, I guess). We took on some truly enormous projects together, but always managed to keep it fun and come out on the other side of it.

Outside of work, I had a fantastic group of friends to grill up steaks, cook turduckens, make killer pasta sauces, ride bikes, blow up water jugs with, and more. I need to increase my brevity here, so if you know what the Chalet is then you know who you are. My friends are

invaluable to me, as are my roommates. Mike and Joe, there's not much to say here that hasn't been said between us. Having your best buds at home to de-stress or work through problems with is one of the best things I could have hoped for. Joe and I met each other on our initial flight in to Santa Barbara in February 2009, and met Mike that same weekend. I shudder to think of what it would be like if it turned out any different.

Now on to my family and loved ones. I'm almost done, I swear! Matt and Mitch, you're like brothers to me. You guys are awesome for traveling so far to come see my defense, and for taking a vested interest in my successes, as I am in yours. Myley, you complement my pragmatism with unbridled optimism. There are so many intangible things about you that I appreciate. To sum it up accurately: I appreciate being around you, and everything that brings into my life. Mom and Dad, wow, I could fill another full chapter just talking about you two. Ever since I was thirteen and you encouraged me to apply to this scientific research elective in high school, you've always seen a potential in me that I didn't know was there. You made me want to put the hard work into the things I do. You answered the phone at 3 a.m. when I couldn't sleep because I was too worried about my work. You sacrificed for me in ways that I only recently started to understand. But even better than all that is sharing my success with you, and how much fun we have together. I love you.

CURRICULUM VITAE

Education

January 2015	Ph.D. University of California, Santa Barbara Electrical and Computer Engineering
June 2011	M.S. University of California, Santa Barbara Electrical and Computer Engineering
May 2009	B.S. Rensselaer Polytechnic Institute Honors: Summa cum laude Major: Applied Physics, Minor: Materials Science and Engineering

Professional Experience

Department of Electrical and Computer Engineering, UC Santa Barbara
Graduate Student Researcher

10/2012 – present

- Develop the growth of Ga- and N-polar AlInGaN materials by (MOCVD)
- Characterize the electrostatic and transport properties of AlInGaN materials
- Connect material properties to the parameters which may be controlled during MOCVD growth
- Developed growth processes for III-N Hot Electron Transistors (HETs)
- Developed growth processes for N-polar InAlN-based HEMTs

MOCVD Lab, UC Santa Barbara
Laboratory Manager

06/2011 – present

- Oversee the operation of a Veeco TurboDisc reactor
- Perform preventative maintenance to enhance reliability
- Troubleshoot and repair malfunctions that affect multiple systems in the MOCVD reactor
- Designed and implemented system upgrades to improve ease of access during maintenance operations, and also improve overall reactor reliability
- Decreased reactor down-time by 40% through improved process control and preventative maintenance cycles, as well as system upgrades as of October 2015

Department of Electrical and Computer Engineering, UC Santa Barbara
Graduate Student Researcher

06/2009 – 10/2012

- Designed and fabricated novel solar cells utilizing the polarization charge in III-N heterojunctions
- Used ion implantation and regrowth technologies to manipulate the internal electric fields of multiple quantum well solar cells
- Developed growth of high-indium-content, long-wavelength InGaN quantum wells by MOCVD
- Developed the growth of Ga-polar polarization-doped p-(In)GaN which yielded carrier high concentration beyond what is possible from thermal ionization of dopant species

TJ Watson Research Center, IBM, Yorktown Heights, NY
Undergraduate Research Intern

05/2008 – 8/2008

- Modified and expanded upon the source code for S/TRIM (Scattering/Tracking and Range of Ions in Matter)
- Added functionality to: simulate ion distributions in non-planar substrates, raster the incident "ion beam", and cant the incident "ion beam" in MATLAB
- My program, SRIM 2D, has had continued use after my internship ended

Publications

M. A. Laurent, D. J. Suntrup III, G. Gupta, U. K. Mishra, *Barrier height inhomogeneity and its impact on (Al, In, Ga)N Schottky diodes*, Journal of Applied Physics (in progress)

M. A. Laurent, G. Gupta, S. Wienecke, A. A. Muqtadir, S. Keller, S. P. DenBaars, U. K. Mishra, *Extraction of net interfacial polarization charge from $Al_{0.54}In_{0.12}Ga_{0.34}N/GaN$ high electron mobility transistors grown by metalorganic chemical vapor deposition*, Journal of Applied Physics, **116**, 183704 (2014)

G. Gupta, **M. A. Laurent**, H. Li, D. J. Suntrup, E. Acuna, S. Keller, U. K. Mishra, *Design space of III-N hot electron transistors using AlGaN and InGaN polarization-dipole barriers*, IEEE Electron Device Letters, **99** (2014).

S. Keller, H. Li, **M. A. Laurent**, Y. Hu, N. Pfaff, J. Lu, D. F. Brown, N. A. Fichtenbaum, J. S. Speck, S. P. DenBaars, U. K. Mishra, *Recent Progress in metal-organic chemical vapor deposition of (000-1) N-polar group-III nitrides*, Semiconductor Science and Technology, **29**, 113001 (2014).

G. Gupta, **M. A. Laurent**, J. Lu, S. Keller, U. K. Mishra, *Design of polarization-dipole-induced isotype heterojunction diodes for use in III-N hot electron transistors*, Applied Physics Express, **7**, 014102 (2014).

J. Kim, **M. A. Laurent**, H. Li, S. Lal, U. K. Mishra, *Barrier reduction via implementation of InGaN interlayer in wafer-bonded current aperture vertical electron transistors consisting of InGaN channel and N-polar GaN drain*, Applied Physics Letters, **106**, 023506 (2015).

X. Liu, R. Yeluri, J. Kim, S. Lal, A. Raman, C. Lund, S. Wienecke, J. Lu, **M. A. Laurent**, S. Keller, U. K. Mishra, *In-situ metalorganic chemical vapor deposition and capacitance-voltage characterizations of Al_2O_3 on Ga-face GaN metal-oxide-semiconductor capacitors*, Applied Physics Letters, **103**, 053509 (2013).

J. Lu, D. Denninghoff, R. Yeluri, S. Lal, G. Gupta, **M. A. Laurent**, S. Keller, S. P. DenBaars, U. K. Mishra, *Very high channel conductivity in ultra-thin channel N-polar GaN/(AlN,InAlN, AlGaN) high electron mobility hetero-junctions grown by metalorganic chemical vapor deposition*, Applied Physics Letters, **102**, 232104 (2013).

Conference Presentations

M. A. Laurent, D. J. Suntrup III, G. Gupta, S. Keller, U. K. Mishra, *Determination of AlInGaN/GaN Schottky diode barrier height by temperature-dependent current-voltage measurements*, 42nd International Symposium on Compound Semiconductors, June 2015, Santa Barbara, CA, USA.

M. A. Laurent, G. Gupta, S. Wienecke, A. A. Muqtadir, S. Keller, S. P. DenBaars, U. K. Mishra, *Extraction of AlInGaN/GaN net interfacial polarization charge from MOCVD-grown heterostructures*, 56th Electronic Materials Conference, June 2014, Santa Barbara, CA, USA.

G. Gupta, **M. A. Laurent**, H. Li, D. J. Suntrup, E. Acuna, S. Keller, U. K. Mishra, *Common emitter operation of III-N HETs using AlGaN and InGaN polarization-dipole induced barriers*, 72nd Device Research Conference, June 2014, Santa Barbara, CA, USA.

G. Gupta, **M. A. Laurent**, H. Li, D. J. Suntrup, S. Keller, U. K. Mishra, *Estimation of hot-electron mean free path in GaN using a III-N hot electron transistor*, 72nd Device Research Conference, June 2014, Santa Barbara, CA, USA.

J. Kim, S. Lal, **M. A. Laurent**, U. K. Mishra, *Vertical electron transistors with $In_{0.53}Ga_{0.47}As$ channel and N-polar $In_{0.1}Ga_{0.9}N$/GaN drain achieved by direct wafer-bonding*, 72nd Device Research Conference, June 2014, Santa Barbara, CA, USA.

D. Denninghoff, J. Lu, **M. A. Laurent**, E. Ahmadi, S. Keller, U. K. Mishra, *N-polar GaN/InAlN MIS-HEMT with 400 GHz f_{max}*, 70th Device Research Conference, June 2012, Santa Barbara, CA, USA

M. A. Laurent, A. Raman, D. Denninghoff, S. Keller, U. K. Mishra, *Low-temperature growth and characterization of p-GaN and graded p-InGaN layers by MOCVD for photovoltaic applications*, 53rd Electronic Materials Conference, June 2011, Santa Barbara, CA, USA.

S. Bangsaruntip, G. M. Cohen, **M. A. Laurent**, et al., *Role of Geometry on ion-implantation into nanowires*, MRS Spring Meeting & Exhibit, April 2011, San Francisco, CA, USA.

Invited Talks

M. A. Laurent, *Growth and electrical characterization methods for AlInGaN materials*, ECE Visiting Scholar Seminar, University of California at Davis, November 2015.

Geetak Gupta, **Matthew Laurent**, Donald J. Suntrup III, Haoran Li, Stacia Keller, Umesh K. Mishra, "Design and Fabrication of III–N Hot Electron Transistors," *Nitrides Seminar*, University of California Santa Barbara, February, 2014.

Geetak Gupta, Jing Lu, Sansaptak Dasgupta, **Matthew Laurent**, Stacia Keller, Umesh K. Mishra, "III–N Hot Electron Transistors," *Teledyne Scientific and Imaging*, Thousand Oaks, CA, USA, April 2013.

Outreach and Teaching Experience

Undergraduate Intern Mentor, UC Santa Barbara

2010 – 2014

- Provided instruction and guidance on key skills for experimental research and project design
- Mentored four different undergraduate students on a variety of projects including material characterization, measurement design, and electrical characterization
- Three of the students have continued to graduate school, the fourth has entered the private sector
- Provided recommendation letters and/or served as a personal reference for them

National Nanotechnology Infrastructure Network "Chip Camp", UC Santa Barbara

2010 – 2013

- Guided classes of high school students through a fabrication process in the UCSB Teaching Cleanroom
- Taught proper safety procedures and lab hygiene for performing controlled experiments
- Instructed students to design experiments to isolate and test microfabrication process variables

Teaching Assistant: Graduate Level Device Physics (ECE 221A), UC Santa Barbara

01/2012 – 04/2012

- Led office hours, wrote homework solutions, co-wrote problems and solutions to final exam
- Provided additional instruction to graduate students during office hours as necessary

National Nanotechnology Infrastructure Network "Nano Days", Santa Barbara, CA

2010 – 2012

- Volunteered for community-wide outreach program designed to provide instruction on nanoscale science and technology in a fun, accessible way to people of all ages and backgrounds

ABSTRACT

MOCVD Growth and Electrical Characterization of AlInGaN Heterojunctions

by

Matthew A. Laurent

III-N-based electronics and optoelectronics are reaching great levels of sophistication in the areas of power electronics, RF amplifiers, lighting, and display technologies. Much of the success of these technologies can be traced to superior or unique material properties that make III-N solid state devices the ideal choices for their applications. Consequently, state of the art devices are being pushed to the limit of what may be fabricated due to strain considerations in the AlGaN and InGaN systems. In order to continue the advancement of III-N based technologies toward greater performance, into new niches, and open up new markets, it is necessary to exploit the entire (Al,In,Ga)N system to its fullest potential.

The utility of AlInGaN is multifaceted. These materials can be used for strain management, fabrication of lattice-matched devices, and polarization engineering to manipulate electric fields within device active regions, or even create high-conductivity charge slabs. Unlike ternary alloys, there is no single unique combination of band gap, polarization charge, and lattice constant, which results in greater device design freedom. However, to effectively utilize these materials, reliable growth processes must be established, and the material parameters critical to device design must be characterized.

This thesis describes the progress in AlInGaN development at UCSB beginning with identification and exploration of the AlInGaN growth parameter space, using understanding from ternary alloys as a springboard into quaternary growth. From there, the thesis progresses to the establishment of a design toolbox for AlInGaN based devices via electrical

characterization of these materials. Challenges associated with the AlInGaN system, coupled with sparse literature on the topic, necessitated the design of experiments to isolate and characterize the material parameters from measurements of solid-state devices. Electrical characterization focused on the net polarization charge at heterojunction interfaces, as well as the effects of Schottky barrier height inhomogeneity on both electrostatics and transport in diodes. The quantum mechanical scattering at the metal-semiconductor junction will be discussed, as will its physical origin and impact on diode current. A major goal of this thesis was to establish a device design toolbox populated with information of experimentally calculated net polarization charge at AlInGaN/GaN interfaces and Schottky barrier heights. This goal was accomplished and the information was established for future device designers in the field.

The thesis concludes with a discussion of the application and exploitation of the unique effects observed in AlInGaN materials to device design. Future outlook will be given on avenues for research in AlInGaN materials and AlInGaN-based devices, and direction will be provided to finish populating the (electrical) device design toolbox with conduction band offset measurements.

CONTENTS

Chapter 1

INTRODUCTION

As of the time of writing, the world has been made aware of the merits of the III-N material system. From the solid-state lighting revolution to RADAR advancements, RF electronics, and, more recently, power electronics, the impact of GaN and GaN-based devices is undeniable. The III-N materials are firmly established as a versatile player in solid-state electronics, and have entered their adolescence. Consequently, while a great deal of fabrication technology and knowledge regarding materials has been developed, there is still much to be discovered. Furthermore, there are no clear roadmaps to increasing performance with III-N solid state device. New paradigms must be established and new routes toward innovation are begging to be discovered.

The III-N fields of optoelectronics, RF electronics, and power electronics were all rooted in materials science advancements, and the utility of heterojunction design. It is in materials development that the next significant technologies in nitride-based devices will be realized. The question is – what's next? What is the next frontier to tackle for materials? In spite of its successes, the III-N material system is still highly constrained by lattice mismatch and growth condition disparity. An important goal for the future of III-N is to engage in device engineering with a larger design space. Doing so will require utilizing materials that can provide a wider range of band gap values and strain states to the substrate than is possible with AlGaN or InGaN. This sets the stage for the rise of AlInGaN-based devices. To provide a little perspective:

In recent years, the fabrication of AlInGaN heterojunctions and electronic devices have become an active area of research in materials growth, characterization, as well as device development[1–3]. Especially in light of the strain- and polarization-related limitations of ternary III-N devices, the development of AlInGaN-based heterojunction devices has become an attractive goal[4,5]. The current trends in III-N optoelectronics are to conquer the ever-elusive "green gap" of reduced performance and to expand their influence into the field of ultraviolet emitters[6–9]. In either direction, the researcher is faced with strain limitations in AlGaN or InGaN. In the field of electronic devices, HEMT designers seek ever-higher conductivity in the channel, and vertical electronics could make use of heterojunctions in a variety of ways (i.e. a CAVET current blocking layer)[10–15]. In these applications, AlGaN has also been the dominant material for heterojunction design. Thus, the engineer is quickly confronted with design limitations due to the inflexibility of ternary alloys. Figure 1.1a visualizes the diversity in material properties that are available within the III-N system, while Figure 1.1b highlights the very small region of the III-N materials spectrum currently used in state-of-the-art devices.

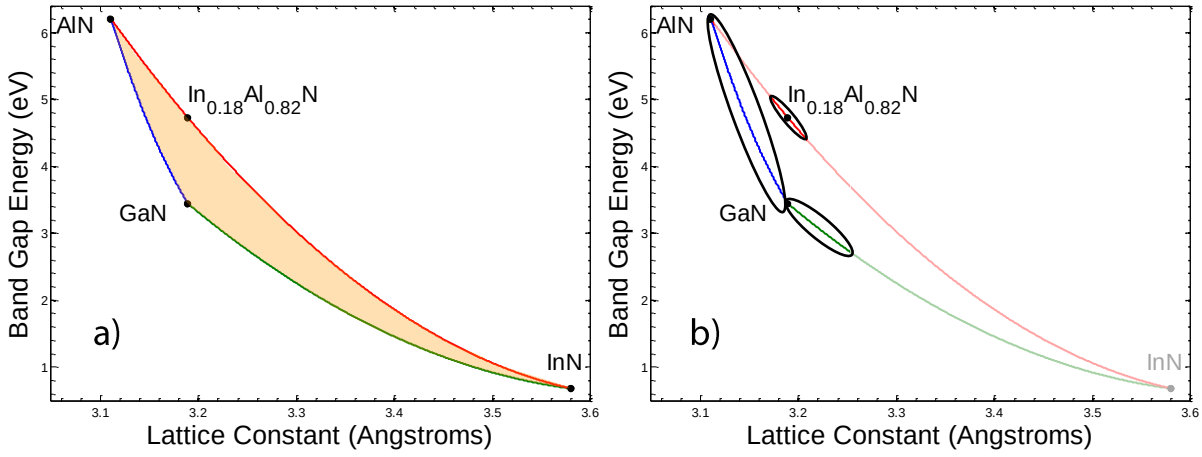

Figure 1.1 shows the entirety of the III-N band gap versus lattice constant plot in part a), which shows a large variety in achievable band gaps and lattice constants. Figure 1.1b) shows the region of this parameter space which is commonly achievable via MOCVD growth.

AlInGaN-based heterojunctions have many advantageous features for device design, and provides a significant increase in design freedom, where the net interfacial polarization charges, lattice constants, and band gap energies may be treated as design parameters with fewer constraints [16–18]. As in other III-V semiconductor systems, quaternary alloys may be used to independently control the strain and band gap in the AlInGaN material. This has several relevant technological applications, such as enabling lattice-matched heterojunction devices to GaN, where the AlInGaN band gap may take on a continuum of values between GaN (3.42 eV) and lattice-matched InAlN (4.7 eV).

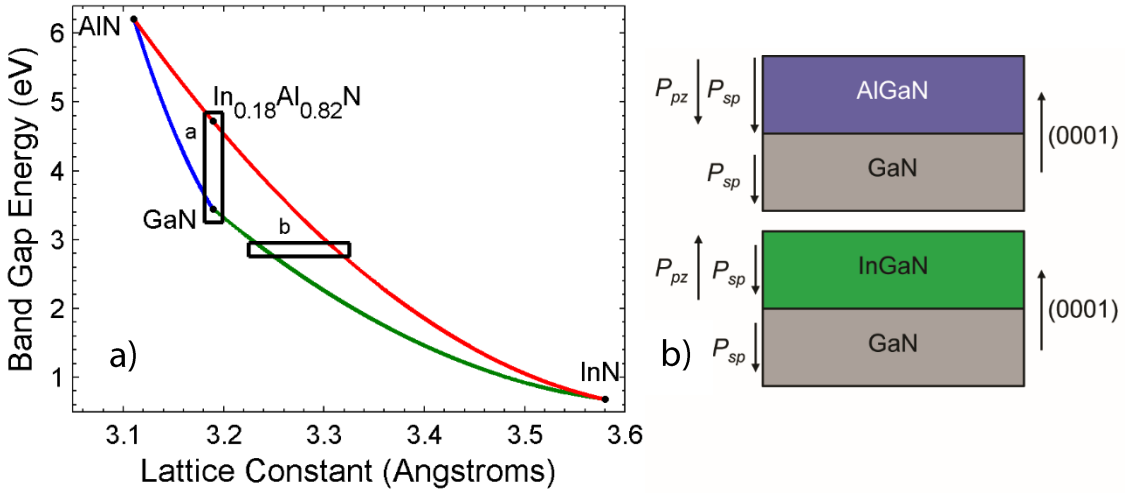

Figure 1.2a) Region a) shows AlInGaN films lattice-matched to GaN, with varying net interfacial polarization charge, $Q_{\pi}(net)$, and band gap (E_g), while region b) shows AlInGaN films with E_g = 2.75 eV, and varying $Q_{\pi}(net)$ and strain state, $\Delta a/a_0$ (a_0 is the lattice constant of the GaN substrate). Figure 1.2b) shows how the opposing sense of piezoelectric polarization charge between AlGaN and InGaN can be used to control the total polarization of an AlInGaN film.

Lattice-matched films are useful for vertical electronic devices due to the ability to block leakage current using thick layers without the risk of strain relaxation. The growth of intentionally strained AlInGaN alloys may also be used to mitigate the cumulative strain in

multilayer heterojunction devices. Precisely controlling strain and composition can also allow for the tailoring of $Q_{\pi}(net)$ at interfaces (as visualized in Figure 1.2a and Figure 1.2b).

AlInGaN provides the researcher with the maximum amount of control over the electrical properties of heterojunctions, which allows for engineering of the electric field in device structures. AlInGaN can also provide increased control over graded layers (i.e. polarization doped layers), or to tailor the barrier heights present in device structures. This can be a gateway to the realization of novel device designs, and more[16]. Furthermore, there is evidence that electron mobility in AlInGaN/AlN/GaN HEMTs may exceed that of $Al_{0.83}In_{0.17}N$/AlN/HEMTs[19,20], which can be directly applicable to a wide variety of devices, from the highly practical to the truly novel.

Furthermore, why AlInGaN and not AlGaNP or AlGaNAs? This is a twofold answer. The first is a pragmatic concern: there is a large disparity between growth conditions required for III-N materials and growth conditions for other III-V semconductors, and it is more difficult to control the group-V lattice site composition than the group-III composition[21]. The second is due to fundamental materials limitations. Nitrogen has poor solubility in As- or P-based materials,[22] and it is difficult to incorporate into the crystal[23]. Furthermore, GaAs and GaP form in the zinc blende crystal structure, whereas III-N semiconductors form in the wurtzite crystal structure. AlInGaN allows for the optimization of a growth window within the overall III-N parameter space, with direct control over growth rates via group-III injection, and without any ill effects from attempting to combine incongruous materials (wurtizte GaN with zinc blende III-Vs).

1.1 CURRENT STATE-OF-THE-ART

There are several groups around the world conducting research on AlInGaN materials and devices. Aachen University (the group of Andrei Vescan) has produced the largest amount of material regarding the MOCVD growth of AlInGaN[1,2]. There has also been some work by molecular beam epitaxy (MBE) from Notre Dame with Debdeep Jena and Huili Xing's groups[20], and pulsed atomic layer epitaxy (PALE) and MOCVD from Asif Khan's group at University of South Carolina[24]. If the growth data from Chapter 2 of this thesis is compared with the data from the various publications from Aachen, the reader will find that the growth conditions are nearly identical in spite of a significant difference in reactor geometries.

When it comes to device development, the current state-of-the-art is what can be described as a semi-empirical regime of experiment and engineering. This means that the properties of devices are unknown and unpredictable with these materials so far. Any new devices require significant characterization prior to fabrication. This is not necessarily a bad thing, but it limits the complexity of projects that researchers are willing to take on. More complex device design, integration, or attempts to create novel solid-state devices generally require a greater degree of "maturity" in the material system. Maturity in a material system boils down to having access to robust and repeatable fabrication procedures, as well as experience with and prior knowledge of material properties.

Regardless of being in the earlier stages of design and development with AlInGaN materials, groups from around the world have achieved devices that show great promise for the AlInGaN system. Notre Dame has demonstrated RF AlInGaN-based HEMTs with a mobility of 1850 cm2/V-s and an f_{max} of 300 GHz[20]. Some limited polarization engineering has been demonstrated at Aachen University, where both epitaxially determined enhancement-

mode HEMTs and p-type HEMTs have been fabricated[25,26]. Furthermore, University of Seoul, Tokushima University, Rensselaer Polytechnic Institute, and the University of South Carolina have demonstrated the utility of AlInGaN in the optoelectronics fields. At Seoul, they have utilized the malleable polarization in the AlInGaN system to show improvements in green LED performance[27], which was likely inspired by earlier work at RPI[28]. At Tokushima and the University of South Carolina, they have gone toward the UV end of the spectrum to show the promise of AlInGaN in that area[8,29].

In order to move beyond the semi-empirical phase of research and enter an era of predictive device design, it is of paramount importance to characterize heterojunction electrostatics, transport-related material properties, as well as broach the very large field of interfacial and surface studies. This thesis attempts to hit all of these key areas, such that the results of this thesis may be broadly applied to the future of device design in III-N materials.

1.2 OUTLINE OF THESIS

This thesis is split up into three sections and two themes. The ultimate goal of this dissertation was to establish a design toolbox for AlInGaN-based devices, which encompasses the knowledge of a wide variety of material constants relevant to band diagram engineering and electrostatic design. The first section in Chapter 2 covers MOCVD growth development and materials characterization of AlInGaN. As of the beginning of this work, there were no established growth techniques for AlInGaN at UCSB. After the growth space was established and reliable growth recipes were constructed, the theme of the thesis shifts to electrical characterization of heterojunctions.

Chapter 3 discusses the measurements and calculations for determining the net interfacial polarization charge, Q_{π}*(net)* at an AlInGaN/GaN interface. These numbers are compared with the body of theoretical work in the area, and incorporated into a simulation software suite. Chapter 4 discusses the measurement of the Schottky Barrier Height of AlInGaN to nickel, another important material parameter, as well as the characterization of vertical transport across the metal-semiconductor junction of the AlInGaN-nickel diode. Finally, Chapter 5 concludes this dissertation with future outlook for continued AlInGaN materials development by MOCVD, and proposes a measurement technique for calculating conduction band offsets, ΔE_c, of AlInGaN to GaN. Between Q_{π}*(net)*, Schottky Barrier height, and ΔE_c, the design toolbox for electrostatic design (or DC device design) can be considered to be complete.

This would then allow researchers in the nitrides to leave behind the phase of empirical experimentation in the AlInGaN system for a more productive standard of predictive device design. Even without experimental knowledge of ΔE_c, having experimental knowledge regarding the polarization and Schottky diode characteristics is a significant step forward for engineering with AlInGaN materials. Chapter 5 concludes with future outlook for device applications and experimentation designed to take advantage of some of the unique properties of AlInGaN materials.

1.3 REFERENCES

[1] B. Reuters, M. Finken, A. Wille, B. Holländer, M. Heuken, H. Kalisch, and A. Vescan, **093524**, 1 (2013).

[2] B. Reuters, A. Wille, B. Holländer, E. Sakalauskas, N. Ketteniss, C. Mauder, R. Goldhahn, M. Heuken, H. Kalisch, and A. Vescan, J. Electron. Mater. **41**, 905 (2012).

[3] Y.A. Chang, Y.R. Lin, J.Y. Chang, T.H. Wang, and Y.K. Kuo, IEEE J. Quantum Electron. **49**, 553 (2013).

[4] M.A. Khan, J.W. Yang, G. Simin, R. Gaska, M.S. Shur, and A.D. Bykhovski, Appl. Phys. Lett. **75**, 2806 (1999).

[5] Nidhi, S. Dasgupta, J. Lu, J.S. Speck, and U.K. Mishra, IEEE Electron Device Lett. **33**, 794 (2012).

[6] M.H. Crawford, IEEE J. Sel. Top. Quantum Electron. **15**, 1028 (2009).

[7] T. Frost, A. Banerjee, K. Sun, S. Chuang, and P. Bhattacharya, IEEE J. Quantum Electron. **49**, 923 (2013).

[8] Y. Muramoto, M. Kimura, and S. Nouda, Semicond. Sci. Technol. **29**, 084004 (2014).

[9] I.L. Koslow, M.T. Hardy, P. Shan Hsu, P.-Y. Dang, F. Wu, A. Romanov, Y.-R. Wu, E.C. Young, S. Nakamura, J.S. Speck, and S.P. DenBaars, Appl. Phys. Lett. **101**, 121106 (2012).

[10] J. Lu, X. Zheng, M. Guidry, D. Denninghoff, E. Ahmadi, S. Lal, S. Keller, S.P. DenBaars, and U.K. Mishra, Appl. Phys. Lett. **104**, 092107 (2014).

[11] J. Simon, V. Protasenko, C. Lian, H. Xing, and D. Jena, Science **327**, 60 (2010).

[12] R. Yeluri, J. Lu, D. Browne, C.A. Hurni, S. Chowdhury, S. Keller, J.S. Speck, and U.K. Mishra, in *72nd Device Res. Conf.* (IEEE, 2014), pp. 253–254.

[13] S. Dasgupta, T.E. Mates, J.S. Speck, and U.K. Mishra, Growth (Lakeland) 80 (n.d.).

[14] U.K. Mishra and T.E. Kazior, Proc. IEEE **96**, 287 (2008).

[15] U.K. Mishra, P. Parikh, and Y. Wu, Power **90**, (2002).

[16] D. Jena, J. Simon, A. Wang, Y. Cao, K. Goodman, J. Verma, S. Ganguly, G. Li, K. Karda, V. Protasenko, C. Lian, T. Kosel, P. Fay, and H. Xing, Phys. Status Solidi Appl. Mater. Sci. **208**, 1511 (2011).

[17] H. Hahn, B. Reuters, A. Wille, N. Ketteniss, F. Benkhelifa, O. Ambacher, H. Kalisch, and A. Vescan, Semicond. Sci. Technol. **27**, 055004 (2012).

[18] M.A. Khan, J.W. Yang, G. Simin, R. Gaska, M.S. Shur, H.-C. zur Loye, G. Tamulaitis, A. Zukauskas, D.J. Smith, D. Chandrasekhar, and R. Bicknell-Tassius, Appl. Phys. Lett. **76**, 1161 (2000).

[19] L. Rahimzadeh Khoshroo, N. Ketteniss, C. Mauder, H. Behmenburg, J.F. Woitok, I. Booker, J. Gruis, M. Heuken, A. Vescan, H. Kalisch, and R.H. Jansen, Phys. Status Solidi Curr. Top. Solid State Phys. **7**, 2001 (2010).

[20] R. Wang, G. Li, G. Karbasian, J. Guo, B. Song, Y. Yue, Z. Hu, O. Laboutin, Y. Cao, W. Johnson, G. Snider, P. Fay, D. Jena, and H.G. Xing, IEEE Electron Device Lett. **34**, 378 (2013).

[21] G.B. Stringfellow, *Organometallic Vapor Phase Epitaxy: Theory and Practice*, Second (Academic Press, New York, 1999).

[22] S.B. Zhang and S.H. Wei, Phys. Rev. Lett. **86**, 1789 (2001).

[23] F. Alexandre, *Dilute Nitride Semiconductors* (Elsevier, Amsterdam, The Netherlands, 2005).

[24] J.P. Zhang, E. Kuokstis, Q. Fareed, H.M. Wang, J.W. Yang, G. Simin, M. Asif Khan, G. Tamulaitis, G. Kurilcik, S. Jursenas, a. Zukauskas, R. Gaska, and M. Shur, Phys. Status Solidi Appl. Res. **188**, 95 (2001).

[25] B. Reuters, A. Wille, N. Ketteniss, H. Hahn, B. Holländer, M. Heuken, H. Kalisch, and A. Vescan, J. Electron. Mater. **42**, 826 (2013).

[26] B. Reuters, H. Hahn, A. Pooth, B. Hollander, U. Breuer, M. Heuken, H. Kalisch, and A. Vescan, J.Phys. D Appl. Phys. **47**, 175103 (2014).

[27] S.-H. Park and D. Ahn, IEEE J. Sel. Top. Quantum Electron. **19**, 1901308 (2013).

[28] M.F. Schubert, J. Xu, J.K. Kim, E.F. Schubert, M.H. Kim, S. Yoon, S.M. Lee, C. Sone, T. Sakong, and Y. Park, Appl. Phys. Lett. **93**, (2008).

[29] J.P. Zhang, V. Adivarahan, H.M. Wang, Q. Fareed, E. Kuokstis, A. Chitnis, M. Shatalov, J.W. Yang, G. Simin, M.A. Khan, M. Shur, and R. Gaska, Jpn. J. Appl. Phys. **40**, L921 (2001).

Chapter 2

GROWTH AND MATERIAL CHARACTERIZATION OF Ga-POLAR $Al_xIn_yGa_{(1-x-y)}N$ BY METALORGANIC CHEMICAL VAPOR DEPOSITION (MOCVD)

2.1 GROWTH SPACE IDENTIFICATION WITH TERNARY ALLOYS

The growth studies described here were devoted to developing a practical understanding of the capabilities and limitations of AlInGaN growth by MOCVD. The ultimate goal was to identify the requirements for growing these materials with sufficient quality for implementation in electronic devices. When developing growth processes for new epitaxial films, it is first necessary to look at phenomena that occur during the growth of similar but well-documented materials. For the MOCVD growth of quaternary III-N alloys, analyzing the properties of epitaxial films of the ternary alloys that comprise AlInGaN – AlGaN, InGaN, and InAlN – under identical growth conditions provided a useful, yet incomplete, picture of the growth mode of AlInGaN. Identifying compositional limitations and the causes of detrimental growth phenomena in the ternaries helped to provide initial constraints upon the MOCVD growth of AlInGaN, thereby facilitating experiment design for subsequent mapping of the growth space.

Observations related to MOCVD growth of III-N materials, which informed the development of an AlInGaN growth process, included: temperature dependence of X_{InN} in InGaN alloys[1], pit formation at threading dislocations of low-temperature nitride films[2–4], relationship between X_{AlN} in AlGaN films and input gas flow rates[5–7], high impurity levels of

C and O in low-pressure and -temperature nitride films[8–10], and the growth optimization of lattice-matched InAlN by MOCVD[11,12].

2.1.1 General growth constraints

All samples in these studies were grown on GaN-on-sapphire pseudo-substrates wherein the GaN pseudo-substrate was grown by the standard two-step growth technique: a thin (~20 nm), low-temperature GaN nucleation layer followed by a high-temperature GaN buffer of about 1.5 μm in thickness. For samples with low enough strain (i.e. no visible signs of cracking or extreme surface roughening), the threading dislocation density was determined by the estimated to be $3 \cdot 10^{18}$ cm^{-3}. This accounted for almost the entirety of the samples included in this thesis.

Samples used for structural characterization were performed primarily as regrowths. This means that the pseudo-substrate was grown separately from the layer of interest, whether it be AlGaN, InAlN, or AlInGaN. The advantage of doing so is increased throughput: one 2" GaN wafer can be cut into four pieces and regrown upon. The regrowth recipes are significantly shorter than beginning every growth with nucleation. See Appendix A for recipe numbers; most growths from March through May 2016 were regrowth recipes. It is important to note that the composition and morphology of the epilayers under study were not sensitive to whether the films were regrowths or continuous growths. Furthermore, for electrical robustness, all device samples in the antecedent chapters were performed as continuous growths.

TMGa (trimethyl gallium) was used as the gallium precursor for the GaN pseudo-substrates. AlGaN, InAlN, and AlInGaN utilized TMAl (trimethyl aluminum), TEGa (triethyl gallium), and TMIn (trimethyl indium) for aluminum, gallium, and indium precursors,

respectively. Nitrogen was supplied by ammonia (NH_3). Ferrocene (Cp_2Fe) supplied iron for creating semi-insulating pseudo-substrates, which was utilized for experiments involving high electron mobility transistors (HEMTs). Disilane (Si_2H_6) was used for n-type doping for growth of Schottky diodes.

Due to the high aluminum and indium fractions that must coexist in AlInGaN films, as well as the interest in lattice-matched films of varying band gap, the general growth conditions of $In_{0.18}Al_{0.82}N$ were adopted for AlInGaN growth. The InAlN growth conditions provided a starting point for growth temperature, chamber pressure, NH_3 flow rate, and growth rate. Previous work by Roy Chung indicated that lattice-matched InAlN is best grown at a growth chamber temperature of 804 C, a growth chamber pressure of 70 torr, 4 slm of NH_3 flow, and a growth rate of approximately 1.1 nm/minute[11]. Total gas flow in the chamber was 11.5 slm using nitrogen as a carrier gas. The indium composition was controlled by the temperature, the growth pressure of 70 torr minimized C and O impurity concentrations, and the slow growth rate made a smooth surface morphology possible.

2.1.2 Using ternary alloys to identify boundaries of the AlInGaN growth space

Before proceeding with the growth of quaternary films, it was necessary to understand the dependence of film composition and growth rate upon the relative molar flow rates of TMAl, TEGa, and TMIn for ternary alloys. Subsequent experiments were performed on AlGaN and InGaN films, all grown under conditions identical to InAlN. In the case of constant pre-reactions, the AlGaN growth rate should be[13]

$$r_g(AlGaN) = r_g(GaN) + r_g(AlN), \tag{2.1}$$

and the binary growth rates for GaN and AlN should be linear functions of the molar flow rate of their respective precursors[13]:

$$r_g(GaN) = m_1 \cdot f_{\mathrm{TEGa}} + b_1, \tag{2.2a}$$

$$r_g(AlN) = m_2 \cdot f_{\mathrm{TMAl}} + b_2. \tag{2.2b}$$

The intercepts of these lines, b_1 and b_2, should be (nearly) zero. Furthermore, the AlN fraction of the film may be calculated from[13]

$$X_{\mathrm{AlN}} = \frac{r_g(AlN)}{r_g(AlGaN)}, \tag{2.3}$$

and compared to the experimental value of X_{AlN} as measured via X-Ray Diffraction (XRD). Experiments showed that the expected linear relationship between binary growth rate and precursor molar flow held true, and that there was a 1:1 correlation of measured to calculated X_{AlN} (Figure 2.1). The easiest way to calculate growth rate is by measuring thickness by XRD and dividing by growth time. It should be noted that this is an approximation for films with low strain. Precautions were taken to avoid relaxation in these series and, when X_{AlN} became large, bulk layers were substituted for AlGaN/GaN superlattices [cite].

The solid crystal fraction of aluminum may also be calculated from the molar fraction of the aluminum precursor in the vapor phase:

$$X_{\mathrm{AlN}} = \frac{f_{\mathrm{TMAl}}}{f_{\mathrm{TMAl}} + {}^{1}/_{k}(f_{\mathrm{TEGa}})}, \tag{2.4}$$

where k is defined as the distribution coefficient for aluminum in AlGaN under these growth conditions[13]. The distribution coefficient may be understood as the ratio between diffusion coefficients between aluminum and gallium in the vapor phase, and may be calculated from

$$k = \frac{D_{\mathrm{Al}}}{D_{\mathrm{Ga}}} = \frac{X_{\mathrm{AlN}}/X_{\mathrm{GaN}}}{f_{\mathrm{TMAl}}/f_{\mathrm{TEGa}}}, \tag{2.5}$$

in which D_{Al} and D_{Ga} are the aluminum and gallium diffusion coefficients, respectively[13]. Under these growth conditions, it was found that the distribution coefficient is 3.13 (Figure 2.1d), which indicated that the diffusion coefficient for aluminum is much larger than that of

gallium for low-pressure and low- temperature MOCVD growth. The extracted value for *k* was then used to plot the right hand side of equation (2.4) against X_{AlN} as determined from XRD. The slope was equal to unity, and the intercept to zero, as should be the case with a properly calculated distribution coefficient.

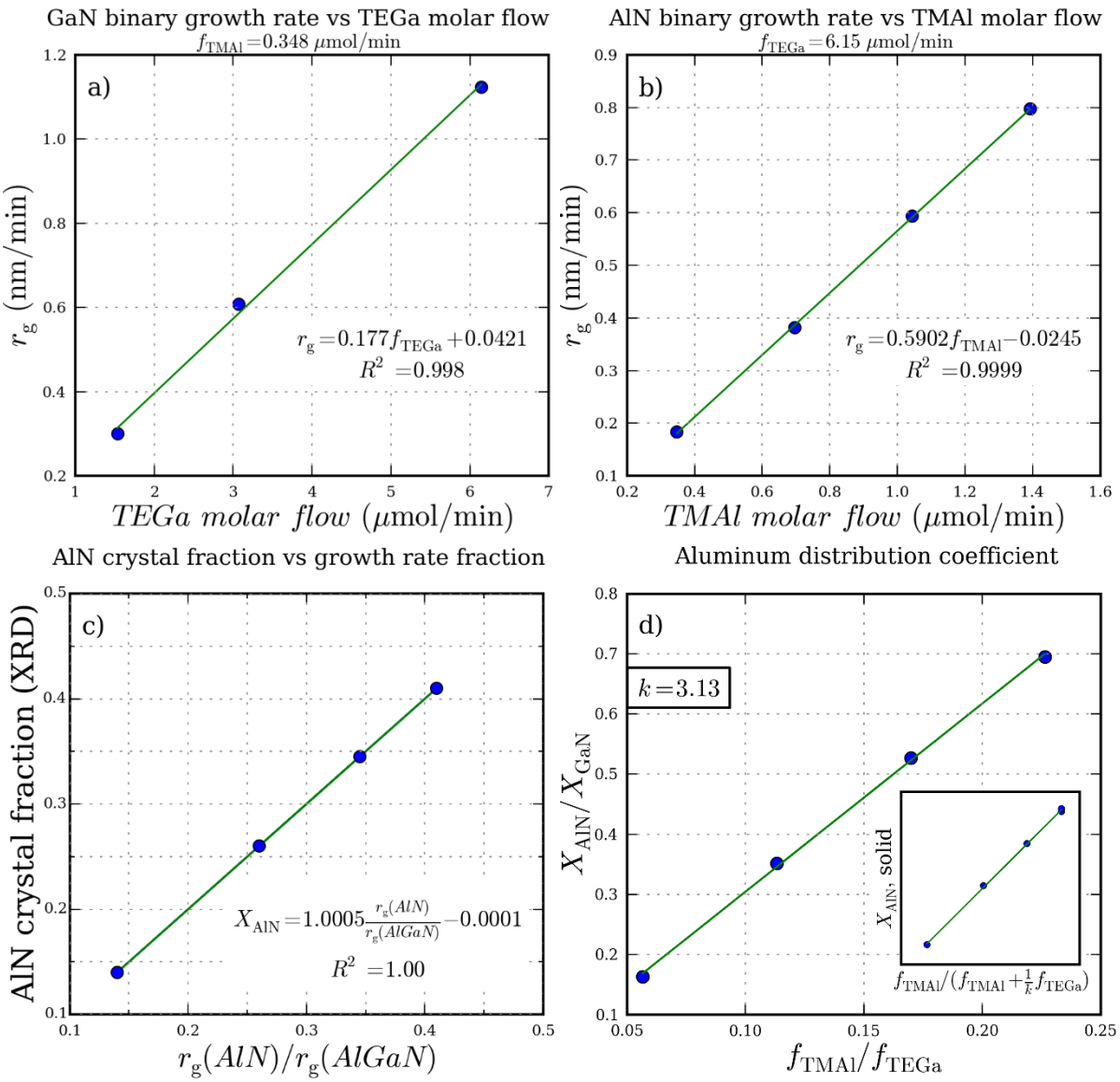

Figure 2.1. Flow rate dependencies of r_g(GaN) (1a) and r_g(AlN) (1b) for AlGaN grown under InAlN conditions. These trends indicate constant pre-reactions during AlGaN growth. Figure 2.1c shows the 1:1 correlation of calculated to measured AlN composition. Figure 2.1d shows a plot of equation (2.5) and

calculated value of *k;* inset plot is solid vs. vapor phase X_{AlN} from equation (2.4). The inset trend line has a slope of one and intercept of zero.

This data indicated that the rate of pre-reactions during growth was constant, and provided the necessary information to grow AlGaN at any composition and growth rate as dictated by the desired device structure. It should be noted that the growth rates for all samples in this study were between 1-2 nm/minute; a general constraint during growth space mapping was to attempt to match AlGaN, InGaN and AlInGaN growth rates to that of lattice-matched $In_{0.18}Al_{0.82}N$.

The InGaN recipe was created by adopting the growth conditions for lattice-matched InAlN, and was grown with a temperature of 804 °C and TMIn molar flow rate of 15.28 µmol/min. TEGa replaced TMAl in the recipe with a flow rate of 6.15 umol/min to ensure that the InGaN growth rate was approximately equal to those of the InAlN and AlGaN (see Figure 2.1a). From XRD measurements, the InN fraction of the crystal was found to be only 0.05. The lower X_{InN} for InGaN was expected, since the greater In-Al bond strength in InAlN as compared with the In-Ga bond strength would prevent indium desorption during growth[12]. It was therefore expected that larger X_{AlN} would correlate with larger X_{InN} due to decreased indium vapor pressure over aluminum-containing solids. InAlN represented the case where indium stability was the highest and incorporation into the crystal was the greatest (InGaN being the lowest-stability case), if all other conditions were held constant. Using InGaN and $In_{0.18}Al_{0.82}N$ as lower and upper bounds on indium incorporation, respectively, a line was interpolated between the two crystal compositions to give a rough idea of the X_{InN} to expect when performing initial growths of AlInGaN (Figure 2.2).

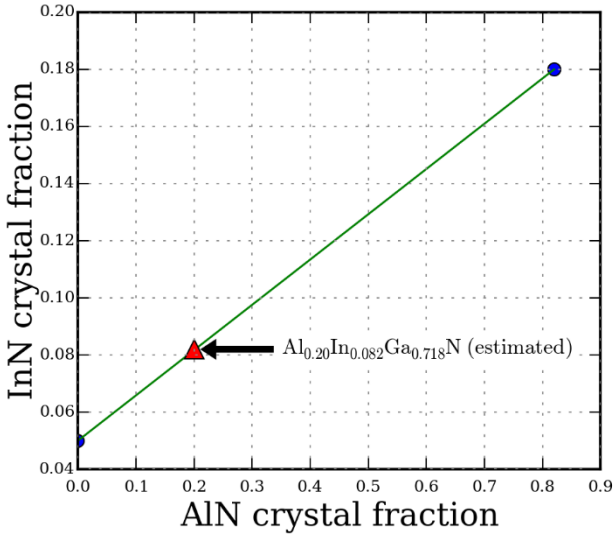

Figure 2.2. The dependence of X_{InN} on X_{AlN} at 804 °C and 70 torr was assumed to be linear for initial AlInGaN growths. The red marker at $X_{AlN} = 0.20$ corresponds to $X_{InN} = 0.082$.

With the compositional dependences of AlGaN and InGaN established under these growth conditions, the first AlInGaN growth was attempted with a projected composition of $X_{AlN} = 0.20$ and $X_{InN} = 0.082$. The first AlInGaN growths were performed as a thickness series to observe the surface morphology and relaxation mechanisms of this class of materials. The purpose of the thick films during initial growths was predicated by the fact that Rutherford Backscattering Spectrometry (RBS) was necessary to unambiguously determine the crystal composition of this new material. RBS analysis, according to engineers at Evans Analytical Group, is most reliable for films over 100 nm in thickness.

2.1.3 Initial AlInGaN Growth: composition and relaxation

RBS analysis was performed on a 152 nm thick AlInGaN film, and the following crystal fractions were calculated: $X_{AlN} = 0.26$ +/- 0.01, $X_{InN} = 0.072$ +/- 0.003, and $X_{GaN} = 0.668$ +/- 0.005. The uncertainty in the RBS measurement was smaller than the magnitude of variation in composition that is expected from MOCVD growth. Furthermore, the RBS data

showed that the crystal composition was constant as a function of depth (see Figure 2.3), and did not demonstrate any composition pulling effects[14,15]. Due to the great degree of precision in this measurement, this initial sample was stored in reserve as a calibration standard. A piece of the standard was then used to calibrate the Secondary Ion Mass Spectroscopy (SIMS) tool at UCSB. SIMS is typically used to find the concentration of minority species in a crystal matrix, such as C or O in GaN. Furthermore, the relative sensitivity of the detector varies between different ionic species. Consequently, it was necessary to calibrate the composition calculation for scans in which majority species of the crystal matrix (Al, Ga, In) were being detected. Doing so enabled the use of SIMS in place of RBS for composition measurement of subsequent AlInGaN samples.

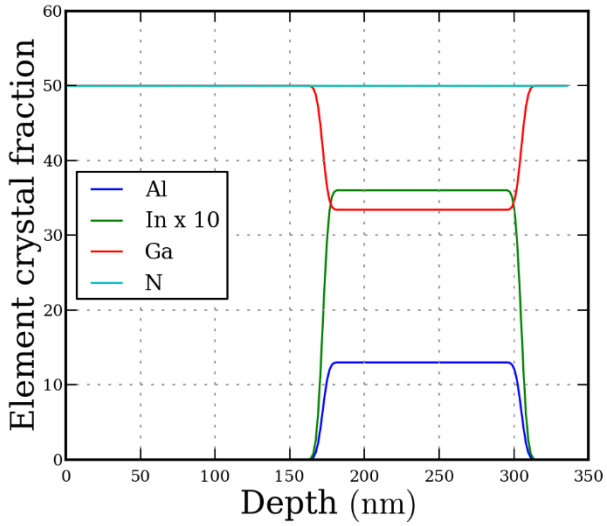

Figure 2.3. RBS data was used to find the composition of the first AlInGaN growth and confirmed depth uniformity of composition.

In addition to RBS analysis, this sample was used as part of a thickness series to understand the morphological breakdown of these low-temperature films. The AFM images in Figure 2.4 depict the change in surface morphology as film thickness was increased from 75 nm to 300 nm. Significant large-scale changes, ranging in size from hundreds of nanometers

to 1 μm or more, were visible alongside small-scale changes, with a characteristic length on the order of tens of nanometers. The large-scale features that presented themselves with increasing film thickness were hillocks, which appeared to be faceted, as well as pits that had hexagonal cross-sections.

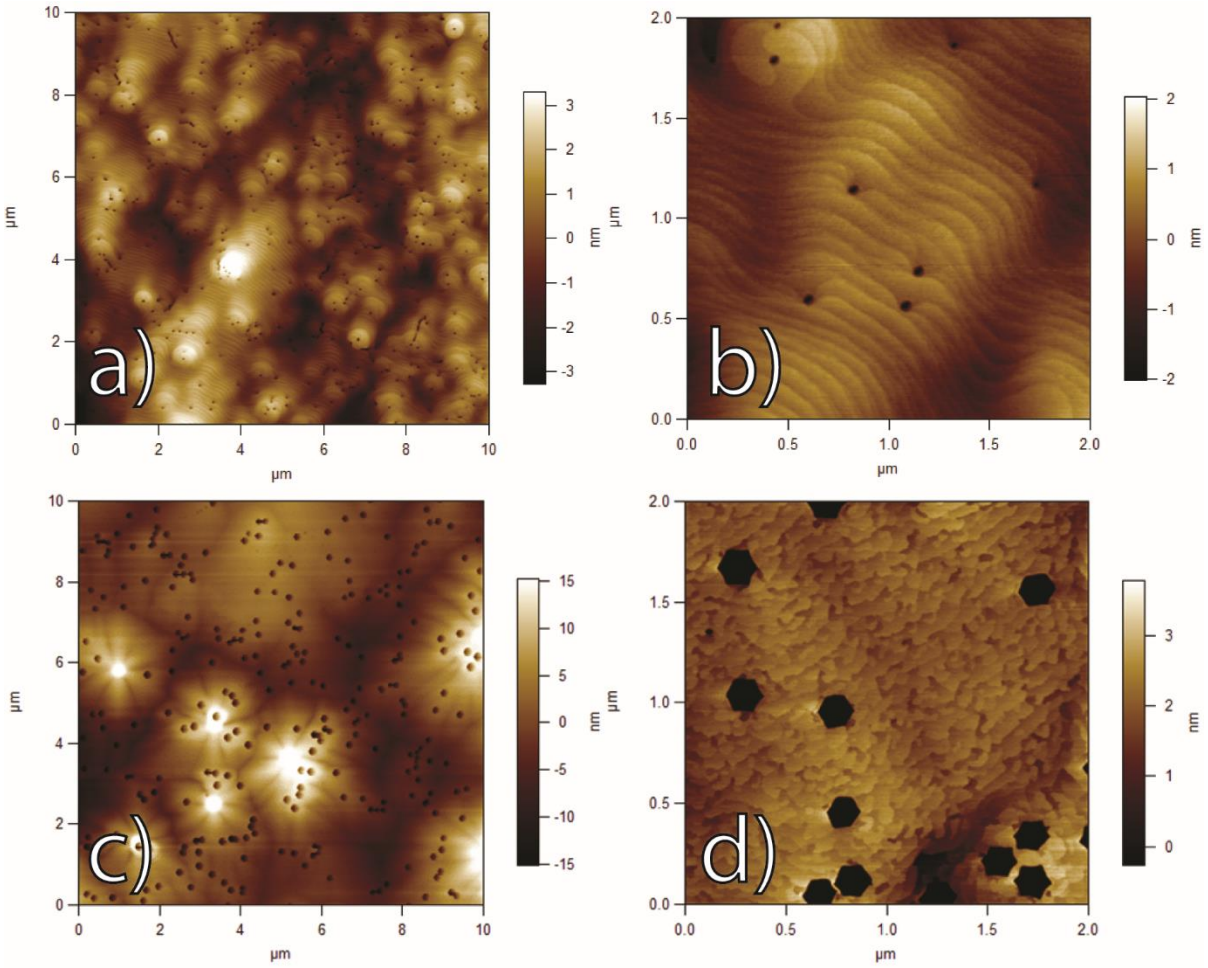

Figure 2.4. Morphological evolution of $Al_{0.26}In_{0.072}Ga_{0.668}N$ with thickness. Figure 2.4a and 2.4b show 10um and 2um scans from a sample with 75 nm AlInGaN grown on a GaN template, respectively. 2.4c and 2.4d show 10um and 2um scans from a sample with 300 nm AlInGaN grown atop a GaN template, respectively.

By comparing the orientation of the pit facets in the AFM scan with the orientation of the sample during measurement, it was found that the pits terminated on the m-planes at the surface. This is identical to the V-defects that are commonly observed in InGaN films[3,16]. The

small-scale feature that became apparent with increasing thickness was the breakdown of smooth step-flow growth. The thin AlInGaN sample showed smooth step-flow growth (Figure 2.4b), whereas the 300-nm-thick sample showed an irregular step flow pattern (Figure 2.4d). This mottled step flow contained a much higher density of kinks and corners than the thin sample, which may affect growth rate, impurity incorporation, and indium incorporation into the crystal. XRD ω-2θ scans were compared between the three samples. The spacing between Pendellösung fringes indicated that the sample thickness increased proportionally to the growth time, and that growth rate was constant[17].

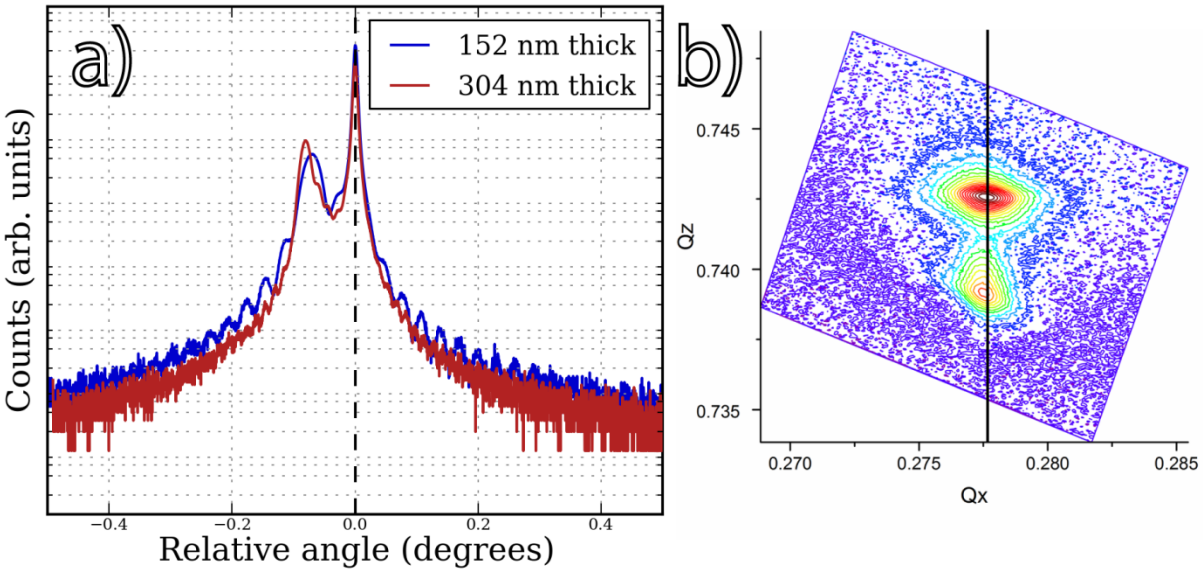

Figure 2.5. a) The red XRD ω-2θ spectrum (300 nm thick) has a main satellite peak that is shifted in the direction of greater compressive strain (larger lattice constant) from the blue spectrum (150 nm thick). b) The $(10\bar{1}5)$ RSM showed partial film relaxation, due to the offset of the AlInGaN peak from GaN peak (black line).

When comparing the 300 nm and 150 nm AlInGaN samples, the position of the layer peak shifted away from the GaN substrate, which indicated greater compressive strain (or larger lattice constant) in the 300 nm film (Figure 2.5a). That would then indicate a slightly higher X_{InN}, or partial relaxation of the film. A reciprocal space map (RSM), which was aligned

to the $(10\bar{1}5)$ reflection of GaN, of the thick sample showed ~4% film relaxation, which may account for the peak displacement (Figure 2.5b).

The hillocks present on thicker samples were investigated in more detail. High resolution AFM scans showed that the hillocks were not faceted as was first presumed by the large-area scan. From Figure 2.6, it was clearly visible that the step flow spiraled around the center of the hillock. It was therefore concluded that these hillocks were the result of spiral growth around a screw-type threading dislocation. During step-flow growth, the leading step edge intersected with the dislocation, which runs perpendicular to the growth direction[18]. The screw-type dislocation served to pin the step edge in position, and all subsequent step-flow growth in the vicinity of the dislocation grew around the pinned step.

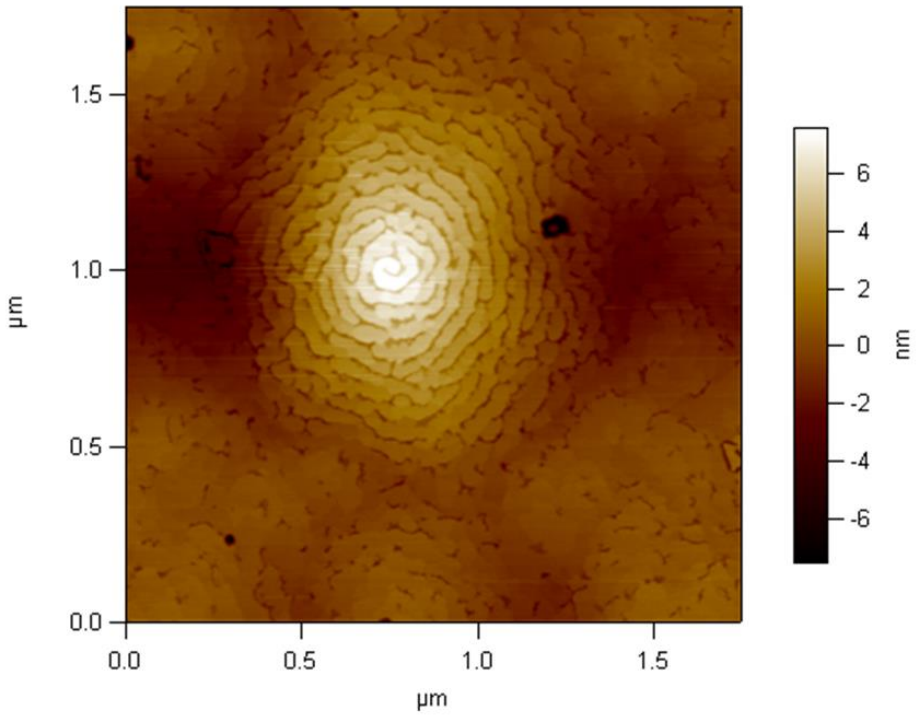

Figure 2.6. Spiral growth hillocks are typical features on thick AlInGaN samples (>150 nm thickness). The mottled step flow, large pit, and tall hillock indicate that this sample is starting to undergo strain relaxation. The step flow around the center of the hillock indicates that the hillock core is a screw-type dislocation, causing spiral growth to circle around the step edge that intersected with, and was pinned by, the screw dislocation.

2.2 $Al_xIn_yGa_{(1-x-y)}N$ GROWTH SPACE MAPPING

Once the strain relaxation mechanisms for AlInGaN were understood, other major growth conditions were varied to see the effects on the resultant films. First, the ratio of TMAl to TEGa injected during growth was investigated, followed by substrate temperature during growth, for the purpose of assessing compositional effects and nature of pre-reactions during growth. Then the impact of *V-III* ratio on crystal composition, as well as growth rate and sample roughness, was examined. Finally, the impact of varying growth conditions and crystal compositions on surface morphology was evaluated. These observations were combined with SIMS impurity analysis to give the optimal window for device-grade material growth.

2.2.1 TMAl and TEGa flow rate series

It is impossible to discuss the effect of TMAl flow rate variation without TEGa because of the combined effect of the two reactant gases during growth. Just as for AlGaN films, it is important that $r_g(AlN)$ varies linearly with TMAl molar flow, and $r_g(GaN)$ with TEGa. From the experiments with AlGaN, pre-reactions rates were expected to be constant. However, with the addition of TMIn into the gas phase, it was important to verify that this was still the case. The added degree of complexity in AlInGaN films makes the flow rate relationship even more critical: with indium present in the crystal, it is necessary to ensure that there are independent means for controlling X_{AlN}, X_{GaN}, and X_{InN}. The ideal scenario is where X_{AlN} and X_{GaN} are controlled by the flow rates of their respective precursor gases, and X_{InN} is controlled by temperature (with no temperature effects on X_{AlN} or X_{GaN}). This has proven to be the case for other research groups[19], and it should hold true for material grown at UCSB as well. It should be noted that for all experiments, TMIn flow was held constant at 15.28 μmol/min, and the

sample surface temperature was about 804 C. This flow rate was well into the saturation regime for indium incorporation for InAlN[11], and should also hold true for AlInGaN.

Just as for the AlGaN growth calibrations, Figures 2.1a and 2.1b were recreated for the AlInGaN system, and can be seen in Figure 2.7. It was interesting to note that the slope in 7a is almost identical to 1a, and that of 7b is nearly identical to 1b. This would indicate that the rate of change of the binary growth rate for AlN and GaN with precursor flow was unchanged from AlGaN, even though there was a third element incorporating onto the group-III sublattice and a much higher total group III precursor flow.

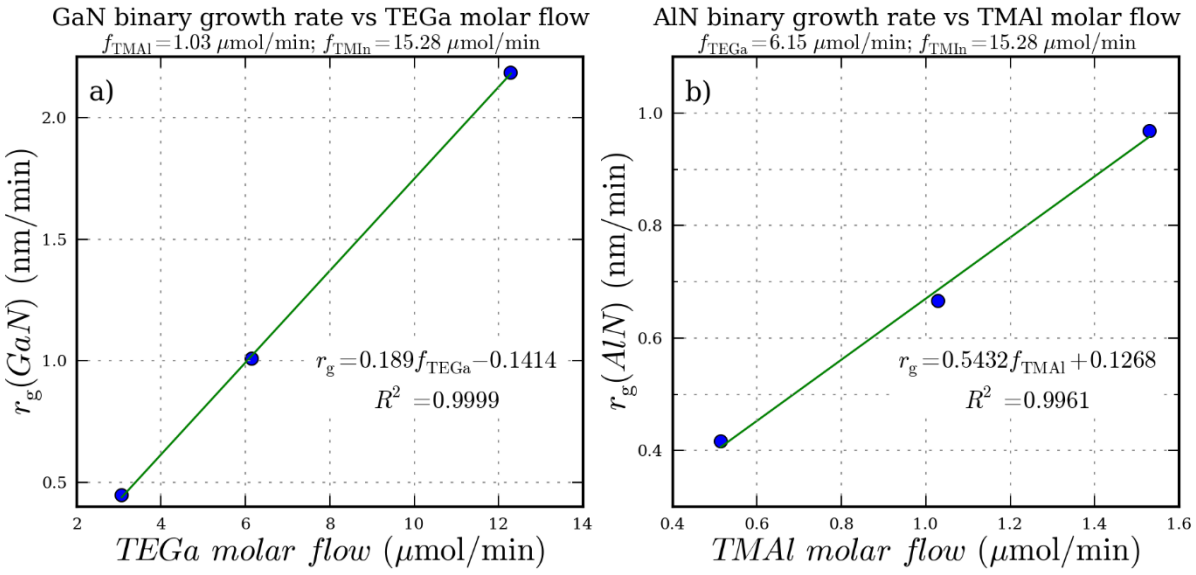

Figure 2.7. Flow rate dependence of AlN (2.7a) and GaN (2.7b) binary growth rates in AlInGaN.

After establishing the independence of GaN and AlN binary growth rates in AlInGaN films, the next issue to be addressed was establishing compositional dependences on precursor flow rates. Due to the greater complexity than the AlGaN case, and for general utility of the MOCVD process, it was necessary to carefully map this out for predictive purposes. Demonstrating the ability to grow AlInGaN alloys is interesting, but the ability to accurately pinpoint specific compositions during growth is where the actual technological utility of AlInGaN can be realized. If one imagines the potential applications of AlInGaN, lattice-

matched devices will require that epilayers be grown with very accurate compositions. This will also hold true for polarization or electric field engineering. To establish the dependence of crystal composition on TMAl and TEGa, the crystal fraction of aluminum and indium were plotted against TMAl flow (with TEGa flow held constant), and TEGa flow (with TMAl flow held constant). Figure 2.8a shows the composition dependence on TMAl molar flow with TEGa held at 6.15 µmol/min, while Figure 2.8b shows the composition dependence on TEGa molar flow with TMAl held at 1.03 µmol/min.

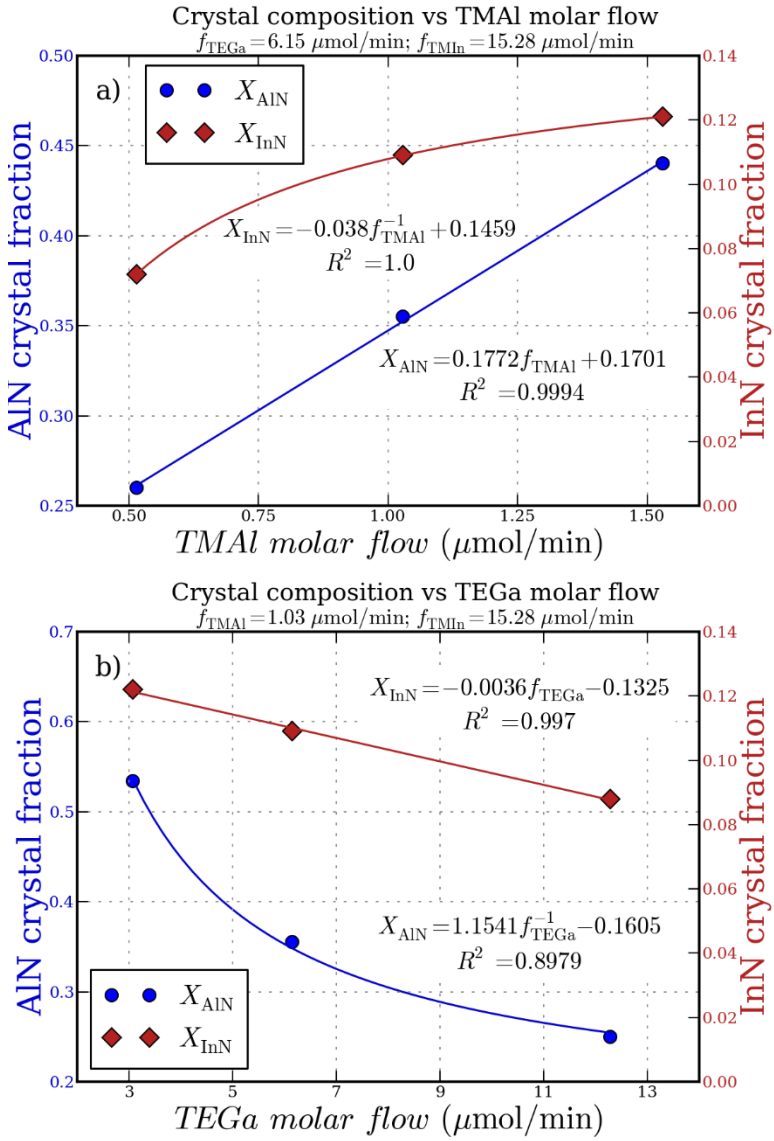

Figure 2.8. Crystal composition flow dependences for AlInGaN alloys.

Figure 2.8a showed a linear dependence of X_{AlN} on TMAl molar flow, which is very useful for predicting flow rates for future growths. An interesting feature of Figure 2.8a was the nonlinear increase in X_{InN} that appeared to begin to saturate at higher TMAl flows (and therefore X_{AlN}). This result supported the earlier statements about higher X_{AlN} suppressing indium desorption during growth. Since the indium fraction saturated at an X_{InN} value less than what is observed for InAlN, which has the same TMIn molar flow as all of these AlInGaN growths, while the X_{AlN} shows no signs of saturating, it suggested that indium and gallium compete for positioning on the group-III sublattice at high TMAl flow (and high X_{InN}). Since the TEGa flow during InAlN growth is zero, and there is a finite GaN growth rate in these AlInGaN samples, one can conclude that the maximum X_{InN} that the crystal composition will saturate at as a function of TMAl flow would depend upon $r_g(GaN)$. Therefore, if $r_g(GaN)$ were to increase, X_{InN} would be expected to decrease.

These conclusions are borne out in Figure 2.8b, which does indeed show decreasing X_{InN} with increasing TEGa flow. The relationship appeared to be linear, but may asymptotically approach a value at very high TEGa flow rates if $r_g(GaN) >>> r_g(InN)$, or if extremely high TEGa flow would begin to introduce deleterious gas-phase pre-reactions. Any finite flow of TMIn should incorporate indium into the crystal, even at very high $r_g(GaN)$ values. Figure 2.8b also showed an inverse relationship between X_{AlN} and TEGa flow rate for a constant TMAl flow. However, if the TMAl and TEGa flow rates are modulated together, and X_{AlN} is observed as a function of flow rate ratio,

$$FRR = \frac{f_{TMAl}}{(f_{TMAl}+f_{TEGa})}, \tag{2.6}$$

there may be a different functional dependence.

Figure 2.9 shows that a plot of this nature gives a linear relationship between X_{AlN} and *FRR*, and it also confirmed the increase and subsequent saturation of X_{InN} with increasing X_{AlN} (i.e. *FRR*). It was also interesting to note that X_{AlN} vs. *FRR* was linear for both AlGaN and AlInGaN. Therefore, for a constant TMIn flow rate, aluminum incorporation into the crystal is independent of the indium incorporation. This is extremely useful for future AlInGaN growth development, as it makes it possible to predict X_{AlN} directly from Figure 2.9 and the desired *FRR*. Furthermore, this provided additional evidence toward the idea that gallium and indium atoms compete for incorporation onto the group-III sublattice in AlInGaN, as suggested by the data from Figure 2.8. It is important to note that equation (2.6) was not equated to X_{AlN} since it was not straightforward to determine any sort of an aluminum distribution coefficient, as in equation (2.4). Equation (2.6) also did not take the effect of f_{TMIn} into account. The purpose of defining the *FRR* was to develop an empirical relationship between crystal composition and experimental variables.

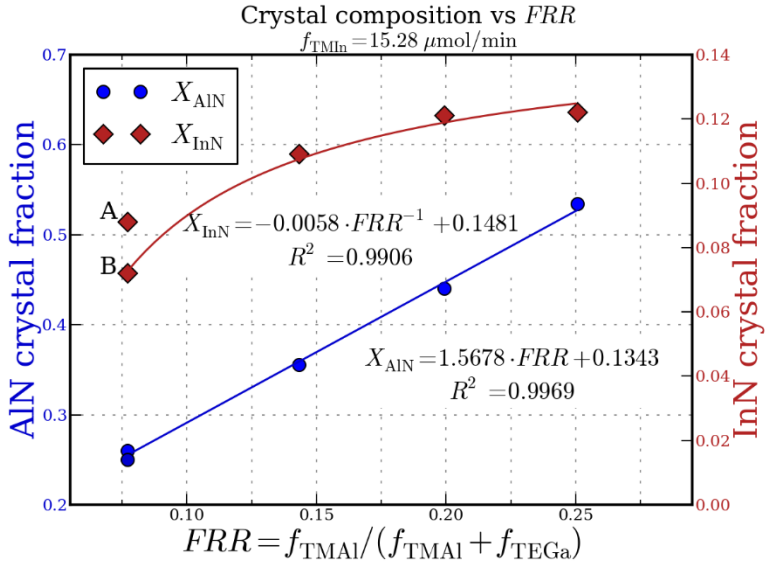

Figure 2.9. Variation in X_{AlN} and X_{InN} with flow rate ratio as defined in equation (2.6). The sample labeled *A* had larger X_{InN} than sample *B*, in spite of nearly identical X_{AlN}, due to $r_g(A)$ being twice that of $r_g(B)$.

There is a major caveat that must be acknowledged when trying to understand the relationship between gas flow and crystal composition: these trends are only strictly true when all reactant flows, except for the one under investigation, are held constant. This can be demonstrated by comparing the data points labeled "A" and "B" in Figure 2.9. f_{TMAl} and f_{TEGa} in sample A were twice as large as in sample B. Per the predictions in Figure 2.8 and the linear relationship between gas flow and binary growth rate in Figure 2.7, it would be expected that X_{AlN} for the two samples be identical, which was found to be true. However, the data from Figure 2.8b also suggested that X_{InN} should be identical, which it clearly was not. In fact, comparing samples A vs. B would indicate an opposing relationship from Figure 2.8b: namely that X_{InN} increases with increasing f_{TEGa}. However, since indium incorporation very susceptible to desorption due to the element's high vapor pressure during growth, one must keep in mind that sample A had a higher growth rate and as compared to sample B. Higher growth rate would decrease the residence time of indium adatoms on the surface before they are buried by the next monolayer, effectively decreasing the time that they have to desorb. Consequently, if the *FRR* is held constant and both f_{TMAl} and f_{TEGa} are increased simultaneously, X_{InN} will increase in spite of X_{AlN} remaining constant.

2.2.2 Temperature series

Following the flow rate series, a temperature series was grown to see the effect of sample temperature during growth on crystal composition. Sample temperature was measured by laser pyrometry, thus the temperatures reported in Figure 2.10 were the temperatures of the sample surfaces during AlInGaN deposition. Temperature was controlled by heating filament current; a current set-point of 58.87 corresponded to a sample surface temperature of 785 °C, and a set-point of 61.87 corresponded to a temperature of 816 °C. These two temperatures

were the extremes of the temperature series. It was expected that changing the growth temperature would be the most effective way of controlling X_{InN}.

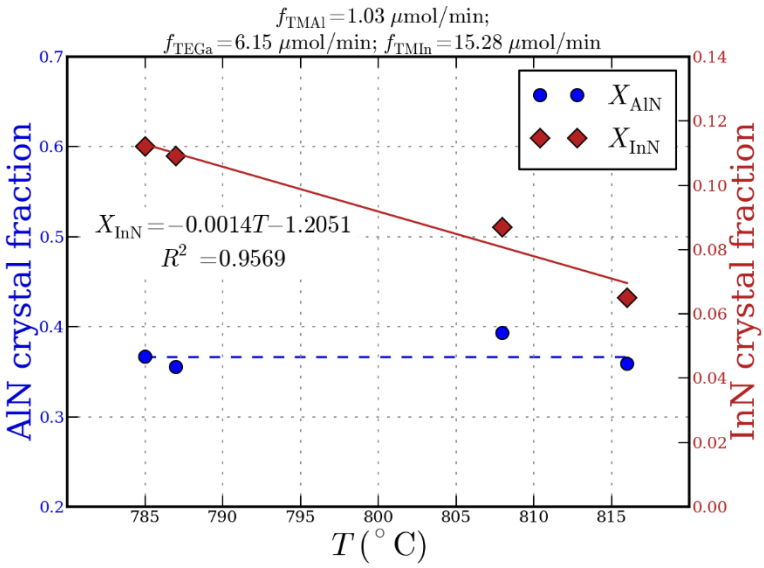

Figure 2.10. X_{AlN} and X_{InN} for AlInGaN samples as a function of sample surface temperature during growth. X_{InN} had a linear relationship with temperature, while X_{AlN} did not vary with temperature. The blue dashed line between X_{AlN} data points serves as a guide for the eye.

Figure 2.10 shows that the indium content in the crystal decreased linearly with increasing temperature in the operational temperature window within which most AlInGaN experiments were performed. This provided evidence that the temperature independence of X_{AlN} from AlGaN films extended to AlInGaN, and the temperature dependence of X_{InN} is similar to that of InGaN. Furthermore, the fact that X_{AlN} did not change with decreasing X_{InN} (and increasing temperature) adds more evidence to the notion that indium and gallium atoms are in competition for incorporation on the group-III sublattice of the growing AlInGaN film. This is also useful for band- and strain-engineering purposes. Independently controlling X_{InN} with temperature, and having knowledge of $\Delta X_{InN}/\Delta T$, provides a means for controlling strain, band gap, and crystal composition to a fine degree. The previous section demonstrated that

using *FRR* or f_{TMAl} was the most reliable way to predict X_{AlN}. However, varying the growth rate but keeping *FRR* constant can yield different X_{InN} values. Therefore, the most reliable method of composition calibration would be to determine X_{AlN} via *FRR*, and then adjust the growth temperature as necessary to account for any possible variation in X_{InN} from what is expected.

2.2.3 V-III ratio series

The group V source is usually present in great excess of the group III source during MOCVD growth. Consequently, the same sort of relationships between growth rates and flow rates are not applicable to group V precursor flows[13]. The best method for judging the effects of changing the quantity of group V gas injection during growth is via the V-III ratio. The V-III ratio can be quite a complex variable. Varying this quantity can cause changes in the crystal composition, growth rate[13], and surface mobility of adatoms[5,20]. Changing the V-III ratio can also have indirect effects on surface roughness and morphology.

In order to investigate the effect of V-III ratio on the properties of the resultant materials, the ammonia (NH_3) flow rate was varied while the group III injection was held constant. The TEGa injection was 3.07 µmol/min, TMAl injection was 1.03 µmol/min, and TMIn injection was 15.28 µmol/min. The total flow of gas in the chamber was held constant throughout these experiments. Therefore, the N_2 carrier gas injection was changed by a corresponding amount to account for changes in NH_3 flow from 1 standard liter per minute (slm) to 5 slm. Since the partial pressure of the reactant gases is dependent upon the total gas volume in the chamber at any time, changing the total flow through the reactor can cause changes in the degree of supersaturation in the gas phase, which can lead to differences in growth rates and amount of pre-reactions. In order to eliminate the consequences of these effects, total flow in the reactor

was held constant at 11.5 slm (as with all AlInGaN growths), and the balance of the volume in the chamber was comprised of N_2 carrier gas.

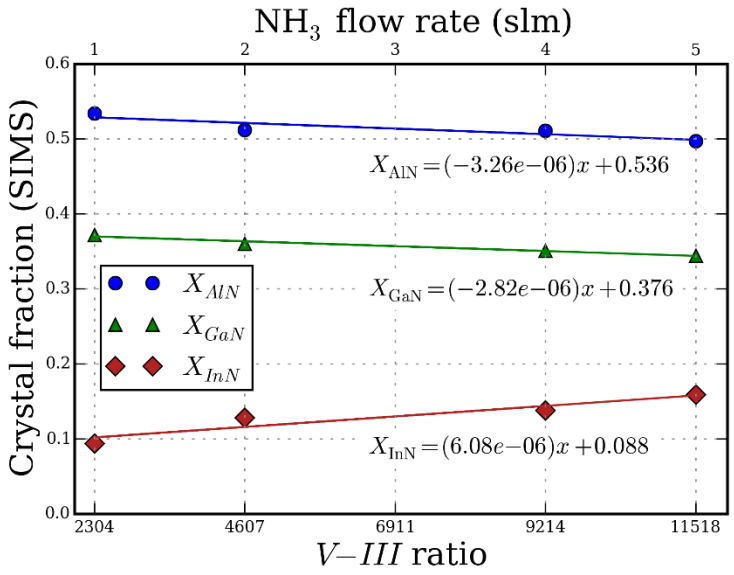

Figure 2.11. Crystal composition versus V-III ratio. X_{AlN} (shape) and X_{GaN} (other shape) decrease at approximately half the rate that X_{InN} (third shape) increases. Crystal fraction and V-III are dimensionless.

To see the effects of V-III ratio on crystal composition, see Figure 2.11 which shows the changes in X_{AlN}, X_{InN}, and X_{GaN} with increasing *V-III*. It is clear from the figure that X_{AlN} and X_{GaN} decreased slightly while X_{InN} increased with increasing *V-III*. The rate of change of crystal fraction as a function of *V-III* was very similar between X_{AlN} and X_{GaN} at $3.26 \cdot 10^{-6}$ and $2.82 \cdot 10^{-6}$, respectively. The total negative rate of change of X_{AlN} and X_{GaN} combined was accompanied by an equal but opposite rate of change of X_{InN} with *V-III*. Therefore, for any incremental decrease in X_{AlN} and X_{GaN}, there was a corresponding increase of X_{InN}. Though the change was gradual over a very large range of NH_3 flow rate values, the effect on the strain state of the crystal was profound, as demonstrated in Figure 2.12.

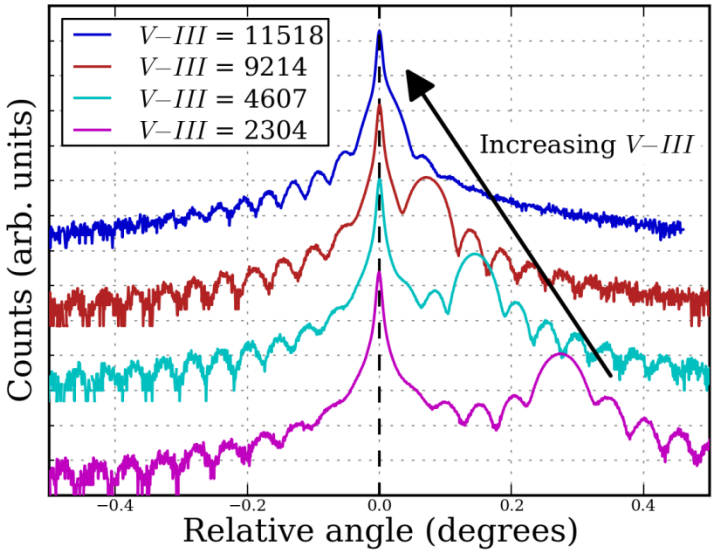

Figure 2.12 shows the change in the AlInGaN satellite peak position with respect to the GaN substrate peak in a V-III ratio growth series of AlInGaN epilayers. Since the change in X_{InN} was much more dramatic than X_{AlN} in this series, the increase in compressive strain in the crystal is mainly due to X_{InN} increasing from 0.094 to 0.159.

Plotting the composition ratios, X_{AlN}/X_{InN}, X_{AlN}/X_{GaN}, and X_{GaN}/X_{InN}, against V-III ratio in Figure 2.13 reveals further details about the response of the crystal composition to a change in *V-III*. First, the X_{AlN}/X_{InN} and X_{GaN}/X_{InN} ratios decrease with increasing *V/III*, and they mirror the changes in one another. These are expected from the data in Figure 2.10. Second, X_{AlN}/X_{GaN} is nearly constant with increasing *V-III*. If X_{AlN}/X_{GaN} is constant and X_{InN} increases with increasing *V-III*, then X_{AlN} and X_{GaN} must decrease together. And, as seen in Figure 2.10, their rate-of-change is nearly identical. Furthermore, since $X_{AlN} + X_{InN} + X_{GaN} = 1$, then any increase in X_{InN} wth *V-III* must be accompanied by a decrease in X_{AlN} and X_{GaN}. This can be described as indium adatoms replacing aluminum and gallium atoms on the group-III sublattice with increasing V-III ratio. Since the slope of X_{AlN} and X_{GaN} with V-III ratio were nearly identical, it is also possible to conclude that there was no preferential replacement of aluminum or gallium with indium. The increase in X_{InN} detracted from X_{AlN} and X_{GaN} equally. This is

different from the temperature and flow rate effects seen in the crystal, where it has been clear that the exchange primarily occurs between indium and gallium.

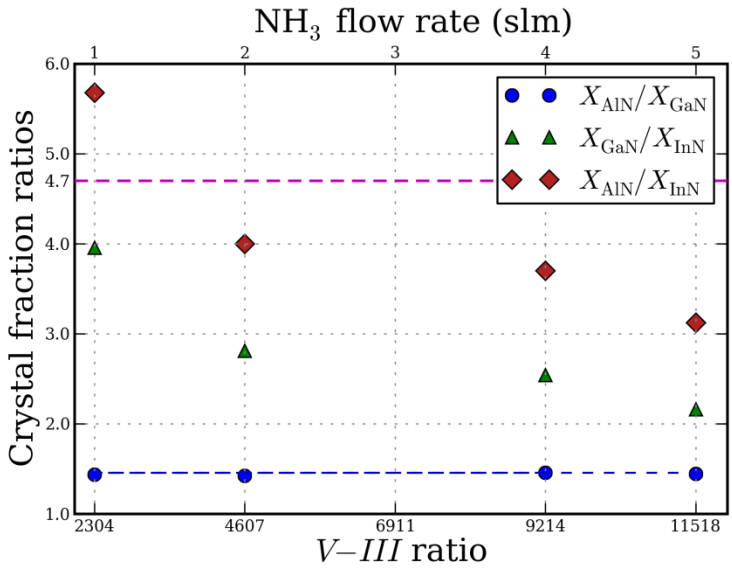

Figure 2.13 shows the change in crystal fraction ratios as a function of *V-III*. The variation in X_{AlN} and X_{GaN} with X_{InN} mirror one another, and X_{AlN}/X_{GaN} (blue circles) is constant with increasing *V-III*. X_{AlN}/X_{InN} (red diamonds) can be used to estimate the strain state of AlInGaN. The dashed magenta line at X_{AlN}/X_{InN} = 4.7 is the ratio for lattice-matching to GaN and accompanies the data to evaluate the strain state of the samples.

Finally, the crystal fraction X_{AlN}/X_{InN} can be used as a strain estimator for AlInGaN. Lattice-matched $In_{0.175}Al_{0.825}N$ has $X_{AlN}/X_{InN} \approx 4.7$, and was indicated in Figure 2.13 as a horizontal, dashed red line[21,22]. Thus, any AlInGaN films that are grown lattice-matched to GaN should have the same ratio of aluminum content to indium content.

Changing the V-III ratio also had a significant effect on growth rate. Figure 2.14 shows the impact of the total AlInGaN growth rate, $r_{g,\,TOT}$ on V-III, as well as the change in the binary growth rates for AlN, GaN, and InN. Over the V-III ratio range investigated in this study, $r_{g,\,TOT}$ increased by about 92% - from 0.84 nm/min to 1.61 nm/min. The AlInGaN growth rate can be broken up into its constituent binary alloy growth rates, as was done for AlGaN (equation (2.1)). Just as for the case of AlGaN,

$$r_{g,TOT} = r_g(AlN) + r_g(GaN) + r_g(InN), \text{ where} \tag{2.7}$$

$$r_g(AlN) = X_{AlN} \cdot r_{g,TOT}, \tag{2.8a}$$

$$r_g(GaN) = X_{GaN} \cdot r_{g,TOT}, \text{ and} \tag{2.8b}$$

$$r_g(InN) = X_{InN} \cdot r_{g,TOT}. \tag{2.8c}$$

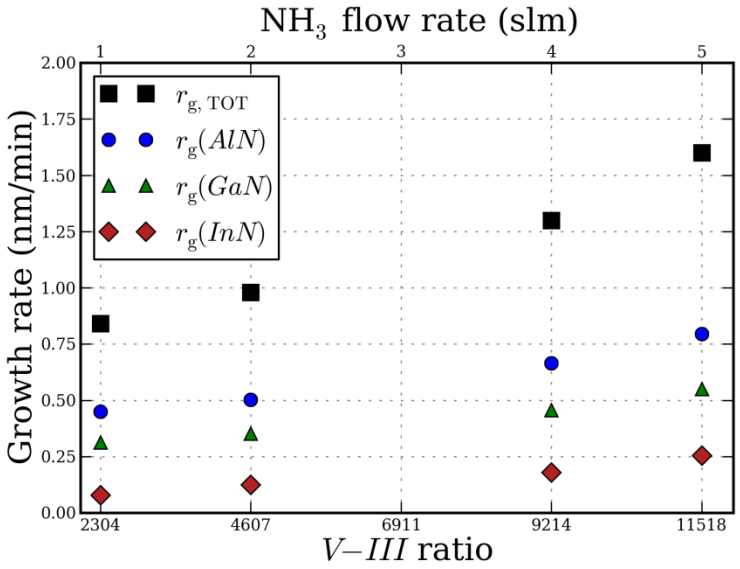

Figure 2.14 shows the total AlInGaN growth rate (black squares), as well as the binary growth rates for AlN (blue circles), GaN (green triangles), and InN (red diamonds). Increasing the V-III ratio from 2304 to 11518 increased the total growth rate by about 100%, and resulted in a $r_g(InN)$ increase of 221.8%

From Figure 2.14, it was discovered that $r_g(GaN)$ increased by 76% to 0.55 nm/min and $r_g(AlN)$ increased by 77% to 0.80 nm/min. The fact that $r_g(GaN)$ and $r_g(AlN)$ increased by a smaller amount than $r_{g,\,TOT}$ explained why X_{GaN} and X_{AlN} decreased slightly as V-III ratio was increased. However, the real point of interest lies with $r_g(InN)$, which increased by 222% (from 0.079 to 0.254 nm/min). The increase in $r_g(InN)$ corresponded to an increase in X_{InN} of 69% (from 0.094 to 0.159). Additionally, the fact that $r_{g,\,TOT}$ increased with increasing *V-III* is another sign that the rate of pre-reactions was constant and did not impact these studies. If pre-reactions played a significant role in AlInGaN growth under these conditions, then $r_{g,\,TOT}$ would decrease with increasing *V-III*.

In the V-III ratio series, there are two simultaneous effects occurring that can impact X_{InN}: increased growth rate and increased group V reactant partial pressure in the gas phase. It is possible to decouple these two effects by examining Figure 2.9 in the flow rate series section of this chapter. Comparing data points A and B it can be seen that X_{AlN} remained constant while X_{InN} increased. This was the result of increasing the growth rate by 100% via an increase in f_{TMAl} and f_{TEGa}. These two flow rates were increased by the same proportion to keep *FRR* a constant, but X_{InN} increased by 22% as a response to the more rapid growth rate. The higher X_{InN} associated with point A also resulted in a larger r_g*(InN)*. The increase in r_g*(InN)* from sample B to sample A was 150%. However, both the increase in X_{InN} and r_g*(InN)* achieved by increasing the growth rate alone were smaller than the increases achieved by increasing *V-III* ratio (X_{InN} increase of 69% and r_g*(InN)* increase of 222%). Therefore, the increase in group V reactant partial pressure over the surface of the growing crystal must account for the remainder of the growth rate and crystal fraction increase.

The final quantity that was investigated during the V-III ratio series was the RMS roughness of the epilayers, as seen in Figure 2.15.

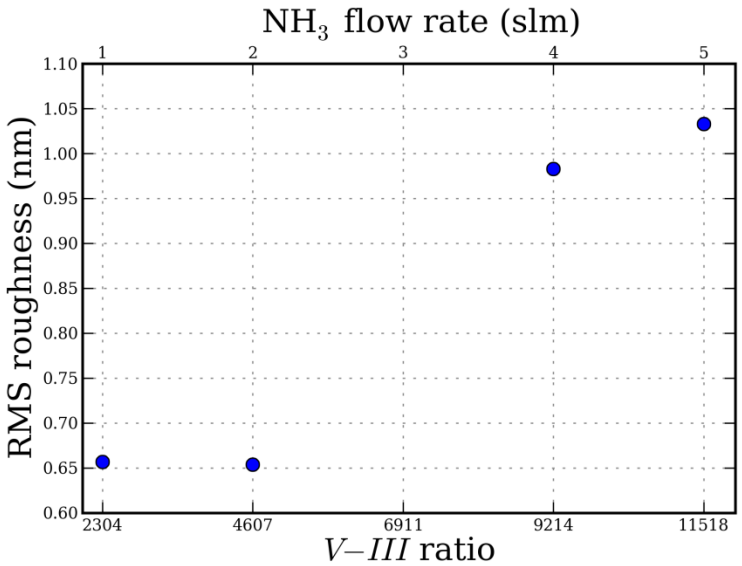

Figure 2.15. RMS roughness as a function of V-III ratio saturates at ~0.65 nm for *V-III* = 4607 and lower.

In order to maintain a fair comparison between samples, RMS roughness was calculated from 2x2 μm AFM scans that were taken at the mid-point between the center and edge of the 2" sapphire substrate. RMS roughness was evaluated from small area scans (as opposed to 10x10 or 20x20 μm scans) to prevent thickness undulations of the underlying substrate and height differences caused by spiral hillock growth from influencing the roughness value calculated for each sample. In order to normalize for the roughening that occurs with increasing sample thickness (see section 2.1.3), all samples were 90-120 nm thick (target thickness was 100 nm). Fortunately, the RMS roughness throughout this entire V-III ratio range is tolerable for device development. As mentioned in section 2.1.3, rougher samples may lead to enhanced indium incorporation at step edges, kinks, and non-planar facets. However, the surface roughness is not severe enough to yield any significant indium uptake by this mechanism.

2.3 $Al_xIn_yGa_{(1-x-y)}N$ SURFACE MORPHOLOGY

2.3.1 Dislocation-mediated surface morphology

The general growth space was established by understanding the response of growth rate, crystal composition, and surface roughness to the major user-controllable variables in MOCVD. However, the growth space can be further refined by understanding the interplay of surface morphology with the growth conditions that were investigated in the previous section. The typical surface morphology of an AlInGaN film was similar to Figure 2.16, which shows a 10x10 and 2x2 μm scan of an $Al_{0.54}In_{0.10}Ga_{0.36}N$ epilayer grown to be 105 nm thick.

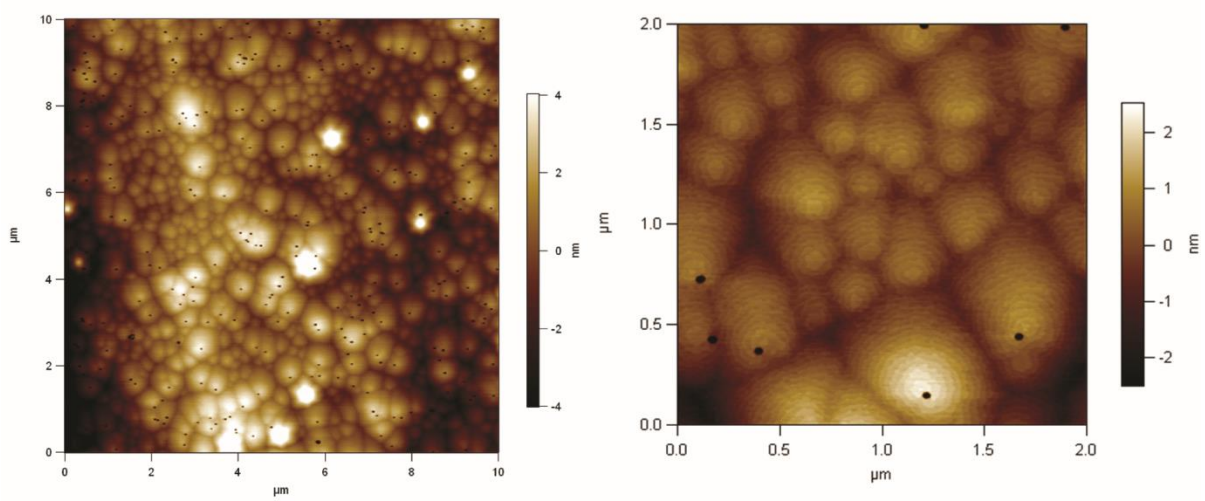

Figure 2.16. Typical surface morphology of AlInGaN films shows tightly-packed spiral growth features, irregular step edges and V-defects.

This image shows the characteristic features of AlInGaN films: irregular step edges, spiral growth "islands" abutting one another, sparse hillocks taller than their surroundings, and V-defects at the intersection between threading dislocations and the material surface. These morphological features do not look similar to most GaN films grown by MOCVD, but resemble the dislocation-mediated surface morphology as described by Heying, *et. al.* for GaN films growth by molecular beam epitaxy (MBE)[18] or for InGaN by MOCVD[23]. MBE films have spiral features due to pinning of growing step edges by dislocations, as in Figure 2.17.

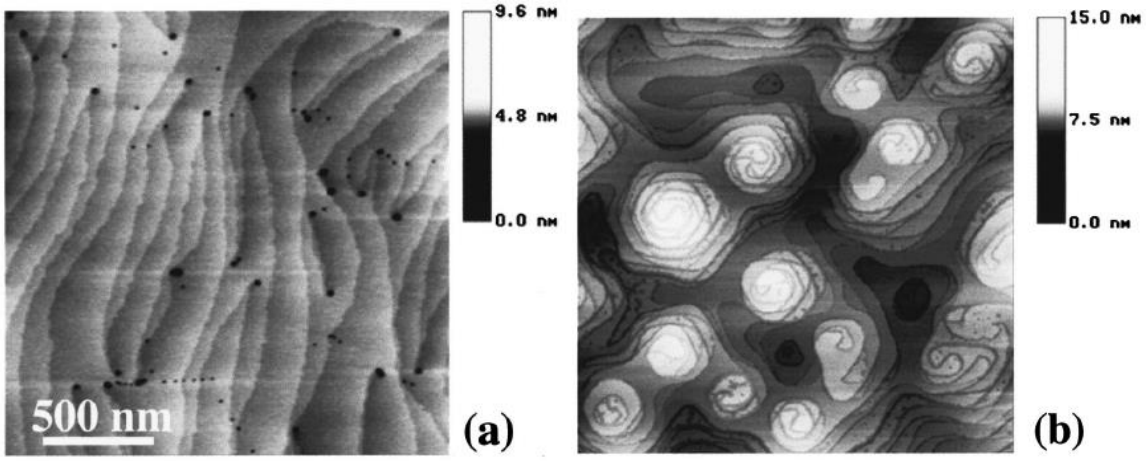

Figure 2.17a) shows the surface of MOCVD GaN; 2.17b) shows spiral growth of MBE-grown GaN[18].

The dislocation-mediated surface morphology was examined in a series of varying growth conditions through the lens of the theories developed by Burton, Cabrera and Frank[24]. Their work will be subsequently referred to as BCF theory. Heying, *et. al.* found that the comparing surface analysis between MOCVD and MBE films, as well as their growth conditions, was consistent with the tenets of BCF theory. Due to the similarity of AlInGaN morphology to MBE morphology, AlInGaN morphology was analyzed with reference to BCF theory. The points of BCF theory that are relevant to morphological analysis of AlInGaN films are as follows:

1. Spiral hillocks begin when two steps that are pinned together by a dislocation intersect. Spiral hillocks are comprised of two interlocking step ramps.
2. The formation condition for a spiral growth hillock is when the terrace width of a straight step (W_T) is greater than the terrace width of the two interlocking spiral ramps (W_{spiral}):

$$W_T > W_{spiral} = (4\pi\rho_c)/2 \tag{2.9}$$

3. The radius of curvature of the spiral growth hillock (ρ_c) is determined by the driving force for growth. The greater the driving force (further from equilibrium conditions), the tighter the spirals:

$$\rho_c = \frac{\gamma a}{k_b T \cdot \ln(P/P_0)} \tag{2.10}$$

In equation 2.10, the radius of curvature of the step-line curvature of the forming spiral is dependent upon surface tension, gamma, material monolayer height a, thermal energy k_bT (where k_b is the Boltzmann constant and T is temperature), P is the partial pressure of the growing material reactants in the vapor phase, and P_0 is the material's equilibrium vapor pressure. The term $k_bT \cdot \ln(P/P_0)$ can be considered the driving force for growth. If $P \approx P_0$, then

the surface is at near equilibrium (high temperature MOCVD GaN growth conditions), but if $P >> P_0$, then a large positive driving force is present, and the conditions for spiral growth formation are met (MBE and AlInGaN growth conditions). Since high temperature MOCVD growth occurs much closer to equilibrium than MBE, the spirals seen in MBE-grown GaN are not visible in MOCVD-grown GaN.

The MOCVD variables that affect P are f_{TMAl} and f_{TEGa}, which are the group III injection rates that have a direct relationship with growth rate. The MOCVD variables that affect P_0 are temperature and *V-III* ratio. In the case of InN, P_0 is also influenced by X_{AlN}. Since the growth conditions for AlInGaN are further from equilibrium than GaN, spiral growth must be expected. Therefore, lower P_0 and higher P should result in a higher density of small spiral growth features. As growth conditions get closer to thermodynamic equilibrium, spiral growth features and hillocks should become sparser.

2.3.2 V-III ratio

The changes in surface morphology with *V-III* ratio were the most obvious indicators of dislocation-mediated surface morphology at work. Figures 2.18a-d show that as *V-III* ratio increases, which causes P_0 to decrease and the driving force for growth to increase, the spiral growth features tighten up considerably. The decrease in radius of curvature of the spirals was expected from equation (2.10). Furthermore, the boxed areas of Figure 2.18a) and b) show that each spiral apex is comprised of a pair of pinned steps, as predicted by BCF theory[18,24].

Figure 2.18 also shows a variety of features that are unrelated to or unpredicted by BCF theory. The first, which may be explained by the reduction of the surface mobility of adatoms during growth, is the increasing irregularity of step edges with increasing *V-III* ratio. If the surface mobility of adatoms is low, then they may not be able to find their way to step edges

during growth and deposit on the terraces. This can cause step bunching and broadening of step terraces, which can be seen qualitatively in Figure 2.18a vs. Figure 2.18d. However, the wavy appearance of the step flow is still unexplained. BCF theory uses thermodynamic arguments as the basis of spiral growth formation, so features that are due to surface kinetics would be outside the scope of the theory. It was also unexpected that V-defects do not appear at the apex of many spiral growth features. However, dislocations in the III-N system that intersect with the surface do not necessarily expand into V-defects[18,25].

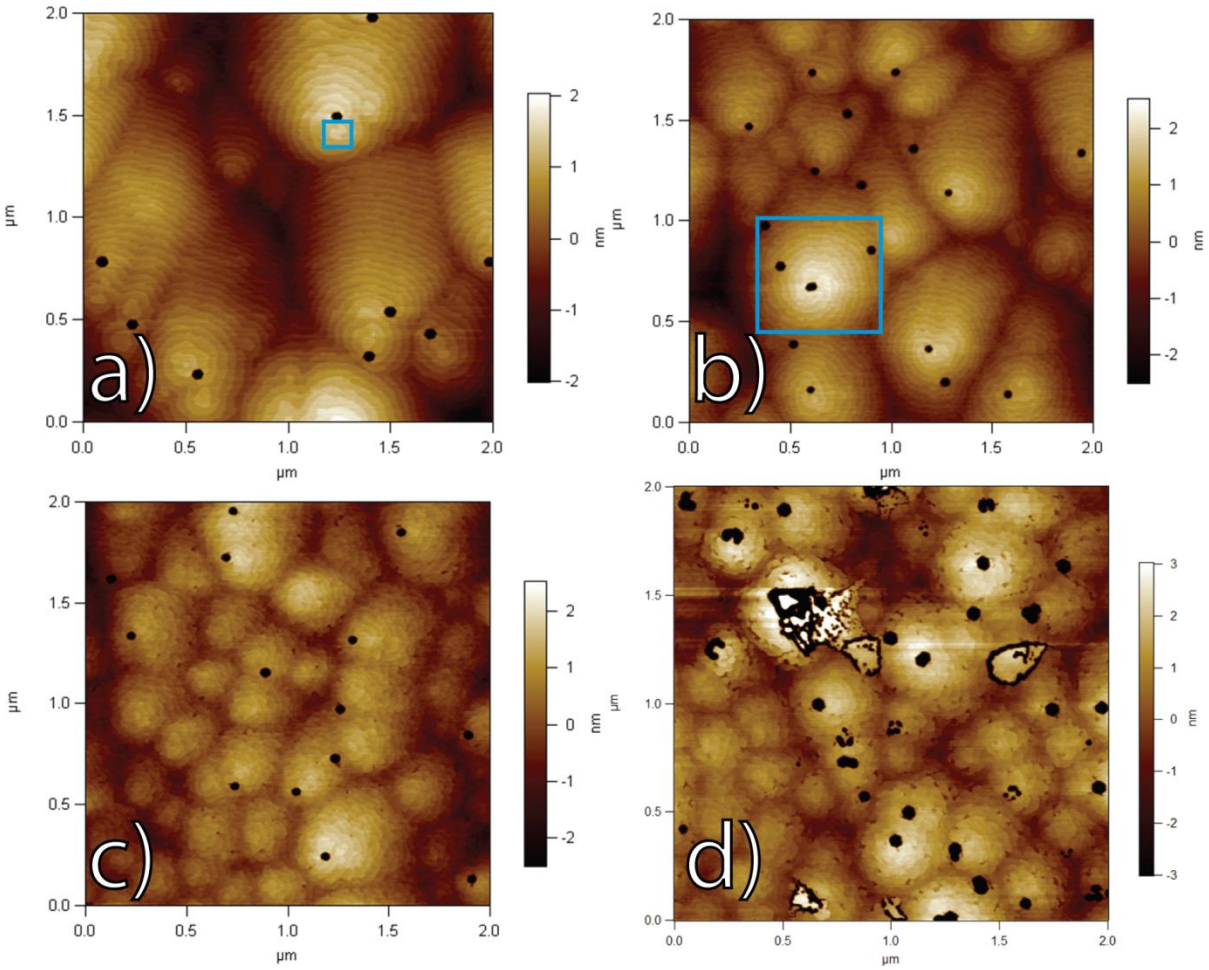

Figure 2.18a)-d) shows AFM images of AlInGaN films ordered by increasing *V-III* ratio (see section 2.2.3). With increasing *V-III*, spiral ρ_c decreases, V-defect diameter increases, step flow becomes irregular, and non-crystallographic features appear (18d). Areas highlighted with the blue box show the pinned steps (18a) and interlocking spiral ramps (18b) that are characteristic of dislocation-mediated surface morphology.

With increasing *V-III* ratio, a widening of V-defects was also observed, which may have been related to the enhanced indium uptake at elevated NH_3 flow rates. Larger XInN makes for larger lattice constants and higher lattice mismatch (greater strain). Another feature that must be noted here were the non-crystallographic objects embedded in the surface of the crystal at very high *V-III* ratio (Figure 2.18d). Adding ~200 standard cubic centimeters per minute (sccm) of H_2 gas flow during growth eliminated these features and also decreased the X_{InN} of the AlInGaN film. Due to their sensitivity to H_2 gas, these non-crystallographic features were believed to be indium metal or a separate phase of material with very high X_{InN}[26,27].

2.3.3 Growth rate

The effects of growth rate on the dislocation-mediated surface morphology of AlInGaN films can be convoluted by changes in crystal composition, such as how high X_{AlN} can decrease surface mobility of adatoms[5,28,29] and increase the impact of growth kinetics on morphology, or how differences in layer thickness can yield changes in step flow appearance. The best way to analyze the effect of growth rate on dislocation-mediate surface morphology would be to compare samples that have identical *FRR*, *V-III* ratio, growth temperature, and layer thickness. Unfortunately, a specific series with these controls was not performed when mapping out the growth space. Therefore, the growth rate dependence of spiral growth features was assessed in case studies where effects unrelated to BCF theory were not controlled for, but acknowledged in comparison between samples. An example of this is not controlling for layer thickness: while thicker layers may have irregular step edges and taller spiral growth hillocks, BCF theory is specifically oriented toward the density of pinned steps and spiral growth features. Assessing the impact of growth rate on dislocation-mediated surface morphology

focused on this metric. Other morphological features unrelated to BCF, but characteristic to the growth rate will also be described.

Consider two samples: sample A grown at 1.6 nm/min with a composition of $Al_{0.26}In_{0.072}Ga_{0.668}N$, and sample B grown at 3.3 nm/min with a composition of $Al_{0.25}In_{0.088}Ga_{0.662}N$. Being nearly compositionally identical, these samples were good candidates for comparing surface morphology. In Figure 2.19a and 2.19b, the AFM scans of sample A show evidence of step pinning at circular plateaus (highlighted by red circles). Sample A also had straight, parallel step flow growth over a significant portion of its area (highlighted by a blue rectangle). The small-area scan in Figure 2.19b, very clearly shows two pinned steps surrounding a dislocation, but the step flow is straight and parallel in areas surrounding it.

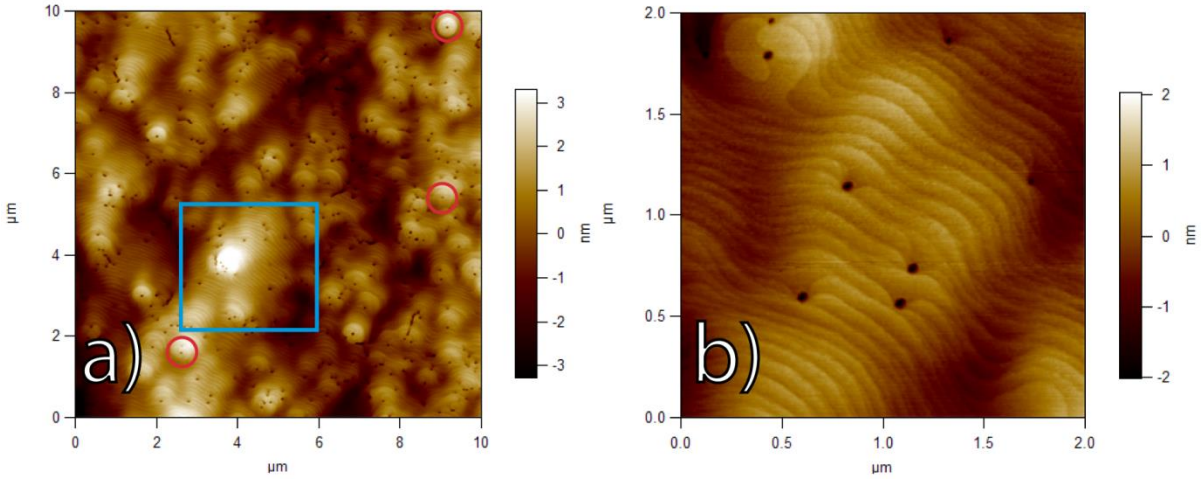

Figure 2.19 shows the step-flow morphology of $Al_{0.26}In_{0.072}Ga_{0.668}N$ with a growth rate of 1.61 nm/min. In 19a), there are several wide areas of smooth step flow growth (blue rectangle), and circular plateaus associated with pinned steps are circled in red. In 19b), the small area of the scan highlights details of both types of features in the sample – pinned steps that can lead to spiral growth surrounded by an area of parallel step flow.

When sample thickness was increased to 150 or 300 nm, as in Figure 2.20, it was apparent that the pinned step plateaus grew into spiral growth hillocks. Furthermore, in spite of the

irregularity in step edges, the spiral growth hillocks were surrounded by expansive areas of uninterrupted step flow growth. This was reflected in the RMS roughness of the samples. The RMS roughness increased from Figure 2.20a to 2.20b, but was mainly due to increase in hillock height in the large-area scans. On a 2x2 µm scale, in a region free from any spiral growth hillocks, the RMS roughness of the sample surface for 300-nm-thick AlInGaN film was still just 0.4 nm.

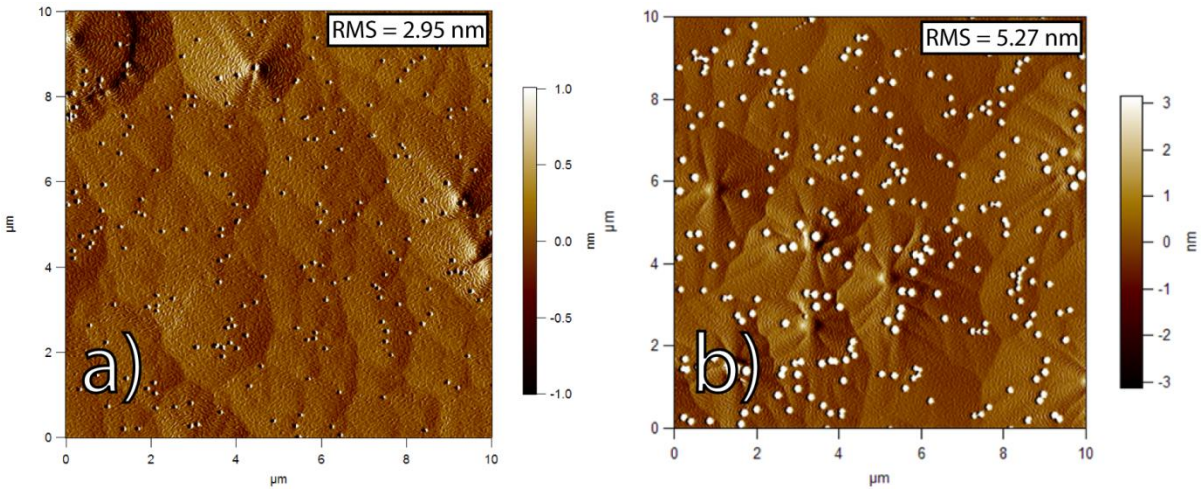

Figure 2.20 shows the morphology for AlInGaN with 150 nm thickness (a) and 300 nm thickness (b). Amplitude scans are shown to capture detail in the tall hillocks and orientation of the step flow. RMS roughness values of the height scan included for reference. Step flow is concentric with the hillock only in its immediate area.

Now consider the AFM images for sample B in Figure 2.21, which had a higher growth rate than sample A. From the 10x10 µm scan it is apparent that much less of the scan area is comprised of parallel step flow growth as compared with sample A. Furthermore, the density of pinned steps, as well as the circular pinned step plateaus, is higher than sample A. In the 2x2 µm scan, the wavy nature of the step flow can be seen in more detail, as well as the high density of paired pinned steps, which can indicate a starting point for spiral growth hillocks. Another feature that presented itself in the highest growth rate sample was non-

crystallographic objects embedded in the sample surface. Interestingly, these objects appeared to be identical to those in Figure 2.18d from the *V-III* ratio series. Furthermore, if f_{TEGa} was kept to a low enough flow rate that ensures smooth surfaces (low r_g*(GaN)*), but f_{TMAl} was increased such that r_g*(AlN)* was higher than called for by InAlN growth conditions (~ 1 nm/min), these non-cyrstallographic features once again reappeared.

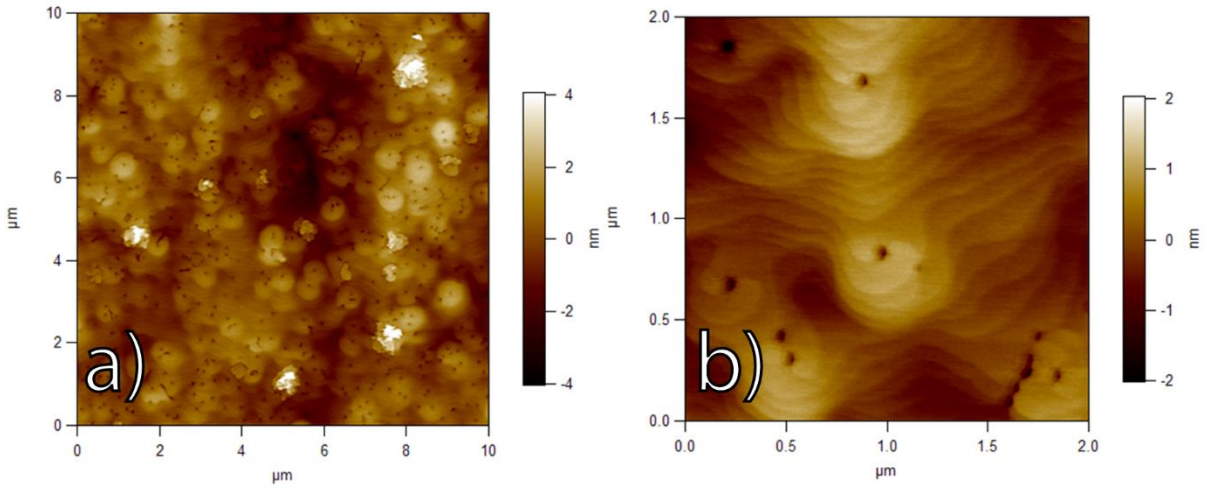

Figure 2.21 shows the morphology for a 70 nm $Al_{0.25}In_{0.088}Ga_{0.662}N$ sample with r_g = 3.3 nm/min. There is a higher pinned step density than sample A (Figure 2.19), and also shows non-crystallographic surface features.

Another case study to consider was between $Al_{0.34}In_{0.12}Ga_{0.54}N$ grown at 1.88 nm/min (sample C, Figure 2.22a) and $Al_{0.44}In_{0.12}Ga_{0.44}N$ grown at 2.26 nm/min (sample D, Figure 2.22b). The difference in growth rates was achieved by increasing f_{TMAl}. AFM scans for sample C are in Figure 2.22a, and those for sample D are in Figure 2.22b. Just as with the *V-III* ratio series, as the growth conditions were driven away from equilibrium (higher growth rate), the density of spiral growth features increased and their radius of curvature decreased. However, unlike the *V-III* ratio series, there was no change in the small scale step flow. This may be due to the relatively high X_{InN} and thickness (~100 nm) in both samples C and D, as well as a high *V-III* ratio of ~7900.

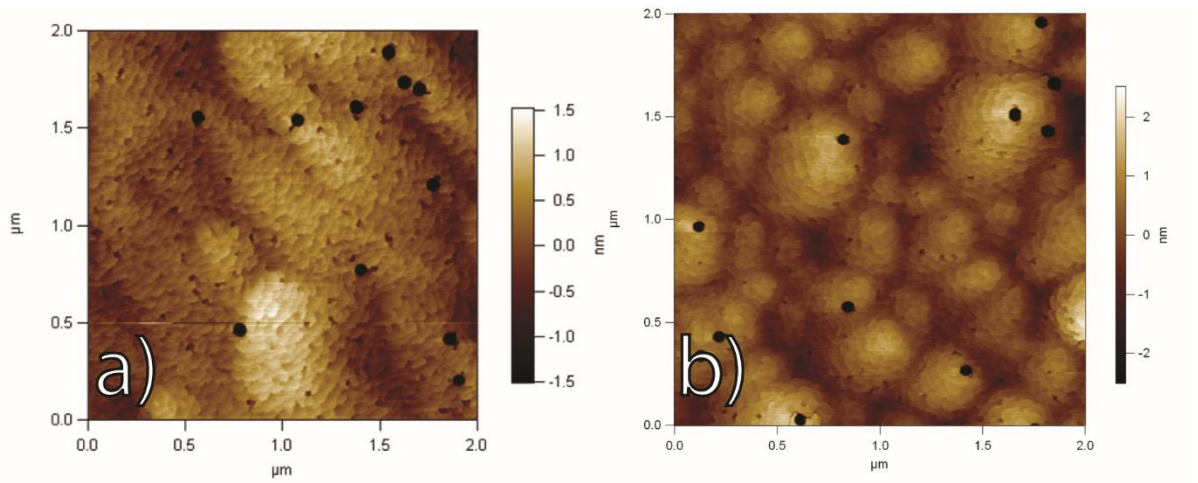

Figure 2.22. The AFM of sample C (a) versus sample D (b) shows an increase in spiral growth feature density. Changes in morphology from a continuous-looking layer to islands may also be due to the higher X_{AlN} and lower surface mobility of adatoms in sample D.

Another effect to keep in mind when comparing samples C and D was the difference in X_{AlN}. From section 2.2.1, it was known that increasing X_{AlN} causes X_{InN} to increase sympathetically. Therefore, borrowing terminology from BCF theory, P_0 must decrease with increasing X_{AlN} if a greater aluminum content in the crystal helps prevent InN desorption. Furthermore, the high bond strength of aluminum will decrease adatom surface mobility with increasing X_{AlN}[5,29]. These effects of aluminum concentration in the crystal may have had additional influence on the surface morphology of the crystal, and contributed to the change in morphology between Figures 2.22a and 2.22b. Nonetheless, it is clear that samples with high X_{AlN} preferred a morphology comprised of tightly packed islands, where each island appeared to grow via spiral growth (i.e. Figures 2.18 and 2.22b).

2.3.4 Temperature

The effect of temperature changes on the AlInGaN film morphology was best observed in 10x10 um AFM scans. There was a variety of large- and small-scale features that changed

in AlInGaN films with temperature. To highlight them all, amplitude scans are shown in Figure 2.23 because height scans would not be able to capture both the nature of the step flow and the size (and shape) of large hillocks simultaneously. For reference, the RMS roughness values calculated from the height scan were included with each amplitude scan.

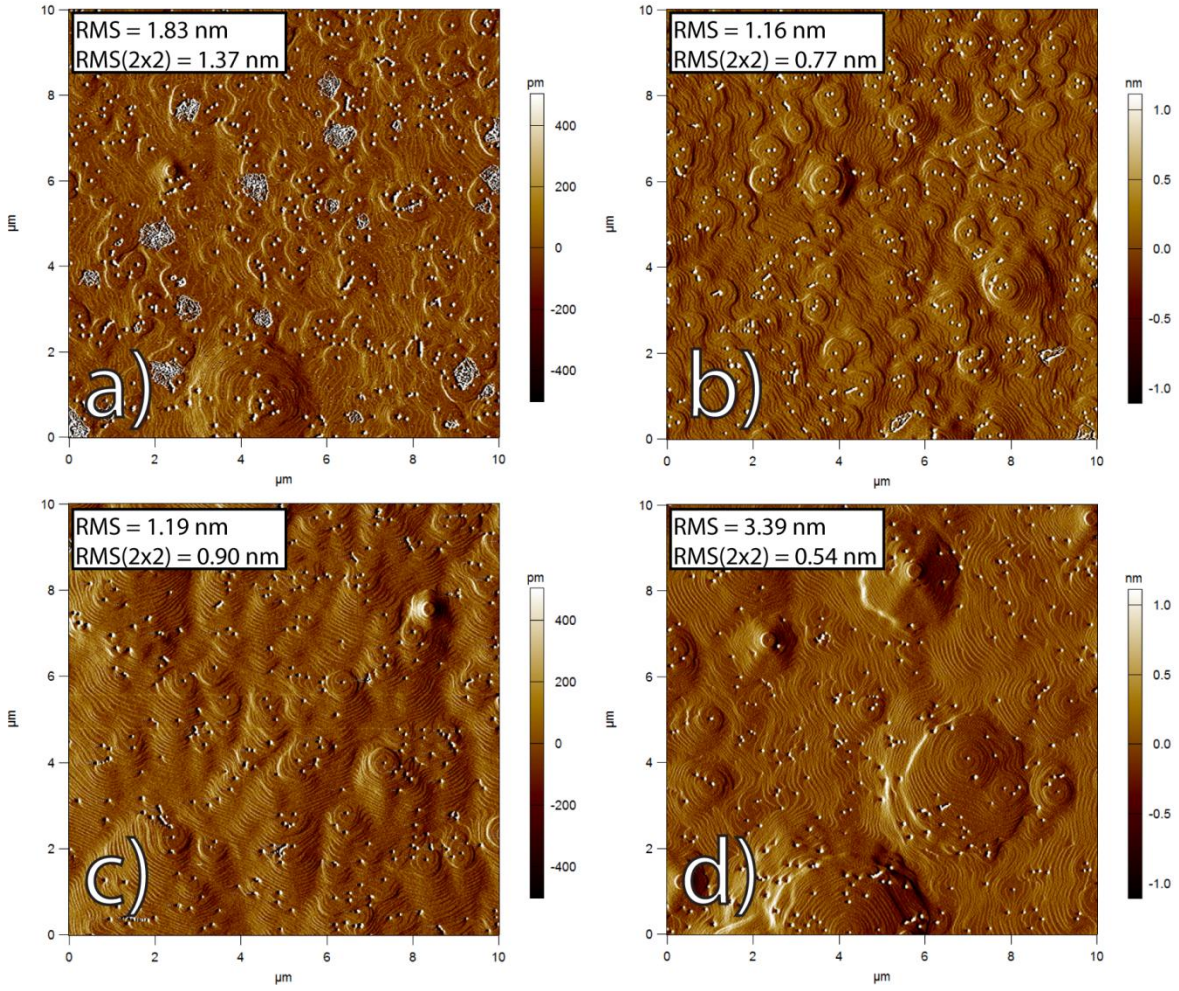

Figure 2.23 shows the surface morphology for AlInGaN films as a function of temperature. Samples here correspond to the series in section 2.2.2; compositions are given in Figure 2.10. Images are order of increasing temperature with (a) at the lowest and (d) at the highest. RMS roughnesses from height scans are included.

The lowest-temperature sample in Figure 2.23a shows the highest density of pinned steps, most irregular step flow, worst RMS roughness, and non-crystallographic features embedded in the surface. By increasing the temperature, Figure 2.23b shows that the non-

crystallographic features disappeared, but the pinned step density was still large. Figure 2.23c shows another reduction in pinned step density by increasing temperature. Finally, the highest-temperature sample showed very orderly step flow growth aside from sparse and large spiral growth hillocks. This last sample revealed that with a lower overall density of pinned steps, which are the precursors to spiral growth hillocks, the pinned steps that do form have much more room to grow into hillocks without coming into contact with competing spiral growth features. Thus, the sample with highest growth temperature, in Figure 2.23d, actually had the largest hillocks protruding from the sample surface, reaching up to 30 nm in height past the planar portion of the sample surface, and over 2 μm in diameter.

Also quoted in Figure 2.23 were the RMS roughness values from a 2x2 μm section of each scan area. These 2x2 μm sections were intentionally chosen to be devoid of hillocks or non-crystallographic features, with the goal of capturing the nature of the step flow. Measurements from AFM of the small-scale sections showed that the surface roughness decreased with increasing temperature. Therefore, if the large-scale features that evolved on the surface were ignored, increasing temperature served to recover step flow reminiscent of high-temperature GaN and reduce surface roughness over short length scales.

2.3.5 Composition

The final relationship to examine was the change in surface morphology with crystal composition. AFM scans were collected from samples with varying X_{InN} and X_{AlN} from a variety of growth conditions. The variables that were held constant were film thickness and NH_3 flow. All of the samples compared here had film thicknesses of 95-115 nm, and NH_3 flow was held constant at 4 slm. This resulted in *V-III* ratio values varying between 7900 and 9412.

The sample with the lowest X_{InN} would have a high gas-phase supersaturation, but was also grown at the highest temperature. From equation 2.10, the strong temperature dependence of spiral formation (compared to $\ln(P/P_0)$) suggests that this sample would have the nearest-to-equilibrium growth conditions. This sample showed step flow most reminiscent of high-temperature GaN on a small scale, but yielded very broad spiral growth hillocks on long length scales (Figure 2.24a). Lowering the growth temperature allowed more indium to incorporate into the crystal (Figure 2.24b). This also resulted in irregular step flow and increased density of spiral growth features. With the increase in spiral density, the sample's overall flatness in large-area AFM scans increased. Increasing the *FRR* in favor of higher X_{AlN} resulted in the film described in Figure 2.24c. The nature of the step flow on the small scale did not change, which means that this morphological feature must be some function of indium content in the crystal as well as film thickness. This feature is not described by dislocation-mediated surface morphology, and may be more related to growth kinetics or strain relaxation. Also notice that in Figure 2.24c, the island-like nature of the film is much more pronounced, with each island appearing to be its own spiral growth feature (as mentioned in section 2.3.2). This is evidence of high-X_{AlN} increasing the stability of the growing crystal. Therefore, in comparison to a low-X_{AlN} film, the effective supersaturation of reactants in the gas phase is higher, yielding a larger driving force for growth and a smaller radius of curvature for spiral growth features.

The final change in composition was to eliminate f_{TEGa} entirely to obtain $In_{0.18}Al_{0.82}N$ in Figure 2.24d. This appeared to be the final evolution of the morphological changes to the AlInGaN crystal. InAlN films show a morphology where InAlN islands decorate the step terraces that were created by the underlying GaN template growth. However, with the extremely high X_{AlN} in the crystal, the kinetic effects of adatoms must be taken into account.

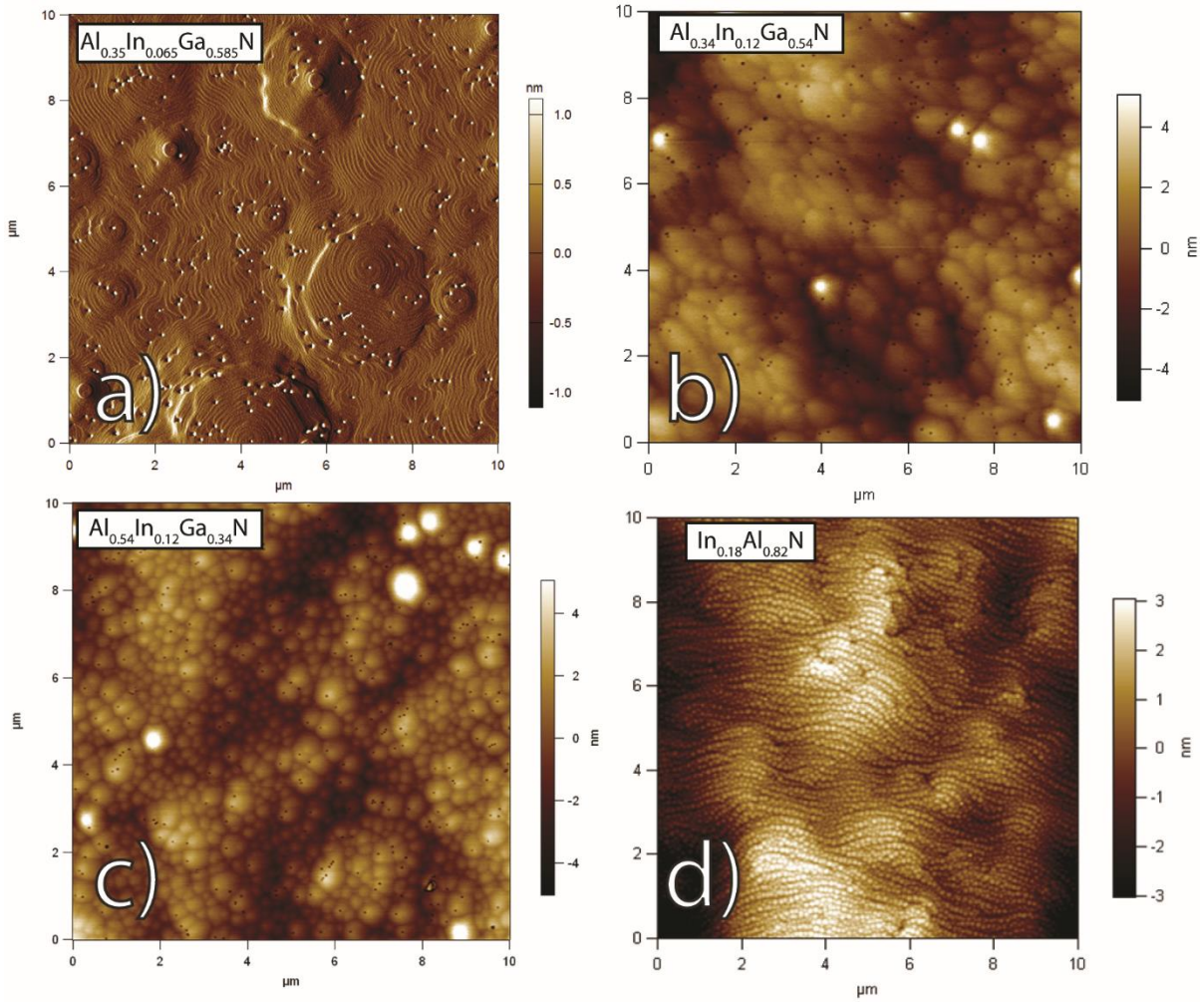

Figure 2.24 shows changes in surface morphology with increasing X_{AlN} and X_{InN}.

According to previous findings, this type of morphology is only possible under the presence of a liquid indium adlayer that promotes enhanced surface migration of the aluminum adatoms[12]. However, the InAlN and all AlInGaN films presented here had identical f_{TMIn} of 15.28 µmol/min, and were grown at similar temperatures. If this explanation were the case and the growth was so kinetically limited, it would not explain the dramatic differences between InAlN surface morphology and the variety of morphologies displayed in the AlInGaN system. However, it is also difficult to describe the morphology present in InAlN as being dominated by spiral growth or dislocation-mediated surface morphology. Thus, the dominant

growth mechanisms for AlInGaN films with low X_{GaN} require further investigation, as does understanding their relationship to InAlN.

2.4 GROWING DEVICE-GRADE MATERIAL

2.4.1 Recipe stability

TABLE I shows the run-to-run repeatability of AlInGaN recipes with various X_{AlN} and X_{GaN} compositions. The excellent process stability is an encouraging foundation for the development of new technology.

	Recipe A		**Recipe B**		**Recipe C**	
	5/8/2013	**6/3/2013**	**5/8/2013**	**6/3/2013**	**5/13/2013**	**6/7/2013**
r_g (nm/min)	1.88	1.88	2.2	2.26	1.3	1.3
X_{AlN}	0.354	0.34	0.44	0.42	0.534	0.504
X_{GaN}	0.536	0.54	0.439	0.44	0.344	0.357
X_{InN}	0.11	0.12	0.121	0.14	0.122	0.139
RMS roughness (nm)	1.40	1.43	1.27	1.47	1.72	1.43

In addition to establishing the growth window for AlInGaN films, it was also necessary to evaluate the process stability under these growth conditions. This was done by repeating identical growth recipes one month after the initial growth was performed. Growth rate, crystal composition by SIMS, and RMS roughness of the films in a 10x10 μm scan area were compared between pairs of samples for a variety of X_{AlN} and X_{GaN} values. The results are summarized in TABLE I. The measurable material properties were all very consistent over a month's time for each recipe. Process consistency is critical for high experiment throughput,

since a more inconsistent process requires more frequent calibration growths, and for developing technology based upon AlInGaN materials.

2.4.2 Impurity analysis

Impurity analysis was also performed on initial AlInGaN growths via SIMS to evaluate the background concentration of carbon and oxygen impurities. High concentration of oxygen impurities in the crystal is correlated with high device leakage current, and results in ionized impurities in the depletion region of devices. Carbon impurities can cause a wide range of deleterious effects, including poor luminescence in InGaN active regions[30], yellow luminescence in GaN buffers[31,32], current collapse in HEMTs[33,34], and other deleterious effects associated with deep levels (such as defect-related tunneling through regions in depletion regions)[33–36]. In Figure 2.25, the SIMS scan shows that [C] ~ $1 \cdot 10^{17}$ cm^{-3} and [O] ~ $3 \cdot 10^{17}$ cm^{-3} for $Al_{0.26}In_{0.072}Ga_{0.668}N$. For the sake of comparison, lattice-matched InAlN has an oxygen impurity level of $2 \cdot 10^{18}$ cm^{-3}, and a carbon impurity level of $3 \cdot 10^{17}$ cm^{-3} [12].

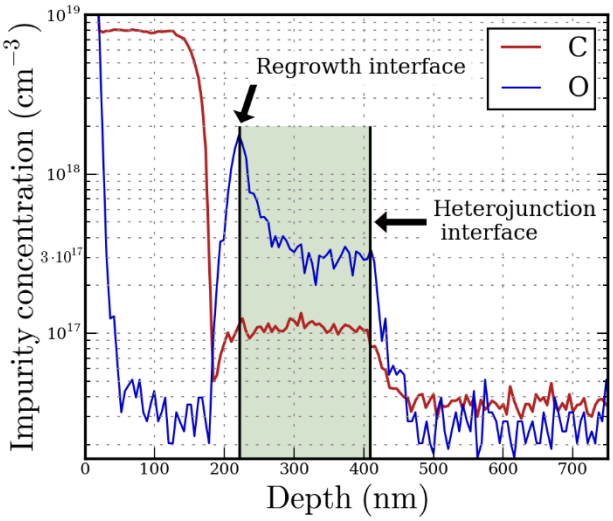

Figure 2.25 shows the SIMS scan of carbon and oxygen impurities in AlInGaN performed at Evans Analytical Group. The shaded region is the AlInGaN epilayer that was grown on a GaN template and buried beneath a GaN cap formed by regrowth.

Oxygen and carbon concentration in the crystal will be a function of growth conditions and crystal composition, but this gave an adequate ballpark for the purposes of device design and future growth experiments. Subsequent current-voltage (*I-V*) experiments on Schottky diode samples revealed that high impurity concentrations can also be a limiter of the growth space. It is well-documented that [C] and [O] increase with decreasing *V-III* ratio[8], but from Figure 2.18 it is seen that low *V-III* ratio also yielded films with excellent surface morphology. In spite of the excellent morphology, when testing Schottky diodes that were fabricated from material growth with a low *V-III* ratio of 2304 (corresponding to a NH_3 flow of 1 slm), it was found that they had extremely high reverse bias leakage. The source of that leakage is believed to be the high impurity levels that are likely to exist in the crystal.

In a similar vein, it was discovered that samples with very high *V-III* ratio (i.e. samples grown under conditions identical to the sample in Figure 2.18d) also produced Schottky diodes that were shorts or near-shorts. In the case of the samples with *V-III* ratio $\geq$ 11518 (NH_3 flow of 5 slm), the source of leakage was believed to be the particles embedded into the surface of the material. Thus for the purposes of electronic devices, the *V-III* ratio must not be too low, nor too high.

2.4.3 Major take-away: the optimal growth window

The ultimate goal of these various growth series was to determine the overarching set of conditions necessary to produce material with high enough quality for use in electronic and optoelectronic devices. With that in mind, contained here is a compilation of guidelines and constraints, established in the previous sections, for the production of material with highest possible quality.

First, a *V-III* ratio must be chosen. The rule of thumb to be used for this is that the minimum *V-III* is always desirable provided that electrical performance does not suffer. In section 2.4.2, it was established that high leakage currents were presented at both low (2304) and high (11518) *V-III* ratios. Therefore, an acceptable range can be found between 4607 and 9214, which corresponds to a NH_3 flow of 2-4 slm. With a *V-III* ratio chosen for growth, X_{AlN} may be determined and calibrated using the TMAl-TEGa *FRR* (section 2.2.1). Then, the temperature can be modulated to finely tune the X_{InN} of the crystal to achieve the desired composition.

From the morphological studies, it was discovered that growing too fast, too cold, or at too high of a *V-III* ratio all resulted in the same system: non-crystallographic features embedded into the sample surface. While they occur under a variety of growth conditions, lower *V-III* ratio helped prevent their formation. It is possible that going to slower growth rates at lower temperatures may also help prevent the formation of these features. Furthermore, including trace amounts of hydrogen during growth was found to reduce the size and density of these features on the sample surface. Unfortunately, it was also accompanied by a decrease in the X_{InN} of the resulting crystal. The hydrogen sensitivity of these surface features indicated that they may be indium-rich. Consequently, lowering the f_{TMIn} for the conditions which presented these non-crystallographic features may help prevent their formation without negatively impacting the X_{InN} of the crystal (unlike using H_2, which does affect X_{InN}). It should be noted that these features are not observed on InAlN surfaces.

The morphological studies also showed evidence of a dislocation-mediated surface morphology in which spiral growth hillock growth is unavoidable. By varying the growth conditions, it was possible to modify the size and density of these hillocks. However, the

characteristics of the hillocks were most sensitive to temperature and *V-III* ratio. Since temperature is critical for achieving the desired crystal composition, *V-III* ratio must be relied upon to generate films with the best possible surface morphology. Furthermore, in Figure 2.24, it is also apparent that the spiral- and island-like morphology became more densely packed simply by increasing X_{AlN}. Miscut c-plane substrates could provide an avenue for inhibiting spiral growth, but miscut substrates yield GaN templates with worse crystalline quality[37,38]. Fortunately, the irregular step flow and dense island morphology expressed in samples grown with high X_{AlN}, or far from thermodynamic equilibrium, has not had a negative effect on the transport properties of the materials. In Chapter 4, the reader will see Schottky diode samples with morphology similar to Figure 2.24c, ideality factor < 1.25 at room temperature, and greater than six orders of magnitude of current rectification between forward and reverse bias.

Another trade-off to consider during growth is that higher *V-III* ratio recipes demand lower growth rate. In general, it was found that growth rates should be limited to less than 3 nm/min (based on results from section 2.3.3). However, if the growth rate is decreased too much, interface abruptness can degrade. The recipe must therefore be modified with respect to the application. For example, HEMTs would require a thin AlInGaN layer and maximum interface abruptness (i.e. minimum interface roughness), and would therefore call for the use of a higher growth rate. Devices that utilize thicker AlInGaN layers, with less of an emphasis on heterojunction abruptness, may benefit from slower growth rates. This is especially true for samples with high X_{AlN}, where surface kinetics can have a strong influence on the outcome of growth. However, for all future device work, total AlInGaN thickness should be kept under 300 nm. Figure 2.4 shows the large diameter of V-defects and extremely tall spiral hillock

peaks. While electrical transport in AlInGaN films is surprisingly tolerant to V-defects and non-ideal surface morphology, Figure 2.4 shows the limit of what can be considered acceptable.

2.5 CONCLUSIONS

Crystal growth is a complex, multi-variable problem. Understanding of, and control over, multiple input parameters must be exercised simultaneously in order to realize the goal of fabricating high-performance heterojunction-based devices. The development of AlInGaN growth described in this chapter has been a first for UCSB. Compositional control of the crystal has been demonstrated over a wide range of X_{AlN} and X_{InN} values, as well as for a variety of growth conditions. Not only that, but the sympathetic incorporation of indium with increasing X_{AlN} has been documented and can be compensated for, resulting in independent control over X_{AlN} and X_{InN} in MOCVD growth. SIMS analysis revealed that the resulting films have sufficiently low impurity levels for incorporation into electronic and optoelectronic devices. Furthermore, constraints on growth conditions have been established to ensure good surface morphology, and growth process stability was demonstrated over the course of a month. The confluence of these factors is the ability to grow device-grade material by MOCVD, and the subsequent chapters will not only verify excellent performance of HEMTs and Schottky diodes, but will also cover detailed analysis of their electrostatic and transport properties.

The capability now exists to perform a wide variety of experiments that require compositional control over AlInGaN films. It is possible to grow graded structures for electric field engineering in devices via polarization control, such as: layers of 3DEG or 3DHG charge slabs, n-i-n diodes, polarization-dipole-based diodes, tunnel junctions, and more[39–45]. Furthermore, and more to the point of this thesis, it is possible to design experiments to

ascertain the unknown material parameters of the AlInGaN system. Experimental reports of net polarization charges at interface, Schottky barrier heights, and conduction band discontinuity are sparse or non-existent in spite of the critical role that these parameters play in device design. Additionally, once these parameters are understood, it will be possible to create experiments that probe electron transport in AlInGaN bulk films, as well as at heterojunction interfaces. There remains a wide breadth of fruitful research areas within MOCVD growth of AlInGaN. Please refer to Chapter 5 to see recommendations for future investigation, as well as some data from growth projects that are just beginning.

2.6 REFERENCES

[1] S. Keller, B.P. Keller, D. Kapolnek, A.C. Abare, H. Masui, L.A. Coldren, U.K. Mishra, and S.P. Den Baars, Appl. Phys. Lett. **68**, 3147 (1996).

[2] J.E. Northrup, L.T. Romano, and J. Neugebauer, Appl. Phys. Lett. **74**, 2319 (1999).

[3] X.H. Wu, C.R. Elsass, A. Abare, M. Mack, S. Keller, P.M. Petroff, S.P. DenBaars, J.S. Speck, and S.J. Rosner, Appl. Phys. Lett. **72**, 692 (1998).

[4] Y. Chen, T. Takeuchi, H. Amano, I. Akasaki, N. Yamada, Y. Kaneko, and S.Y. Wang, Appl. Phys. Lett. **72**, 710 (1998).

[5] G. Parish, Growth and Characterization of Aluminium Gallium Nitride / Gallium Nitride Ultraviolet Detectors, University of California, Santa Barbara, 2001.

[6] S. Ruffenach-clur, O. Briot, and J.L. Rouvie, Mater. Sci. Eng. B **50**, 219 (1997).

[7] H. Li, S. Keller, S.H. Chan, J. Lu, S.P. DenBaars, and U.K. Mishra, Semicond. Sci. Technol. **30**, 055015 (2015).

[8] N.A. Fichtenbaum, T.E. Mates, S. Keller, S.P. DenBaars, and U.K. Mishra, J. Cryst. Growth

310, 1124 (2008).

[9] S.C. Cruz, S. Keller, T.E. Mates, U.K. Mishra, and S.P. DenBaars, J. Cryst. Growth **311**, 3817 (2009).

[10] M. Sumiya, K. Yoshimura, K. Ohtsuka, and S. Fuke, Appl. Phys. Lett. **76**, 2098 (2000).

[11] R.B. Chung, F. Wu, R. Shivaraman, S. Keller, S.P. DenBaars, J.S. Speck, and S. Nakamura, J. Cryst. Growth **324**, 163 (2011).

[12] R.B. Chung, Comprehensive Material Study of MOCVD Grown AlInN and Development of Relaxed Template for Ultraviolet Diode Lasers, University of California, Santa Barbara, 2011.

[13] G.B. Stringfellow, *Organometallic Vapor Phase Epitaxy: Theory and Practice*, Second (Academic Press, New York, 1999).

[14] Y.-L. Tsai, Cheng-Liang Wang, P.-H. Lin, Wei-Tsai Liao, and Jyh-Rong Gong, in *Int. Semicond. Device Res. Symp. 2003* (IEEE, 2003), pp. 98–99.

[15] K. Hiramatsu, Y. Kawaguchi, M. Shimizu, N. Sawaki, T. Zheleva, R.F. Davis, H. Tsuda, W. Taki, N. Kuwano, and K. Oki, MRS Internet J. Nitride Semicond. Res. **2**, (1997).

[16] J.E. Northrup, L.T. Romano, and J. Neugebauer, Appl. Phys. Lett. **74**, 2319 (1999).

[17] K. Godwood, M. Lefeld-Sosnowska, and E. Zielinska-Rohozinska, Phys. Status Solidi **7**, 445 (1964).

[18] B. Heying, E.J. Tarsa, C.R. Elsass, P. Fini, S.P. DenBaars, and J.S. Speck, J. Appl. Phys. **85**, 6470 (1999).

[19] B. Reuters, M. Finken, A. Wille, B. Holländer, M. Heuken, H. Kalisch, and A. Vescan, **093524**, 1 (2013).

[20] S. Keller, C.S. Suh, N.A. Fichtenbaum, M. Furukawa, R. Chu, Z. Chen, K. Vijayraghavan,

S. Rajan, S.P. DenBaars, J.S. Speck, and U.K. Mishra, J. Appl. Phys. **104**, 093510 (2008).

[21] M.A. Khan, J.W. Yang, G. Simin, R. Gaska, M.S. Shur, H.-C. zur Loye, G. Tamulaitis, A. Zukauskas, D.J. Smith, D. Chandrasekhar, and R. Bicknell-Tassius, Appl. Phys. Lett. **76**, 1161 (2000).

[22] R.A. Arif, R.S. Tummidi, Y.K. Ee, and N. Tansu, Phys. Simul. Optoelectron. Devices XV **6468**, 46803 (2007).

[23] S. Keller, U.K. Mishra, S.P. Denbaars, and W. Seifert, Japanese J. Appl. Physics, Part 2 Lett. **37**, 0 (1998).

[24] W.K. Burton, N. Cabrera, and F.C. Frank, Philos. Trans. R. Soc. A Math. Phys. Eng. Sci. **243**, 299 (1951).

[25] A. Hierro, M. Hansen, J.J. Boeckl, L. Zhao, and J.S. Speck, Analysis **946**, 937 (2001).

[26] A. Koukitu, T. Taki, N. Takahashi, and H. Seki, J. Cryst. Growth **197**, 99 (1999).

[27] S. Keller and S.P. DenBaars, J. Cryst. Growth **248**, 479 (2003).

[28] M. Gherasimova, G. Cui, Z. Ren, J. Su, X.L. Wang, J. Han, K. Higashimine, and N. Otsuka, J. Appl. Phys. **95**, 2921 (2004).

[29] S. Porowski and I. Grzegory, *"Phase Diagram of AlN." Properties of Group III Nitrides* (INSPEC, London, 1994).

[30] H. Masui, S. Keller, N. Fellows, N. a. Fichtenbaum, M. Furukawa, S. Nakamura, U.K. Mishra, and S.P. DenBaars, Jpn. J. Appl. Phys. **48**, 071003 (2009).

[31] J.L. Lyons, A. Janotti, and C.G. Van de Walle, Appl. Phys. Lett. **97**, 152108 (2010).

[32] Y. Saitoh, K. Sumiyoshi, M. Okada, T. Horii, T. Miyazaki, H. Shiomi, M. Ueno, K. Katayama, M. Kiyama, and T. Nakamura, Appl. Phys. Express **3**, 081001 (2010).

[33] P.B. Klein, S.C. Binari, K. Ikossi, A.E. Wickenden, D.D. Koleske, and R.L. Henry, Appl.

Phys. Lett. **79**, 3527 (2001).

[34] M.J. Uren, M. Silvestri, M. Casar, G.A.M. Hurkx, J.A. Croon, J. Sonsky, and M. Kuball, IEEE Electron Device Lett. **35**, 327 (2014).

[35] C. Poblenz, P. Waltereit, S. Rajan, S. Heikman, U.K. Mishra, and J.S. Speck, J. Vac. Sci. Technol. B **22**, 1145 (2004).

[36] A.R. Arehart, T. Homan, M.H. Wong, C. Poblenz, J.S. Speck, and S.A. Ringel, Appl. Phys. Lett. **96**, 242112 (2010).

[37] T.Y. Uasa, Y.U. Eta, Y.T. Suda, and A.O. Gawa, **38**, 703 (1999).

[38] K. Hiramatsu, H. Amano, and I. Akasaki, J. Cryst. Growth **107**, 509 (1991).

[39] S. Keller, C.S. Suh, Z. Chen, R. Chu, S. Rajan, N.A. Fichtenbaum, M. Furukawa, S.P. DenBaars, J.S. Speck, and U.K. Mishra, J. Appl. Phys. **103**, 033708 (2008).

[40] S. Rajan, M. Wong, Y. Fu, F. Wu, J.S. Speck, and U.K. Mishra, Jpn. J. Appl. Phys. **44**, L1478 (2005).

[41] D. Jena, J. Simon, A. Wang, Y. Cao, K. Goodman, J. Verma, S. Ganguly, G. Li, K. Karda, V. Protasenko, C. Lian, T. Kosel, P. Fay, and H. Xing, Phys. Status Solidi Appl. Mater. Sci. **208**, 1511 (2011).

[42] M.A. Khan, J.W. Yang, G. Simin, R. Gaska, M.S. Shur, and A.D. Bykhovski, Appl. Phys. Lett. **75**, 2806 (1999).

[43] G. Gupta, M.A. Laurent, J. Lu, S. Keller, and U.K. Mishra, Appl. Phys. Express **7**, 014102 (2014).

[44] H. Hahn, B. Reuters, A. Wille, N. Ketteniss, F. Benkhelifa, O. Ambacher, H. Kalisch, and A. Vescan, Semicond. Sci. Technol. **27**, 055004 (2012).

[45] M.F. Schubert, J. Xu, J.K. Kim, E.F. Schubert, M.H. Kim, S. Yoon, S.M. Lee, C. Sone, T.

Sakong, and Y. Park, Appl. Phys. Lett. **93**, (2008).

Chapter 3

POLARIZATION AND POLARIZATION ENGINEERING IN AlInGaN/GaN HETEROJUNCTIONS

3.1 MOTIVATION: IMPACT OF POLARIZATION ON BAND DIAGRAM

With the MOCVD growth space well-established by the results of Chapter 2, the next stage of AlInGaN development was to establish the toolbox of material parameters necessary for device engineering. The first material parameter that was chosen for investigation was the net interfacial polarization charge at AlInGaN/GaN interfaces. The discontinuity in polarization charge, and therefore the discontinuity in electric field in a device structure, is interesting effect in III-N heterojunctions. It is particularly interesting in the case of AlInGaN-based heterojunctions because of the wide range of values that this net interfacial polarization charge can take on[1–3].

Polarization in III-N materials is due to the polar nature of nitride materials' wurtzite crystal structure, and is directly related to the strain and composition of the crystal[4–7]. By modulating the relative AlN (Y_{AlN}) and InN (Z_{InN}) fractions in the crystal it is possible not only to control the strain of the epitaxial film, and therefore the piezoelectric polarization of the material, but also the spontaneous polarization of the material. More succinctly,

$$P_{\mathrm{TOT}} = P_{\mathrm{PZ}}(X_{\mathrm{GaN}}, Y_{\mathrm{AlN}}, Z_{\mathrm{InN}}) + P_{\mathrm{SP}}(X_{\mathrm{GaN}}, Y_{\mathrm{AlN}}, Z_{\mathrm{InN}}) \tag{3.1}$$

can be controlled during epitaxial growth, which paves the way for polarization engineering in III-N electronics and optoelectronics. In the ternary alloys, two group III species are used to

modify the properties of the epitaxial films. For any composition of A_XB_YN, it is only possible to have one combination of P_{TOT}, E_g, and strain to the substrate, $\Delta a/a_o$. Utilizing AlInGaN/GaN heterojunctions in device design, however, means combinations of P_{TOT}, E_g, and $\Delta a/a_0$ are not unique. This yields an increase in the number of degrees of freedom in material properties that may be exploited in device design.

In order to effectively design polarization-engineered devices, it is necessary to have an accurate estimation of P_{TOT}, E_g, $\Delta a/a_o$, since they all influence the band diagram. In the III-N system, the band diagram is inextricably related to the magnitude of the net polarization charge at heterointerfaces ($Q_\pi(net)$)[6].

$$Q_\pi(net) = P_{TOT}(A) - P_{TOT}(B), \tag{3.2}$$

where A and B are two adjacent epilayers joined at a heterojunction. This can be between a HEMT barrier and the GaN substrate, quantum wells and barriers, or distributed over a region of graded material. In all cases, this net polarization charge strongly affects the electric fields present throughout device structure.

With quaternary alloys, one may choose to hold $\Delta a/a_o$ constant and vary $Q_\pi(net)$ while treating the band gap as a constraining variable (Figure 3.1a). Furthermore, though constrained by limitations due to strain between AlInGaN and GaN, the net interfacial polarization charge ($Q_\pi(net)$) may be varied while the band gap is kept constant (Figure 3.1b). This can be applied to the fabrication of enhancement-mode HEMTs, and optoelectronics in which the quantum-confined Stark effect is minimized via polarization-reduced MQW structures[8–12]. Due to the sensitive nature of controlling these device traits, an accurate estimation of $Q_\pi(net)$ becomes critical when one considers polarization engineering in devices[6].

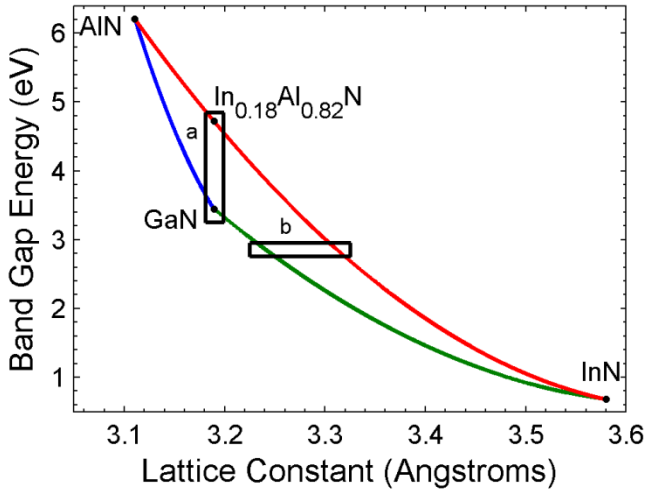

Figure 3.1. The band gap energy versus lattice constant diagram of the III-N material system allows one to visualize band gap and polarization engineering in AlInGaN/GaN heterostructures. Region a) shows AlInGaN films lattice-matched to GaN, with varying $Q_{\pi}(net)$ and E_g, while region b) shows AlInGaN films with E_g = 2.75 eV, and varying $Q_{\pi}(net)$ and $\Delta a/a_0$.

To date, there has been little to no experimental investigation into the interfacial polarization charge at the AlInGaN-GaN interface. Some theoretical work has been carried out in this area[1], but experimental verification of these predictions is still missing. This may be provided by using the HEMT as a diagnostic tool.

3.2 THEORY: CALCULATION OF $Q_{\Pi}(NET)$ AT AN ABRUPT HETEROJUNCTION.

Consider the band diagram of an AlInGaN HEMT, with a thin GaN cap, at equilibrium (Figure 3.2):

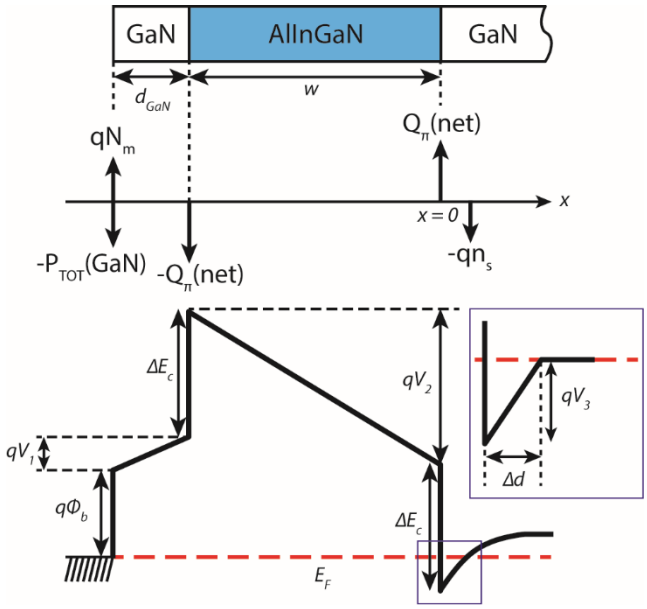

Figure 3.2. Schematic of HEMT layer structure, charge distribution and band diagram. The inset contains the two-dimensional electron gas quantum well drawn under the triangular well approximation, as is common in HEMT analysis[13].

The energy band diagram in Figure 3.2 and all following calculations assume that the background charge carrier concentration, which is a byproduct of MOCVD growth, is sufficiently low such that there is no significant impact on the energy bands (i.e. low ionized donor concentration and insignificant band bending in the AlInGaN). Furthermore, the two-dimensional electron gas (2DEG) is treated as a sheet of charge located at the centroid of the 2DEG wavefunction, a distance Δd from the heterointerface[13,14]. Since the material is at equilibrium, the summation of potential energy changes is equal to zero between the channel and gate:

$$q\phi_b + qV_1 + qV_2 + qV_3 = 0. \tag{3.3}$$

In equation (3.3), qV_1, qV_2, and qV_3 are the conduction band potential energy differences in the structure as derived from the charge distribution in the structure via Gauss' Law. From the charge distribution in Figure 3.2, it is possible to calculate the electric field in each region of

the device structure, beginning at the channel and ending at the surface. Electric fields are calculated by integrating over delta functions, each of which represents a sheet of charge, by an infinitesimal distance σ.

$$\epsilon_{\mathrm{GaN}}\mathcal{E}_3 = \int_{\Delta d+\sigma}^{\Delta d-\sigma} -q \cdot n_{\mathrm{s}}\delta(x-\Delta d)dx = q \cdot n_{\mathrm{s}}, \tag{3.4a}$$

$$\mathcal{E}_3 = \frac{qn_{\mathrm{s}}}{\epsilon_{\mathrm{GaN}}}; \tag{3.4b}$$

$$\epsilon_{\mathrm{AlInGaN}}\mathcal{E}_2 = \epsilon_{\mathrm{GaN}}\mathcal{E}_3 + \int_{0+\sigma}^{0-\sigma} Q_{\pi}(net)\,\delta(x)\,dx, \tag{3.5a}$$

$$\mathcal{E}_2 = -\frac{Q_{\pi}(net)-qn_{\mathrm{s}}}{\epsilon_{\mathrm{AlInGaN}}}; \tag{3.5b}$$

$$\epsilon_{\mathrm{GaN}}\mathcal{E}_1 = \epsilon_{\mathrm{AlInGaN}}\mathcal{E}_2 + \int_{-w+\sigma}^{-w-\sigma} -Q_{\pi}(net)\delta(x+w)\,dx = \epsilon_{\mathrm{GaN}}\mathcal{E}_3 + Q_{\pi}(net) - Q_{\pi}(net), \tag{3.6a}$$

$$\mathcal{E}_1 = \mathcal{E}_3 = \frac{qn_{\mathrm{s}}}{\epsilon_{\mathrm{GaN}}}. \tag{3.6b}$$

Integrating the electric field and multiplying by the electron charge yields the conduction band potential energy differences in the structure.

$$qV_1 = \int_{-(w+d_{\mathrm{GaN}})}^{-w} q \cdot \mathcal{E}_1\,dx = \frac{q^2 n_{\mathrm{s}}}{\epsilon_{\mathrm{GaN}}} \cdot d_{\mathrm{GaN}}, \tag{3.7}$$

$$qV_2 = -\frac{qQ_{\pi}(net)-q^2 n_{\mathrm{s}}}{\epsilon_{\mathrm{AlInGaN}}} \cdot w, \tag{3.8}$$

$$qV_3 = \frac{q^2 n_{\mathrm{s}}}{\epsilon_{\mathrm{GaN}}} \cdot \Delta d. \tag{3.9}$$

In this set of equations, n_{s} represents the channel charge, $Q_{\pi}(net)$ is the net polarization charge at the AlInGaN/GaN interface, d_{GaN} represents the GaN cap thickness, and w is the AlInGaN thickness. Δd was calculated using a 1-D Poisson-Schrödinger solver for a variety of AlGaN/GaN and InAlN/GaN heterojunctions, and was found to vary between 0.95 and 1.10 nm[15]. In light of the minor fluctuations in Δd, it was assumed to be 1 nm for AlInGaN/GaN

heterostructures. The relative dielectric constant of AlInGaN, $\epsilon_{\mathrm{AlInGaN}}$, is approximated to be 9.452 by using Vegard's law.

Combining equation (3.3) with (3.7), (3.8), and (3.9) yields a linear function in *w*:

$$q \cdot n_{\mathrm{s}} D = Q_{\pi}(net) \cdot w - \epsilon_{\mathrm{AlInGaN}} \cdot \phi_{\mathrm{b}} \tag{3.10}$$

where $D = (\epsilon_{\mathrm{AlInGaN}}/\epsilon_{\mathrm{GaN}})(d_{\mathrm{GaN}} + \Delta d) + w$. Thus, one may grow a HEMT series in which the AlInGaN barrier composition is held constant and the thickness is varied. Performing Hall measurements to find the channel charge of each HEMT in the series makes it possible to plot the left-hand side of (3.10) against the AlInGaN thickness, *w*. From there, a linear fit can be used to extract $Q_{\pi}(net)$ from its slope and ϕ_{b}, the surface pinning position of the Fermi level, from its intercept with the ordinate axis.

$Q_{\pi}(net)$ and ϕ_{b} may also be extracted by performing *I-V* and *C-V* measurements on HEMTs and diodes. Unlike Hall measurements, this requires biasing the sample surface with respect to the channel, and thus adds a gate bias to the band diagram in Figure 3.2. In the presence of gate bias, equation (3.3) becomes

$$qV_{\mathrm{g}} = q\phi_{\mathrm{b}} + qV_1 + qV_2 + qV_3. \tag{3.11}$$

Combining equation (3.11) with (3.7), (3.8), and (3.9) yields

$$V_{\mathrm{g}} = \phi_{\mathrm{b}} + \frac{qn_{\mathrm{s}}}{\epsilon_{\mathrm{GaN}}} \cdot d_{\mathrm{GaN}} - \frac{Q_{\pi}(net) - qn_{\mathrm{s}}}{\epsilon_{\mathrm{AlInGaN}}} \cdot w + \frac{qn_{\mathrm{s}}}{\epsilon_{\mathrm{GaN}}} \cdot \Delta d. \tag{3.12}$$

If n_{s} is set to zero, V_{g} becomes the pinch-off voltage, V_{p}. Rearranging terms allows the expression for the pinch-off voltage to be written as a function of the AlInGaN barrier thickness:

$$V_{\mathrm{p}}(w) = \phi_{\mathrm{b}} - w\left(\frac{Q_{\pi}(net)}{\epsilon_{\mathrm{AlInGaN}}}\right). \tag{3.13}$$

If one first measures the pinch-off voltages for a series of HEMTs with varying AlInGaN barrier thicknesses, then a linear fit to the V_{p} *vs w* data can be used to extract both ϕ_{b} and

Q_π*(net).* Since these HEMTs are GaN-capped, it is expected that the ϕ_b extracted from the intercept of V_p *vs w* corresponds to the pinning level of the Fermi energy at the interface between GaN and the gate metal. Calculating Q_π*(net)* from the slope of V_p *vs w* yields the net polarization charge at the AlInGaN/GaN interface.

3.3 EXPERIMENTAL

In order to proceed with the experiment, it was first necessary to determine if the background carrier concentration was low enough for the proposed analysis to be valid. To do so, a thick sample was grown under identical conditions as the series used in this experiment and sent out to Evans Analytical Group for Secondary Ion Mass Spectroscopy (SIMS). The background oxygen concentration was measured to be about $3 \cdot 10^{17}$ cm^{-3}. This is the sample from Chapter 2 used for SIMS analysis – growth conditions for all samples here are identical, aside from crystal composition. Thus we can assume that the background carrier concentration may be slightly higher for these high-Y_{AlN} films. This value was inexact due to differences between the GaN and AlInGaN etch rates in SIMS, but an oxygen background in the mid-10^{17}s cm^{-3} was low enough to assume that the bands were linear in the thin HEMT barriers. The final test of the validity of this assumption would be the quality of the linear fit to the V_p *vs w* data. Significant deviation from linearity would indicate an appreciable amount of ionized donors in the HEMT barrier.

3.3.1 Material growth and device fabrication

The GaN/AlInGaN/GaN HEMTs used in this study were grown by metalorganic chemical vapor deposition (MOCVD). The AlInGaN layers, as well as the thin GaN cap, were

grown at 70 torr and 804 C in nitrogen carrier gas atop a semi-insulating GaN template. The GaN cap was used to ensure a reproducible Schottky barrier height for all samples. The composition of the AlInGaN was calibrated by SIMS and kept constant at $Al_{0.54}In_{0.12}Ga_{0.34}N$. This composition was chosen for three reasons: first, its band gap is larger than GaN, about 4.18 eV[16]; second, it is in new growth territory, since this composition is far from any of the ternary alloys; third, from previous experience it is known that this composition may be grown with good surface morphology and low impurity concentration. XRD scans of each sample showed very little fluctuation in AlInGaN composition. The fact that this sample is in new growth territory is excellent for testing polarization constants and bowing parameters. Since there is an appreciable fraction of AlN, InN, and GaN simultaneously, any deviation from the established constants and bowing parameters from the ternaries should be most apparent in a sample like this.

For this growth series, the GaN cap thickness (d_{GaN}) was held constant at 2 nm, while the AlInGaN thickness (w) was varied between 7.9 and 18.5 nm. Thicknesses were calibrated via XRD with a reference sample and re-verified after growth. In order to mitigate the detrimental effects of surface kinetics during low temperature growth of high-Y_{AlN} films, the AlInGaN growth rate was chosen to be about 0.65 nm/min[17]. A standard optical gate process was used to fabricate the HEMTs, in which the source and drain Ohmic contacts were Ti/Al/Ni/Au and annealed at 820 °C for 30 s[18]. The gate metal stack was Ni/Au, and a BCl_3/Cl_2 etch provided device isolation. Hall dies and Schottky diodes were fabricated simultaneously; the gate lithography and metallization were omitted from the Hall dies.

3.3.2 Electrical measurements

Hall measurements were performed on a Lakeshore Hall Measurement system to find n_s values for each HEMT sample. n_s was measured at three magnetic field intensities: 6 kilo-Gauss (kG), 4 kG, and 2kG. The measurement results were identical at each magnitude of the magnetic field, which bolstered the validity of the measurement. Afterward, *I-V* and *C-V* measurements were performed to find the pinch-off voltage, V_p, for the HEMT samples. For the *I-V* measurements, the drain current (I_d) was measured as a function of the gate bias (V_g) on an Agilent 4155b Semiconductor Parameter Analyzer, with the drain-source bias fixed at 6V. The I_d-V_g curves had a linear region of constant transconductance (g_m), which yielded to gate leakage current with decreasing (more negative) gate bias (Figure 3.3). The pinch-off voltage was extracted by performing a linear fit to the data at the point of maximum g_m, and then calculating the intercept of that line with the abscissa. The fit was extended to further data points past the point of maximum g_m while the R^2 value of the fit remained above 0.9995. All data points deviating from a straight line were excluded from the fit (red data points in Figure 3.3) because the current in these regions was influenced by factors other than the amount of charge present in the channel underneath the gate.

The large drain-source bias was to ensure that the linear region of the I_d-V_g curve was as large as possible, and that the channel was entirely pinched off by the gate. Near 0V the onset of transconductance compression was apparent, while gate leakage was the main contributor to drain current beyond -3.5V. These measurements were repeated for each die on the wafer, and an average pinch-off voltage was calculated for each sample.

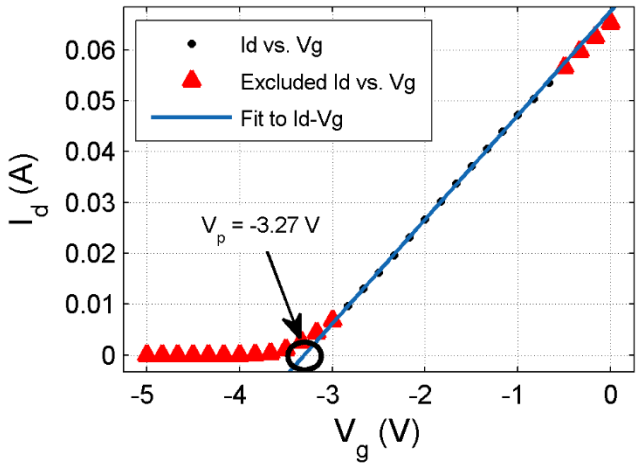

Figure 3.3. I_d *vs.* V_g for an AlInGaN HEMT with an 18.4 nm barrier. At larger reverse bias, gate leakage dominates the measured current, while near 0V the onset of transconductance compression becomes apparent.

C-V measurements were performed on Schottky diodes with a 100-micron radius using an Agilent 4294 Impedance Analyzer with ground-signal-ground (GSG) probes. The *C-V* curves showed very abrupt charge modulation, as is characteristic of 2DEG depletion, and the diodes on each sample were biased from 0V until the capacitance dropped to a minimum and stabilized. This varied between -1.5 and -5V, depending on the thickness of the AlInGaN layer. The *C-V* curves were then numerically integrated to obtain n_s vs. V_g (Figure 3.4), which has a shape similar to that of the I_d-V_g curve, and the analysis was the same: perform a linear fit and extrapolate down to the point where $n_s = 0$ (the condition for pinch-off of the channel). Data points that deviated from linear behavior were excluded from the fit, and an average pinch-off voltage was calculated for each sample.

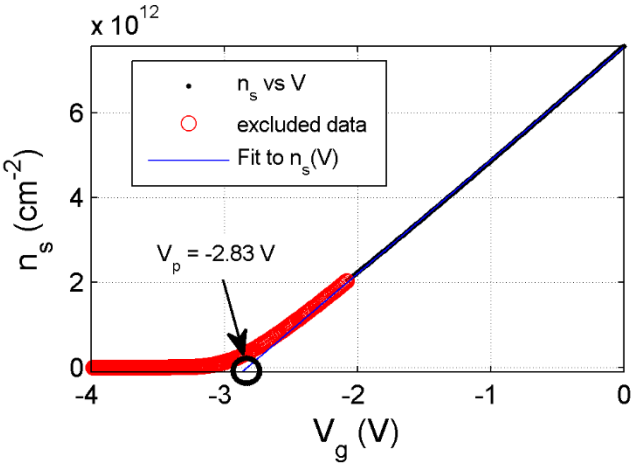

Figure 3.4. n_s vs. V_g for an AlInGaN HEMT with an 18.4 nm barrier. Points that deviate from linearity beyond -3V have been excluded.

3.4 RESULTS AND DISCUSSION

3.4.1 Electrical characterization results

The result of the pinch-off voltage calculations and Hall measurements can be seen in (Figure 3.5) with a linear trend line superimposed over them. The linear fit has very high fidelity to the data, supporting the assumption that any band bending in the AlInGaN HEMT barrier was insignificant. This also validated the SIMS measurements that showed low background oxygen concentration in the AlInGaN. After obtaining the fit parameters, equation (3.10) was used to extract $Q_\pi(net)$ and ϕ_b from Figure 3.5a, while equation (3.13) was used to extract $Q_\pi(net)$ and ϕ_b from Figures 3.5b and 3.5c. The results are summarized in TABLE 3.1 and organized by the extraction method. One should notice the excellent agreement between the $Q_\pi(net)$ measurements: there is only a 6.5% variation in between all of the measurement techniques. Furthermore, the measured $Q_\pi(net)$ agrees with the theoretical prediction of $2.07 \cdot 10^{-6}$ C/cm^2 within about 3.5%[1].

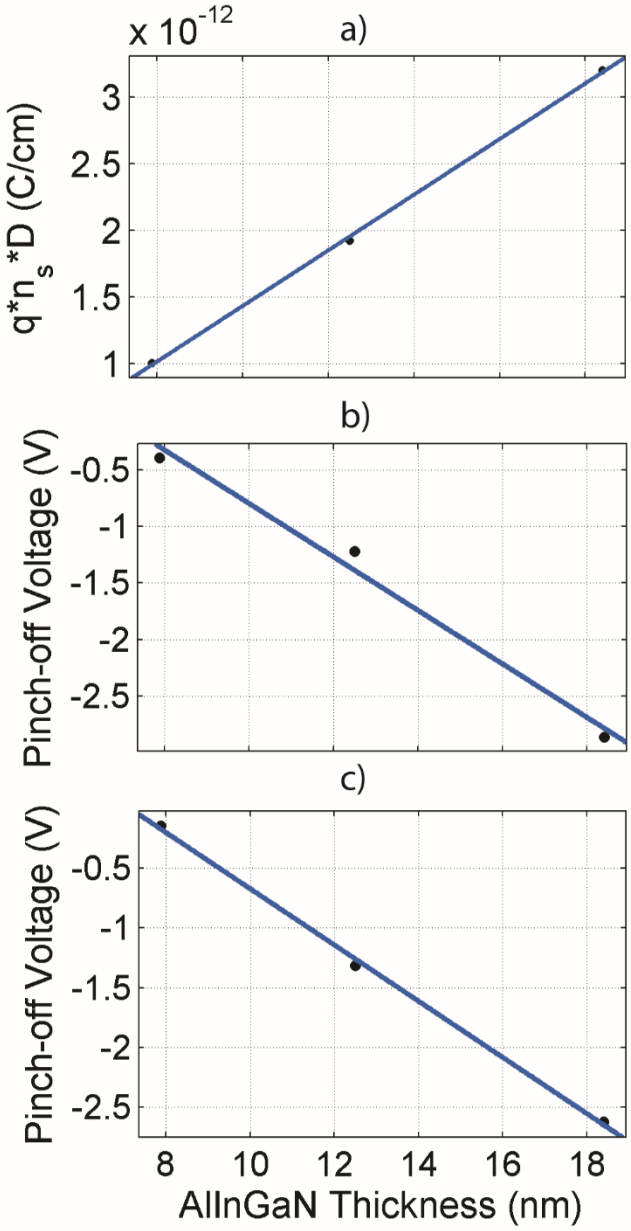

Figure 3.5. (a) $q \cdot n_s \cdot D$ vs AlInGaN thickness, (b) V_p vs. AlInGaN thickness from I_d-V_g measurements, and (c) V_p vs. AlInGaN thickness from *C*-*V* measurements. The high fidelity of the fit to the data indicates low background carrier density and consistency between samples.

One will also notice from TABLE 3.1 that the Schottky barrier height from the I_d-V_g and *C*-*V* measurements were much higher than the expected barrier height between GaN and nickel (~0.84 eV), while the surface pinning level as measured by Hall was reasonable[16]. This

discrepancy was attributed to the processing steps used prior to gate metallization: after lithography, a 30-second O_2 descum was performed, followed by a 1-minute dip in buffered hydrofluoric acid (HF) immediately prior to metallization. It is believed that the oxidative properties and damaging energetic particles of the O_2 plasma combined with the HF removed the thin GaN cap layer (2 nm) at the surface, leaving in its place a defective oxy-nitride surface.

TABLE 3.1. Summary of measured $Q_{\pi}(net)$ and ϕ_b values from the three techniques employed in this study. Also included are the values obtained from modified runs of the process on additional pieces of the wafer.

Extraction Method	$Q_{\pi}(net)$ **(10^{-6} C/cm^2)**	ϕ_b **(eV)**
Hall	2.099 ± 0.054	0.774 ± 0.024
I_d-V_g	1.978 ± 0.036	1.567 ± 0.001
C-*V*	1.968 ± 0.133	1.681 ± 0.086
I_d-V_g + UV ozone	2.033 ± 0.016	1.784 ± 0.077
C-*V* w/o descum	2.064 ± 0.086	1.418 ± 0.061
C-*V* w/o descum, w/o HF dip	1.904 ± 0.054	1.144 ± 0.156

3.4.2 Analyzing effects of the interfacial oxide

In order to probe the effect of the surface treatment on the Schottky barrier height, several splits of the process were performed on additional pieces of the wafers. Since the change in ϕ_b was attributed to the gate processing, the splits were all designed to modify or eliminate either the descum step or pre-metallization acid dip. The splits were as follow: first, the descum method was modified, in which the O_2 plasma descum was substituted for a 20-minute UV Ozone descum; second, the descum was eliminated entirely; third, both the descum

and HF dip were eliminated. As can be seen from TABLE 3.1, none of the processing splits had a large influence on the magnitude of $Q_{\pi}(net)$, which reinforces the validity of the measurement result.

However, the results in TABLE 3.1 did reveal that the metal-semiconductor barrier height varied significantly with changes in the gate fabrication process. The UV Ozone descum seemed to have a further detrimental effect on the Schottky barrier height, and yielded a deeper pinning position with a ϕ_b of 1.784 eV. Eliminating the descum reduced the barrier height to 1.417 eV, and indicated that the oxidative properties of the descum, combined with the acid dip, significantly altered the surface away from what was intended to be a GaN cap. Eliminating both the descum and acid dip from the process yielded a barrier height of 1.144 eV, which was closer to the expected value of 0.84 eV.

These non-ideal barrier heights indicated that the GaN cap used for these HEMTs was of comparable thickness to the amount of material that was removed prior to gate metallization. If the cap layer was too thin, then performing a descum and acid dip prior to metallization can result in the oxidation and removal of nearly the entire cap. Subsequent exposure to the atmosphere can then either oxidize whatever remains of the GaN cap or, if the GaN cap is completely missing in some areas, oxidize a surface layer of exposed AlInGaN. Not only would this yield a highly defective oxide at the surface, but it would also change the layer structure and band diagram of the device. If the cap layer of the HEMT were considered to be a defective oxide instead of GaN, then that may provide an explanation as to why the extracted barrier height was too large. Furthermore, if it were assumed that the cap layer was 1 nm of $Ga_{1-x-y}N_xO_y$, one may refer to the band diagram in Figure 3.6 and the formalism previously introduced to derive the following:

$$V_g = \phi_b + \frac{qn_s + Q_{oxide} - Q_\pi(net)}{\epsilon_{oxide}} \cdot d_{oxide} - \Delta E_{c,oxide} - \frac{Q_\pi(net) - qn_s}{\epsilon_{AlInGaN}} \cdot w - \Delta E_c + \frac{qn_s}{\epsilon_{GaN}} \cdot \Delta d, \quad (3.14)$$

$$V_p(w) = \left(\phi_b - \Delta E_{c,oxide} - \Delta E_c + \left(\frac{Q_{oxide} - Q_\pi(net)}{\epsilon_{oxide}}\right) \cdot d_{oxide}\right) - \left[\frac{Q_\pi(net)}{\epsilon_{AlInGaN}}\right] \cdot w, \quad (3.15)$$

where Q_{oxide} is the fixed charge at the oxide/AlInGaN interface, $\Delta E_{c,oxide}$ is the conduction band discontinuity between the oxidized cap layer and the AlInGaN, and ϵ_{oxide} is the dielectric constant of the cap layer. The magnitude and sign of Q_{oxide} is unknown; the representation in Figure 3.6 is for illustrative purposes.

3.4.3 Q_π(net) *measurement tolerant to deviations in layer structure*

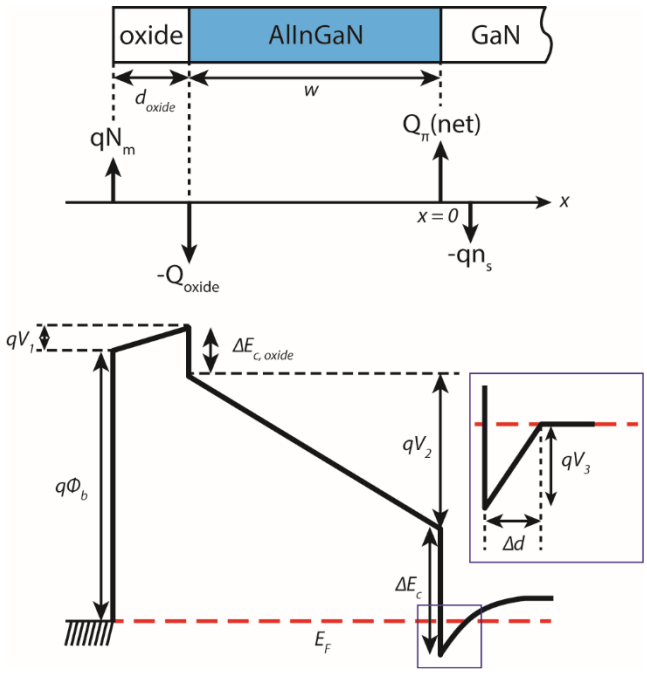

Figure 3.6. Schematic diagram, charge distribution, and band diagram of AlInGaN/GaN HEMT under the assumption that the AlInGaN was capped with an oxidized layer instead of GaN. Please note that Q_{oxide} refers to fixed charge and $\Delta E_{c,oxide}$ is the conduction band offset at the AlInGaN/oxide interface. No assumptions are made about the magnitude or sign of Q_{oxide} or $\Delta E_{c,oxide}$; this diagram is for illustrative purposes.

Equation (3.15) shows that without GaN at the surface, the intercept of V_p *vs* w would depend on the conduction band offsets in the device structure, the voltage drop in the oxide

layer from the net charge at the oxide/AlInGaN interface, and the Schottky barrier height to the oxidized cap layer. It is also apparent from equation (3.15) that the oxide layer would have no effect on the slope of V_p vs. w as long as the AlInGaN thickness, w, is unaffected by the surface oxidation. Consequently, the entire second term of equation (3.15) is identical to the second term in equation (3.13). Since the calculation of $Q_\pi(net)$ at the AlInGaN/GaN interface only depends on the slope of V_p *vs* w, the calculations using equation (3.13) are unaffected by changes in the band diagram due to the oxidation of the GaN cap layer. Therefore, the barrier height extracted in these measurements may not reflect the true Schottky barrier height of Ni to GaN, but the $Q_\pi(net)$ measurement is trustworthy and tolerant to process deviations in device fabrication.

3.5 CONCLUSIONS: EVOLVING TOWARD PREDICTIVE DEVICE DESIGN

The HEMT structure has proven to be a very useful tool for examining the electrical properties of AlInGaN/GaN heterojunctions. It was apparent that the Schottky barrier height to the cap layer on the AlInGaN barrier was very sensitive to the processing steps prior to gate metal deposition. The barrier height to the gate metal varied with the method used for post-lithography descums, and each descum method yielded a ϕ_b far from the ideal value for a Ni-GaN junction. More care must be taken in the future to prevent the introduction of oxide and/or defect states under the gate. It is advisable to use thicker GaN cap layers for similar experiments, since processing the HEMTs without any descum or etch step still yielded a Schottky barrier height that was larger than commonly reported in literature.

Furthermore, this study has revealed the net polarization at the heterointerface between $Al_{0.54}In_{0.12}Ga_{0.34}N$ and GaN. The average value of $Q_\pi(net)$ between *I-V*, *C-V* and Hall

measurement methods was $2.015 \cdot 10^{-6}$ C/cm^2 with a standard deviation of $1.31 \cdot 10^{-7}$ C/cm^2. Measured $Q_{\pi}(net)$ values agreed within 3.5% of theoretical calculations and were extremely consistent between a variety of measurement techniques, with only 6.5% variation between measurement techniques. Additional processing variations showed that this measurement and data analysis technique for extracting $Q_{\pi}(net)$ was consistent, and tolerant to changes in layer structure or errors in device fabrication.

This result is a significant step forward for design and development using quaternary alloys. Engineers are now in a position to utilize polarization constants and bowing parameters that have been experimentally validated for AlInGaN systems. If this knowledge is paired with the correct software suite, then it is possible to move beyond the semi-empirical phase of fabrication-measurement-characterization to a regime where simulations can accurately predict the electrostatic nature of heterojunction devices. Furthermore, the current knowledge base can be expanded upon to develop simulation tools that accurately predict transport behavior in addition to electrostatics.

A commercial software suite, nextnano++[19], was found to provide all the functionality necessary to simulate the band structure of AlInGaN heterojunction epilayer stacks. It offered the ability to modify a local database file to fine-tune the material constants it calls upon to the user's demands, and has built-in functionality to simulate the structure in any crystallographic direction of desire, apply bias to a structure and calculate quasi-Fermi levels, and more. In order to evaluate the accuracy of this software, one of the structures from the HEMT barrier thickness series from section 3.3.1, with AlInGaN thickness of 18.4 nm, was constructed in the software and simulated. Figure 3.7 shows the result, which displays both the band diagram and the charge density profile. This charge density profile was integrated along the direction

of simulation to give a simulated 2DEG density, n_s(sim). This simulated value was found to be $9.33 \cdot 10^{12}$ cm^{-2}, and was compared to the experimentally measured (via Hall measurements) 2DEG density, n_s(Hall) = $9.03 \cdot 10^{12}$ cm^{-2}. Simulation and experiment also agreed well for the other sample thicknesses from this series, which indicated that the 2DEG density varied as expected with HEMT barrier thickness.

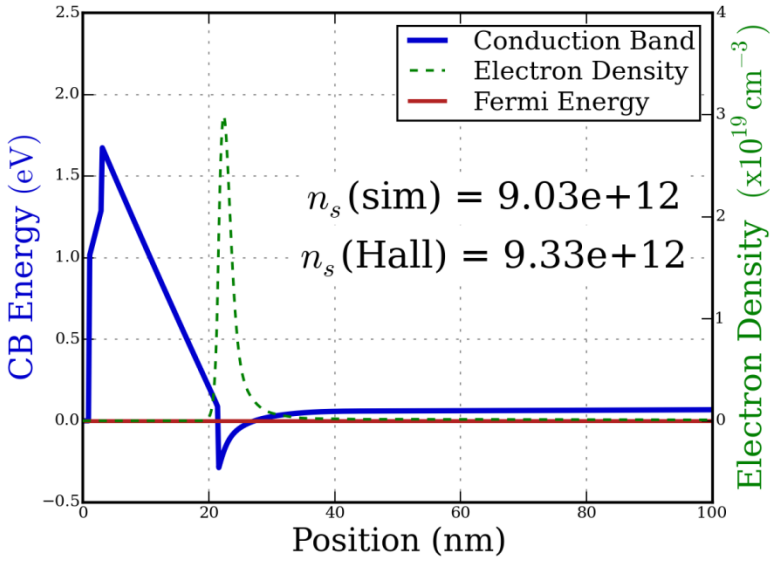

Figure 3.7 shows the band diagram and charge density profile of a GaN/AlInGaN/GaN HEMT with 2 nm GaN cap and 18.4 nm AlInGaN barrier. Note the agreement in charge density between simulation and experiment.

The accuracy of this result encourages continued use of this software, but caution must be exercised! Replicating experimental results is a good first step, but it also provides confirmation bias to the user. The next step to qualify the software must be simulation of a new, but simple, device structure (perhaps a HEMT grown with a different AlInGaN composition) and once again compare experimental to simulated results. If nextnano++ proves itself under predictive conditions, then it can be considered a widely viable simulation tool throughout the AlInGaN system. It would be wise to slowly build up the complexity of simulations and device fabrication after that, while re-verifying as complexity increases.

3.6 POLARIZATION ENGINEERING WITH AlInGaN

Polarization engineering with AlInGaN films offers certain advantages when comparing to creating similar technologies in the AlGaN or InGaN systems. First of all, it is known that with the choice of the correct composition of AlGaN, one can engineer a heterojunction with either positive or negative resolved net polarization charge ($+Q_{\pi}(net)$ or $-Q_{\pi}(net)$). Second, it is possible to incorporate the demonstrated growth capabilities of thick films, varying strain states, and lattice-matched heterojunctions with a variety of compositionally graded layers and abrupt heterojunctions. Thus, in a single material system and single set of growth conditions, it is possible to achieve high-conductivity charge slabs, current blocking layers, or even fine-tuned electric fields in quantum wells (or barriers).

Graded layers were first investigated due to their intriguing potential from both a technological and scientific perspective[20]. There are two senses of graded layers. The first to be investigated was the direct grade, in which the grade begins with GaN and the concentration of the ternary and quaternary elements (Al and In) are gradually increased on the group III lattice site (Figure 3.8) to terminate in an alloy with a larger band gap. Junctions similar to these have been previously investigated for use in the polFET, which is a MESFET structure that utilized polarization in place of typical impurity-based doping in order to form the channel[21]. In addition to the polFET, structures such as these have applications in high-conductivity n-type layers (which can be free of doping), or in test structures to investigate alloy scattering in the nitrides.

It should be noted that Figure 3.8a shows a polFET structure, but from the charge profile, it is also apparent that a very efficient Ohmic contact could be created if the heterojunction between GaN and the wide band gap material were eliminated near the surface.

Furthermore, it is possible to exact excellent compositional control over the grade, as seen in Figure 3.8b. This structure was engineered to be lattice-matched throughout the length of the grade. Although there are some deviations from lattice matched (black curve vs. magenta line), it should be possible to get a perfectly lattice-matched film with some minor flow rate and temperature recalibrations.

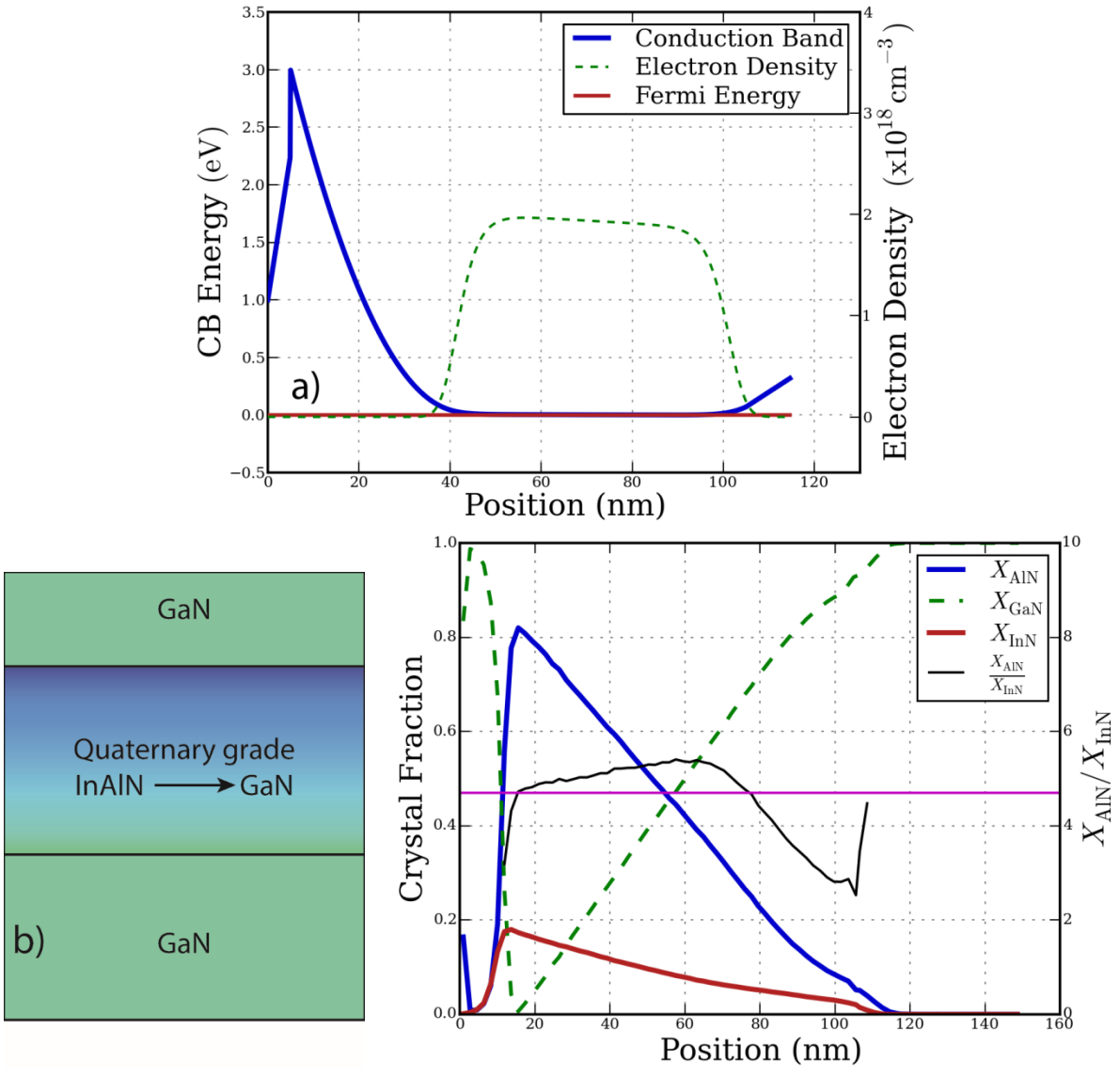

Figure 3.8 a) shows the band diagram and charge profile for a direct grade of increasing band gap in the AlInGaN system. The heterojunction at the surface creates a gating effect for charge control of the 3-

dimensional charge slab. b) Shows the layer structure, compositional measurement along the grade (by SIMS), and deviations from the lattice-matching condition (difference between black curve and magenta line).

The second style of grade to be investigated was the retrograde, which amounts to grading from wide to narrower band gap. This can be a grade from GaN to a narrower band gap material such as InGaN, or an indium-rich AlInGaN, but for the purposes of current blocking layers and hot electron injectors, structures as in Figure 3.9 were investigated. These utilized an abrupt GaN-InAlN heterojunction, followed by a grade back to GaN. Switching from the graded to retrograded structure required a very trivial change in the MOCVD recipe. Figure 3.9b shows good compositional control, but development must be continued to improve agreement with the film composition ratio (black curve) and the lattice-matching condition (magenta line).

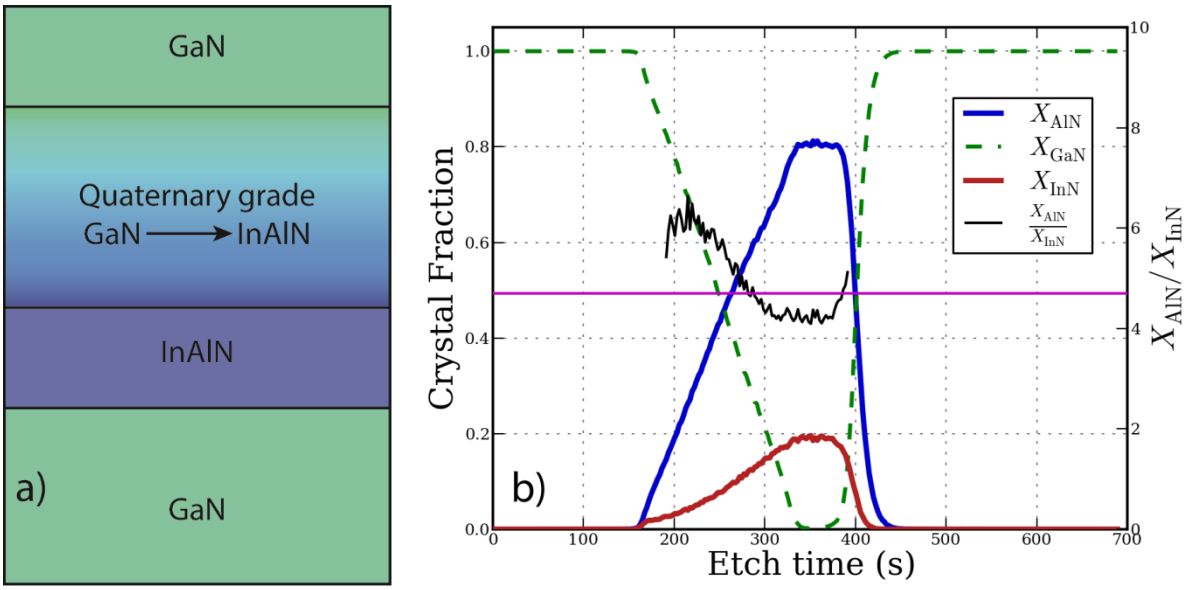

Figure 3.9 shows the layer schematic (a) and the compositional profile (b) of a retrograded structure.

A compositional retrograde such as this has potential applications in two possible ways. First, as shown in Figure 3.10a, it can be used as a current blocking layer, or p-type layer, as the negative fixed polarization charge ($-Q_\pi$) introduced by this technique will pull the valence

band up to the Fermi level. Second, it was originally thought that the triangular potential in Figure 3.10b could be achieved by counter-doping the graded layer in order to offset the $-Q_\pi$ with positive N_d^+ from silicon donors.

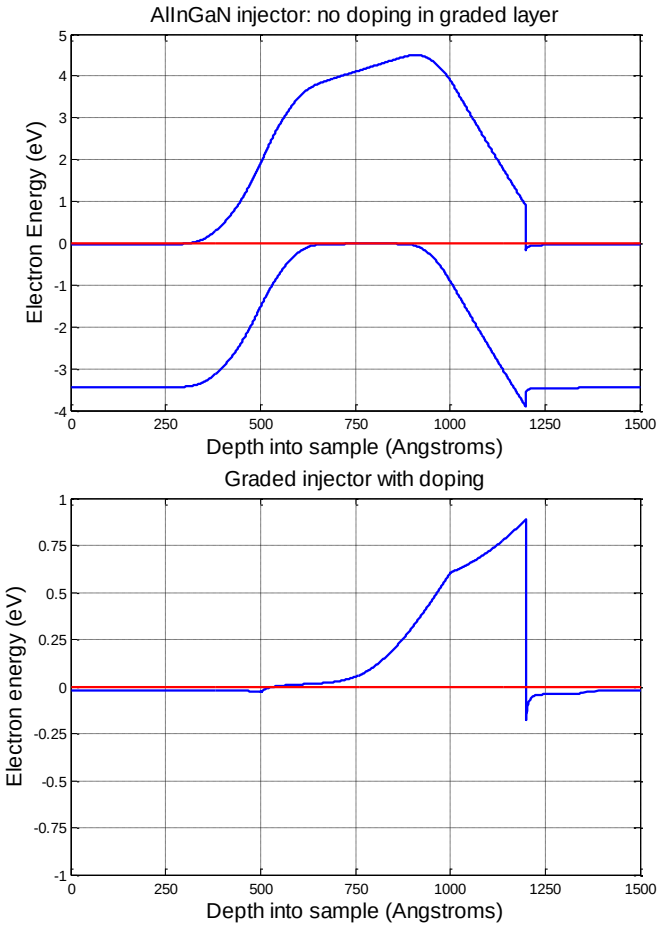

Figure 3.10 shows the different band configurations for a retrograded structure. 3.10a) shows the viability of a graded structure for p-type and current blocking layers. 3.10b) shows the initial strategy of achieving hot electron injectors by counter-doping graded layers. This strategy does not work.

However, this application was based upon poorly executed simulations that neglected to take quantum mechanical effects into account. The true effect of counter doping on the energy bands in a retrograde is shown in Figure 3.11. This shows fully quantum mechanical self-consistent Poisson-Schrodinger simulations in nextnano++ which display very clear

behavior: the bands are resistant to counter-doping until the -Q_π from the polarization is perfectly counter-balanced by the ionized silicon dopants (this occurs around N_d = 1e18 cm^{-3}). Then if the doping exceeds –Q_π, even slightly, the counter-doping pulls the conduction band down toward the Fermi level everywhere and most of the barrier is eliminated (as in the dark red curve in Figure 3.11).

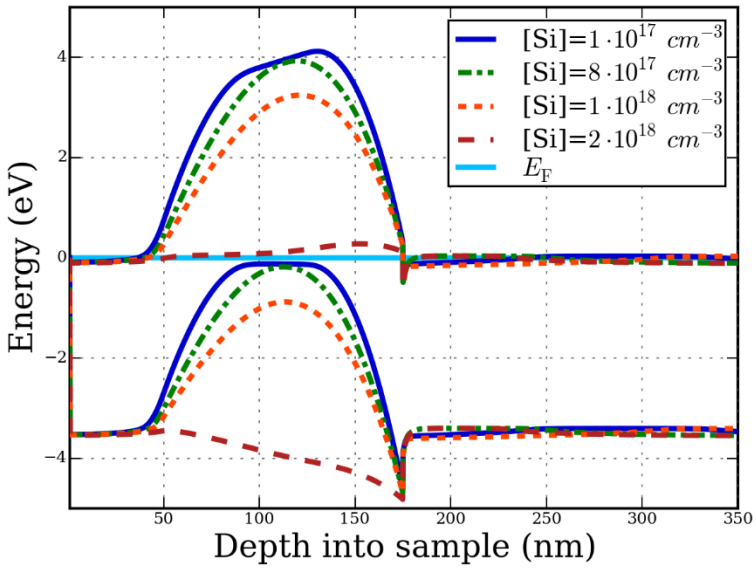

Figure 3.11 shows the reality of trying to create a hot electron injector by this method. The bands create a potential energy barrier until –Q_π is perfectly balanced by N_d^+. Any additional doping eliminates the barrier.

It is also important to note that acceptable surface morphologies are obtainable with graded layers, some as thick as 150 nm, as seen in Figure 3.12. "Acceptable" is in the context of what has been proven to have good electrical properties in the AlInGaN system. The devices with similar morphologies present in Figure 2.24 all yielded Schottky diodes with excellent reverse bias characteristics and ideality factors close to unity at room temperature. Refer to Chapter 4 for more details, and see Figure 4.1 for general *J-V* properties of these films.

Though the MOCVD composition control has been demonstrated for both graded and abrupt heterojunctions, polarization engineering with AlInGaN is still in its infancy. The

impact of process parameters on the surface morphology of graded layers must be investigated in detail. More work is necessary to fine-tune the growth processes for precision applications, and electrical characterization of these films has yet to be performed. Please refer to Chapter 5 for a more extensive discussion of proposed polarization engineering structures with associated band diagrams.

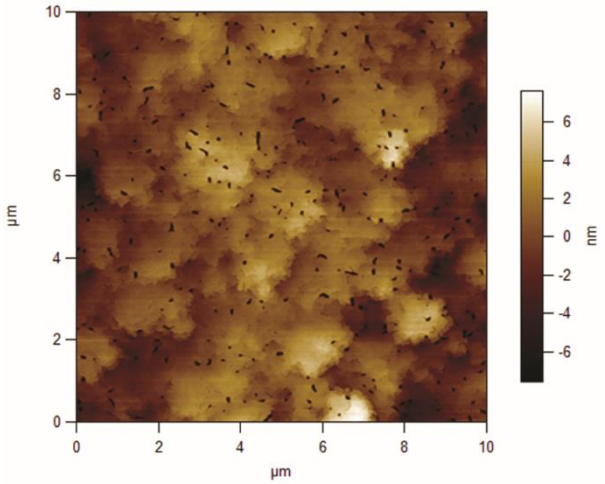

Figure 3.12 shows the surface morphology of a retrograded structure. RMS roughness exceeds that of a constant-composition sample of comparable thickness by 50%, but pit size and density is comparable.

3.7 REFERENCES

[1] D. Jena, J. Simon, A. Wang, Y. Cao, K. Goodman, J. Verma, S. Ganguly, G. Li, K. Karda, V. Protasenko, C. Lian, T. Kosel, P. Fay, and H. Xing, Phys. Status Solidi Appl. Mater. Sci. **208**, 1511 (2011).

[2] B. Reuters, A. Wille, B. Holländer, E. Sakalauskas, N. Ketteniss, C. Mauder, R. Goldhahn, M. Heuken, H. Kalisch, and A. Vescan, J. Electron. Mater. **41**, 905 (2012).

[3] H. Hahn, B. Reuters, A. Wille, N. Ketteniss, F. Benkhelifa, O. Ambacher, H. Kalisch, and A. Vescan, Semicond. Sci. Technol. **27**, 055004 (2012).

[4] F. Bernardini and V. Fiorentini, Phys. Rev. B **64**, 085207 (2001).

[5] O. Ambacher, M. Eickhoff, A. Link, M. Hermann, M. Stutzmann, F. Bernardini, V. Fiorentini, Y. Smorchkova, J. Speck, U. Mishra, W. Schaff, V. Tilak, and L.F. Eastman, Phys. Status Solidi **1907**, 1878 (2003).

[6] M.A. Khan, J.W. Yang, G. Simin, R. Gaska, M.S. Shur, and A.D. Bykhovski, Appl. Phys. Lett. **75**, 2806 (1999).

[7] U.K. Mishra, P. Parikh, and Y. Wu, Power **90**, (2002).

[8] B. Reuters, A. Wille, N. Ketteniss, H. Hahn, B. Holländer, M. Heuken, H. Kalisch, and A. Vescan, J. Electron. Mater. **42**, 826 (2013).

[9] Y.A. Chang, Y.R. Lin, J.Y. Chang, T.H. Wang, and Y.K. Kuo, IEEE J. Quantum Electron. **49**, 553 (2013).

[10] N. Ketteniss, L.R. Khoshroo, M. Eickelkamp, M. Heuken, H. Kalisch, R.H. Jansen, and A. Vescan, Semicond. Sci. Technol. **25**, 075013 (2010).

[11] S.-H. Park and D. Ahn, IEEE J. Sel. Top. Quantum Electron. **19**, 1901308 (2013).

[12] M.F. Schubert, J. Xu, J.K. Kim, E.F. Schubert, M.H. Kim, S. Yoon, S.M. Lee, C. Sone, T. Sakong, and Y. Park, Appl. Phys. Lett. **93**, 2006 (2008).

[13] U.K. Mishra and J. Singh, *Semiconductor Device Physics and Design* (Springer, Dordrecht, The Netherlands, 2008).

[14] H. Kroemer and W.-Y. Chien, Solid. State. Electron. **24**, 655 (1981).

[15] M. Grundmann, *BandEng 1-D Poisson-Schrödinger Solver* (2004).

[16] E. Sakalauskas, B. Reuters, L.R. Khoshroo, H. Kalisch, M. Heuken, A. Vescan, M. Rppischer, C. Cobet, G. Gobsch, and R. Goldhahn, J. Appl. Phys. **110**, 1 (2011).

[17] R.B. Chung, F. Wu, R. Shivaraman, S. Keller, S.P. DenBaars, J.S. Speck, and S. Nakamura,

J. Cryst. Growth **324**, 163 (2011).

[18] C.-H. Chen, S. Keller, G. Parish, R. Vetury, P. Kozodoy, E.L. Hu, S.P. Denbaars, U.K. Mishra, and Y. Wu, Appl. Phys. Lett. **73**, 3147 (1998).

[19] S. Birner, *Nextnano - Semiconductor Software Solutions* (http://nextnano.com/, 2015).

[20] J. Simon, V. Protasenko, C. Lian, H. Xing, and D. Jena, Science **327**, 60 (2010).

[21] S. Rajan, H. Xing, S. DenBaars, U.K. Mishra, and D. Jena, Appl. Phys. Lett. **84**, 1591 (2004).

Chapter 4

CURRENT-VOLTAGE ANALYSIS OF $Al_xIn_yGa_{(1-x-y)}N$ SCHOTTKY DIODES

4.1 MOTIVATION: METAL-SEMICONDUCTOR JUNCTIONS

The net interfacial polarization charge at AlInGaN heterointerfaces is one of many material constants that shape the band diagram and electrostatics of a device, and thereby influence device current transport. It is possible to add to the quantitative understanding of band diagrams of AlInGaN-based devices by investigating the barriers that form at metal-semiconductor junctions (Schottky contacts). The Schottky barrier height (SBH) of a metal-semiconductor junction is a critical design parameter for a HEMT, as it will influence the 2DEG density and pinch-off voltage of the device[1,2]. It is also relevant for constructing a band diagram for PolFETs, Schottky diodes, and other vertical devices like the hot electron transistor (HET)[3,4]. In the case of the HET, it may be necessary to find a metal that can form an Ohmic contact to a quaternary layer. To add to the quaternary design toolbox, it is important to characterize the Schottky nature of AlInGaN contacts to a wide range of metals, and create an empirically defined table of these values for a range of AlInGaN compositions.

The Schottky diode is also invaluable for characterizing vertical charge carrier transport in AlInGaN. The Schottky diode allows for observation and characterization of non-idealities that may be observed in transport, and compare them to known issues in ternary alloys. It is then possible to discover if AlInGaN shares conduction mechanisms with InAlN, and assess

how defects and impurities will affect conduction in their own respective ways. With Schottky diodes, it is possible to determine the main conduction mechanism (i.e. thermionic emission, tunneling, shunt pathways, etc.), and apply a mathematical model to describe that transport. The AlInGaN Schottky diodes presented here have low reverse-bias leakage and function via barrier-limited transport. Subsequent analysis focused on provide an describing this barrier as a function of composition and material band gap, assessing the role of Fermi level pinning in barrier height formation, and relating transport properties to attributes that are inherent to the material from growth or induced by processing.

AlInGaN diode properties are insufficiently characterized in relation to AlGaN, InGaN, and InAlN. It is important to keep in mind that the ultimate goal is to reach the point where meaningful device design and simulation can be done in the AlInGaN system. This requires a sufficient understanding of electrostatics, barrier heights, and current transport in AlInGaN-based devices. All of these can be furthered along by analyzing Schottky diode behavior, which is the focus of this chapter. Of particular interest is the Ni-AlInGaN interface, the junction of interest in this chapter, due to the extensive use of nickel as Schottky contacts in III-N diodes and gate electrodes in HEMTs. The AlInGaN system has a large parameter space, and to-date the SBH is reported for only few compositions[5,6]. In the interest of characterizing it more thoroughly, Schottky diodes of varying InN and AlN fractions, X_{InN} and X_{AlN}, were examined.

4.2 CURRENT-VOLTAGE ANALYSIS OF IDEAL SCHOTTKY DIODES

First and foremost, AlInGaN and GaN Schottky diode behavior from experimental results must be compared with the ideal case. In Schottky diodes, the SBH, (ϕ_{b}), and the

Richardson constant (A^*) are the material properties which govern current transport by thermionic emission (TE). It is possible to extract this information from analyzing current density vs voltage curves as a function of temperature (*J-V-T* measurements). If one considers the ideal diode equation,

$$J = J_S\left[\exp\left(\frac{qV}{nk_bT}\right) - 1\right], \tag{4.1}$$

and focuses on the low-voltage forward-bias regime of the device, it is possible to extract the saturation current of the device, J_S, from

$$\ln(J) = \ln(J_s) + \frac{qV}{nk_bT}, \tag{4.2}$$

while neglecting the series resistance of the device, as well as the last term in equation (4.1). Therefore, by measuring *J vs V*, it is possible to calculate J_S at each measurement temperature from equation (4.2) by evaluating a linear regression to the data, as in Figure 4.1.

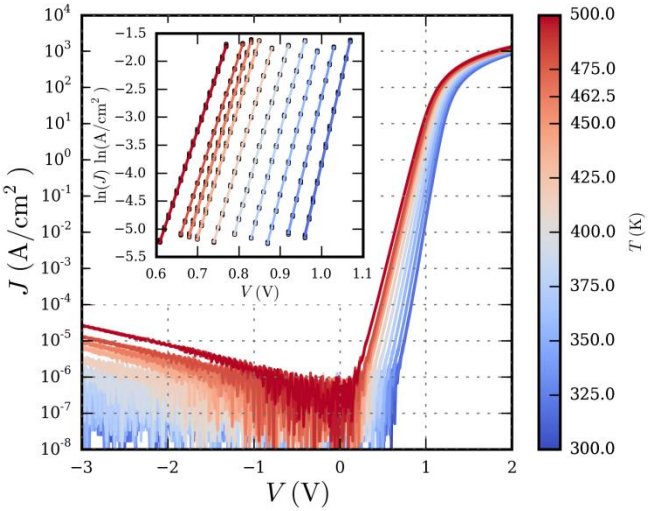

Figure 4.1. *J -V-T* measurements for AlInGaN alloys show low leakage current in reverse bias, and exponential current growth in forward bias. The inset shows the forward-bias regime of the curves where a linear fit to the data is applied. Multiple curves were taken at each temperature to calculate an average J_S for each sample.

Compiling J_S as a function of measurement temperature allows one to construct a Richardson plot from

$$\ln\left(\frac{J_S}{T^2}\right) = \ln(A^*) - \frac{q\phi_b}{k_b T}, \tag{4.3}$$

which is an Arrhenius-style graph where the "activation energy" is the barrier that limits transport of charge carriers across the metal-semiconductor junction interface[7]. According to equation (4.3), plotting $\ln(J_S/T^2)$ vs q/k_bT should yield a straight line for an ideal Schottky diode, in which the slope gives the junction barrier height, and the intercept gives ln(*A**). Note that the theoretical value of *A** for GaN is reported between 22.8 and 26.4 A/cm^2-K^2, depending on which value is assumed for the electron effective mass in GaN[8–10].

4.2.1 III-N diodes: deviation from idealized behavior

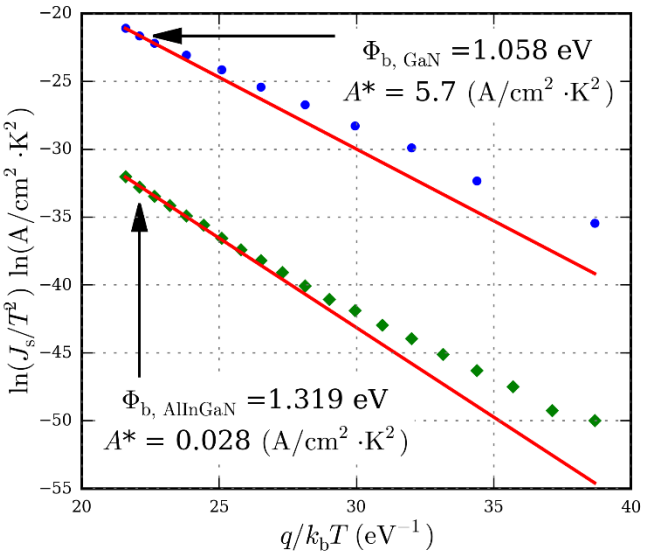

Figure 4.2. Richardson plot for a GaN (blue circles) and AlInGaN (green diamonds) Schottky diode. ϕ_b and *A** were only calculated from the highest-temperature points to mitigate effects non-idealities.

The idealized case for Schottky diode behavior does not hold in III-N materials. The Richardson plot in Figure 4.2 is nonlinear for both GaN and AlInGaN, which limited the data

extraction via linear fit to only the highest-temperature data points. The data points at the highest end of the temperature spectrum are most accurately described by equation (4.3) because diode ideality factor, *n*, was closest to unity here. These data points provided the best measurement of ideal TE current transport in a Schottky diode. Even when restricting the data extraction to the high-temperature points, the calculated *A** values extracted from the GaN diodes, 5.7 A/cm^2-K^2, was lower than the theoretical value. Discrepancy between theoretical and experimental *A** values is a common observation in studies pertaining to Schottky diodes in the nitrides and other III-V material systems[11–14].

Confidence in the *A** value extracted from the GaN diodes was bolstered by the fact that the ideality factors for the devices taken above 500K were very close to unity ($n \leq 1.03$). However, to see an *A** from the AlInGaN diodes that was orders of magnitude too low, even when fitting high-temperature data points, indicated that the standard method of applying equation (4.3) to *J-V-T* data did not sufficiently describe electron transport in these devices. Furthermore, the ideality factors of the AlInGaN diodes at temperatures above 500K were ≥ 1.10, which was significantly higher than their GaN counterparts. It was not only the high *n* value and the small magnitude of the AlInGaN *A**, but also the discrepancy between GaN and AlInGaN *A** values that suggested that the textbook picture of an ideal homojunction Schottky diode could not be applied to AlInGaN Schottky diodes.

4.3 BARRIER HEIGHT INHOMOGENEITY: SOURCE OF NON-IDEAL TRANSPORT

The Richardson plot method did not include phenomena which are known to influence Schottky diode behavior across all semiconductor material systems, such as barrier height inhomogeneity[15]. Barrier height inhomogeneity (BHI) is an extensively studied phenomenon

that greatly alters the observed conduction properties in a Schottky diode away from what would be expected from equation (4.3). Small measured A^* values, high ideality factors, and nonlinearity in $\ln(J_S/T^2)$ are all pieces of evidence of a temperature-dependent SBH, and is often attributed to BHI[11,15,16].

There are several competing theories that seek to provide a physical basis to BHI, and acceptable phenomenological explanations vary between material systems[13,15,17]. In III-N alloys grown at low temperature, such as InGaN and InAlN, it has been shown via Atom Probe Tomography (APT) that some amount of alloy fluctuations are inherent to the growth of the material, regardless of growth technique[18–20]. If one looks at the spatial distribution of the alloyed layers, the group III composition follows a binomial distribution. Furthermore, this holds true for thin quantum wells[18], as well as HEMT barrier layers, which are significantly thicker[20]. Reports suggest that the binomial alloy distribution is due to statistical nature of atom adsorption from the gas phase and other factors during growth[21], and there has been a report of AlInGaN films following this same binomial distribution under APT analysis[22].

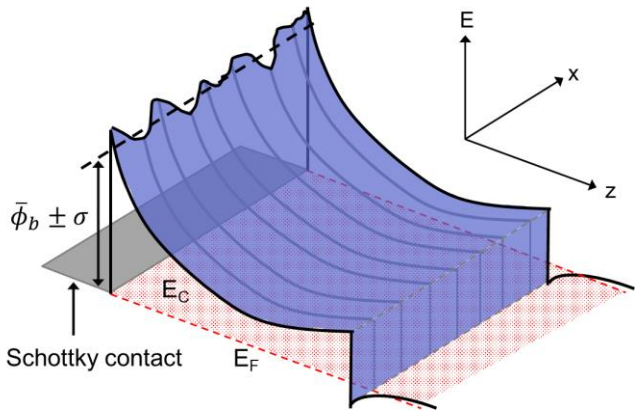

Figure 4.3. Schematic diagram of an inhomogeneous Schottky barrier to a III-N ternary or quaternary alloy. The Fermi energy is displayed as a red shaded plane; the conduction band is a blue contour bounded by black lines. This visualizes the need to describe both the SBH and the fluctuations thereof in a consistent manner.

If alloy fluctuations, which would cause fluctuations in the band gap energy (E_g) and position of the conduction band edge (relative to the Fermi level in the device structure), are responsible for barrier height inhomogeneity in III-N alloys, a more realistic band diagram of the AlInGaN devices can be viewed as the sketch in Figure 4.3. To fully characterize a SBH, it is more instructive (and potentially more useful from a technological perspective) to describe the barrier height by the mean value of a distribution, $\bar{\phi}_{\mathrm{b}}$, and its standard deviation, σ.

4.3.1 Experimental details

To characterize the nature of the proposed inhomogeneous SBH, three samples of varying indium and aluminum composition were grown by metalorganic chemical vapor deposition (MOCVD) in a Veeco P75 Turbodisc reactor. The growth conditions were described in the last chapter, and are summarized in references [23] and [24], for InAlN[23] and AlInGaN, respectively. The composition of each sample as determined by SIMS is summarized in TABLE 4.1[24]. Also included in TABLE 4.1 is an estimation of the band gap energy (E_{g}) for each material, as calculated by Sakalauskas, *et. al.*[25], and a theoretical Richardson constant, A_{T}^{*}. The theoretical Richardson constant for each of these materials was calculated using an effective mass value that was estimated via Vegard's law[8,26].

TABLE 4.1. Sample summary with relative crystal composition, approximate band gap energy, and theoretical Richardson constant values.

Sample	$\%_{\mathbf{AlN}}$	$\%_{\mathbf{InN}}$	$\%_{\mathbf{GaN}}$	$E_{\mathbf{g}}$ **(eV)**	$A_{\mathbf{T}}^{*}\left(\frac{\mathbf{A}}{\mathbf{cm^2 - K^2}}\right)$
A	35	6.5	58.5	3.86	27.2
B	51	13.8	35.2	3.88	28.7
C	53	11	36	4.09	29.40

The layer structure for the Schottky diodes consisted of a 100-nm-thick unintentionally doped AlInGaN layer on top of an n-GaN substrate, which was grown heteroepitaxially on a sapphire substrate. A BCl_3/Cl_2 reactive ion etch provided device isolation, as well as access to the n-GaN layer for Ohmic contact formation. Ti/Al/Ni/Au Ohmic contacts were annealed at 820 C in a N_2 ambient for 30 seconds, and the Ni/Au Schottky contacts were annealed at 350 C in a N_2 ambient for 15 minutes to promote uniform adhesion of the metal to the semiconductor over the entirety of the device area[27,28]. The low-temperature anneal of the Schottky contact was implemented due to variations in *J-V-T* measurements. Some samples exhibited a trend where barrier heights calculated when increasing the temperature from room temperature up to the maximum measurement temperature showed an offset from the barriers calculated when lowering the temperature back to room temperature, as seen in Figure 4.4.

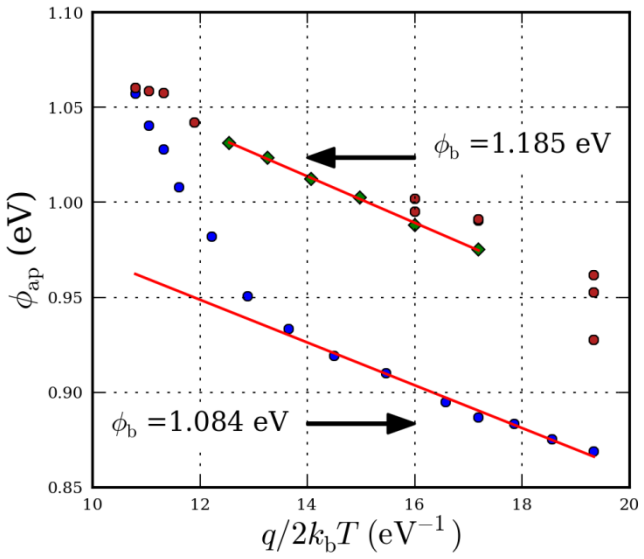

Figure 4.4. The apparent barrier height as a function of temperature for GaN displayed an offset in magnitude for values calculated as temperature was increased (green) and as temperature was decreased (blue). Incorporating a Schottky contact anneal eliminated this issue (red). Note: absolute values of Ni-GaN SBH may be overestimated due to incorrect choice in *A** for the calculations.

This effect was mitigated by introducing the Schottky contact anneal, and incorporating strict rules on the measurement procedure. All measurements were taken consecutively; that is to say, the temperature was either increased or decreased monotonically for all data points. There was no significant break in-between measurements that would necessitate a cool-down of the sample. Furthermore, temperature steps were limited to 25K; it seemed that small temperature steps yielded more consistent data, which may have to do with thermal gradients in the sample, or issues with controller stabilization for large temperature steps. Also note that the temperature was given a minimum of 10 minutes to stabilize after the ramp had completed due to sample size and the poor thermal conductivity of the sapphire substrates.

4.4 DESCRIBING THE INHOMOGENEOUS AlInGaN SBH

4.4.1 Empirical correction factor for non-linear Richardson plot

Temperature-dependent current-voltage measurements were collected but, instead of performing the typical Richardson plot analysis, a popular empirical method was employed to account for the SBH BHI[15,16]. This method modified the analysis of the collected data by scaling the x-variable of the Richardson plot by the ideality factor, so now the plot changes to $\ln(J_S/T^2)$ vs q/nk_bT. Making such a variable substitution corrects for non-idealities in the *J-V* characteristics of the AlInGaN Schottky diodes, and the subsequent extraction of SBH and *A** was identical to the unaltered Richardson plot analysis. Utilizing this empirical method yielded the data in Figure 4.5, which is summarized in TABLE II. Multiple data points were collected at each measurement temperature, and experimental error on the fit parameters was determined by a simple linear regression.

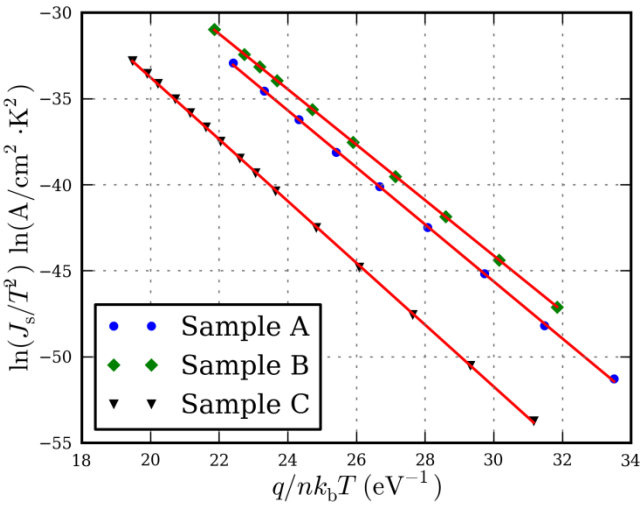

Figure 4.5. Empirically corrected Richardson plot for ϕ_b and A^* extraction. The linearity of data is improved compared to Figure 4.1. For clarity, only the average value of $ln(J_s/T^2)$ is plotted for each temperature.

This empirical method was useful due to the success with which other groups have seen with their implementation. Previous reports in a variety of material systems indicate that utilizing this empirical correction allowed for the extraction of $\bar{\phi}_b$ and A^* values that were in better agreement with theoretical expectations[15,16,29]. This method was also useful for establishing baseline numbers for ϕ_b that could be used for judging the validity of other BHI analysis methods of *J-V-T* data. However, this "correction" for the barrier height inhomogeneity was not particularly enlightening. While it does give a more realistic account of ϕ_b and A^*, it does not give a description of what kind of a correction is being made, nor is there a clear answer to why A^* recovers to a number that agrees better with theoretical calculations. Furthermore, an implicit assumption is required in this method is that the ideality factor affects not only the voltage-dependent term in the diode equation, but it also causes some sort of voltage partitioning in J_S, and that must hold even at 0V of applied bias. The reasoning behind voltage partitioning of diode saturation current is not obvious.

4.4.2 Polynomial fitting to non-linear Richardson plot data

In order to develop a more detailed understanding of AlInGaN Schottky diode behavior, and to provide evidence in support of alloy fluctuations inducing BHI, it was necessary to establish the assumptions which must be satisfied for this interpretation:

1. AlInGaN alloy composition follows the same spatial distribution as InAlN and InGaN
2. E_g, and fluctuations thereof, are reflected in $Al_xIn_yGa_{(1-x-y)}N$ crystal composition
3. Fluctuations in SBH mimic the functional form of fluctuations in E_g
4. Predominant conduction mechanism is thermionic emission, though the electrons may be emitted over many barrier heights

The first three assumptions may be distilled into a requirement that the functional form of the spatial distribution of the alloy fluctuations, and thus SBH, must be known (or assumed). APT suggested the use of a binomial alloy distribution, but only samples a small area. A Schottky diode samples current from a much larger area, and therefore samples many more points from the barrier height distribution. If the sample size of a binomial distribution becomes very large, as it does when increasing area from an APT sample to a diode, it approaches a Gaussian distribution[30]. Consequently, under the assumption that the barrier height distribution is caused by crystal composition fluctuations, AlInGaN diode *J-V* can be accurately described by barrier-limited transport over a Gaussian barrier height distribution underneath the Schottky contact. The fourth assumption was fulfilled by restricting data collection to a regime in which thermionic emission was the only significant contributor to electrical conduction. Over the course of data collection, it was found that *J-V-T* data should only be considered at room temperature and above. Diode ideality factor was close to unity for all samples in this temperature range (n ~ 1.05-1.23). Low n implied that current flow was dominated by

thermionic emission for measurements at 300K and above. With these requirements in mind, a mathematical framework was adapted form Chand and Kumar that described thermionic emission over a Gaussian distribution of barrier heights[31].

To account for the current flow over all possible barrier heights, it is necessary for the diode saturation current to include a term that represents the probability density function of the barrier height distribution:

$$J_0 = \int J_S(\phi_b) P(\phi_b) d\phi_b, \tag{4.4}$$

where

$$J_S(\phi_b) = A^* T^2 exp\left(-\frac{q\phi_b}{k_b T}\right) \tag{4.5}$$

is the diode saturation current for a single barrier height, and

$$P(\phi_b) = \frac{1}{\sigma\sqrt{2\pi}} exp\left(-\frac{(\phi_b - \bar{\phi}_b)^2}{2\sigma^2}\right) \tag{4.6}$$

is a Gaussian probability density function with a mean value of $\bar{\phi}_b$ and a standard deviation of σ. Carrying out the integral over all possible barrier heights, (-∞,+∞), and performing a variable substitution of $u = q(\phi_b - \bar{\phi}_b)/k_b T$ yields

$$J_0 = \frac{A^* T^2}{\sigma\sqrt{2\pi}} \exp\left(-\frac{q\bar{\phi}_b}{k_b T}\right) \int_{-\infty}^{+\infty} \exp\left(-\frac{u^2}{2\sigma^2} - u\right) du. \tag{4.7}$$

This integral in equation (4.7), *I*, can be found in an integral table, and evaluates to

$$I = \int_{-\infty}^{+\infty} \exp\left(-\frac{u^2}{2\sigma^2} - u\right) du = \sqrt{2\pi}\sigma \exp(2\sigma^2). \tag{4.8a}$$

With appropriate variable substitution, J_0 simplifies to

$$J_0 = A^* T^2 \exp\left(-\frac{q\phi_{ap}}{k_b T}\right), \tag{4.8b}$$

where

$$\phi_{ap} = \left(\bar{\phi}_b - \frac{q\sigma^2}{2k_b T}\right) \tag{4.8c}$$

is the apparent barrier height of the diode at a particular temperature. The temperature dependence of the apparent barrier height, and its deviation from the mean, is dependent upon the spread in the distribution of barrier heights underneath the Schottky contact. Equation (4.7b) shows that the apparent barrier height decreases with decreasing temperature, thus giving a source to the nonlinearity of the Richardson plot. $\phi_{\mathrm{ap}} < \bar{\phi}_{\mathrm{b}}$ also explains why J_S is larger than expected with decreasing temperature.

Chand and Kumar proposed utilizing equations (8b) and (8c) to find σ and perform a linear fit to a "Modified Richardson Plot" in which the J_0/T^2 data is scaled by the term containing σ in equation (4.8c). However, doing so requires prior knowledge, or a very good guess, of A^*. Instead, rewriting (8b) and (8c) as

$$\ln\left(\frac{J_0}{T^2}\right) = \ln(A^*) - \bar{\phi}_{\mathrm{b}}x + \frac{\sigma^2}{2}x^2 \text{ , where } x = \frac{q}{k_{\mathrm{b}}T}, \tag{4.9}$$

avoids this limitation by applying a fit of a quadratic function to the experimental data. Using a second order polynomial to fit the data allows one to find all quantities of interest from each of the regression coefficients. This also avoids the need to apply any scaling factor to the data, as was necessary with the empirical correction method, as well as the original method proposed by Chand and Kumar.

4.5 REGRESSION RESULTS AND ANALYSIS

Equation (4.9) was fit to the experimental data via multiple linear regression. The best fit for the coefficients in equation (4.9) was determined by minimizing the sum of the squares of the residuals over all measurements of $\ln(J_0/T^2)$, known as the least squares method[30].

$$e_{\mathrm{i}} = y_{\mathrm{i}} - \hat{y}_{\mathrm{i}} \tag{4.10}$$

is the residual, defined as the difference between y_i, the experimental value ($\ln(J_{0,i}/T_i^2)$), and $\hat{y}_i$, the fitted value from equation (4.9). Figure 4.6 shows the average $\ln(J_0/T^2)$ data for each sample, along with the regression for each sample. The second order polynomial shows excellent fidelity to the experimental data. The residuals, which were calculated for each measurement of $\ln(J_{0,i}/T_i^2)$, were also used to calculate the standard error of each regression coefficient[30]. An excellent primer on multiple linear regression can be found in Schaum's Outline on Statistics and Econometrics[30].

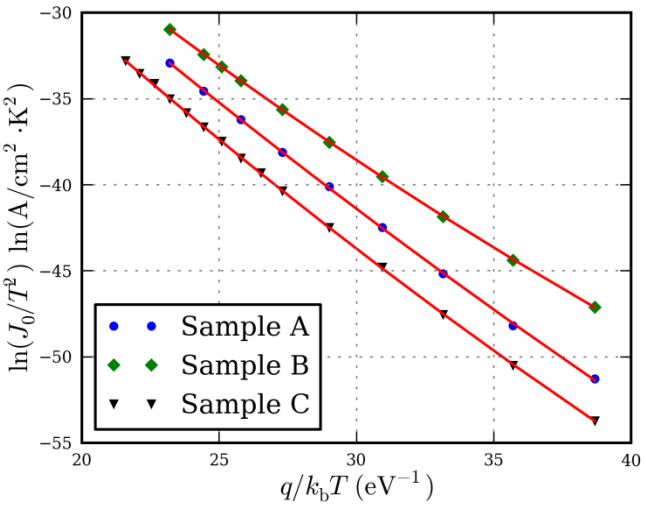

Figure 4.6. Quadratic fit to the experimental $\ln(J_0/T^2)$ data. Note that each data point is an average value of multiple measurements; error bars on data points were omitted for the sake of figure clarity.

Regression analysis gave a mean value and standard error on the regression coefficients. The standard error was that for $\ln(A^*)$, but the quantity of interest was A^*. The result was that the upper and lower bounds on A^* were highly asymmetrical with respect to the mean value. For example, from TABLE 4.2, the upper bound of A^* for sample A was $\exp(\ln(A^*) + \Delta\ln(A^*)) = \exp(0.377 + 0.926) = 3.68$ A/cm^2-K^2, while the lower bound was $\exp(0.377 - 0.926) = 0.58$ A/cm^2-K^2. The mean values for $\ln(A^*)$ were exponentiated so the average A^* for each sample could be displayed for the reader. In a similar vein, the regression coefficient

involving σ was $\sigma^2/2$. Fortunately, the upper and lower bounds of σ were only slightly asymmetrical with respect to the mean. After rounding, any asymmetry was unnoticeable, thus the upper and lower bounds were quoted directly for σ. The parameters calculated from the regression, as well as the standard error for each, are summarized in TABLE 4.2.

TABLE 4.2. Summary of data from both fitting methods. Error analysis from regression was performed on fit parameters, thus the error bars on A^* are highly asymmetrical. Experimental uncertainty in $\ln(A^*)$ is reported, along with the nominal value of A^*.

	Empirical Method			**Quadratic Fit Extraction**			
Sample	$\bar{\phi}_b$ **(eV)**	$\ln(A^*)$	$A^*\left(\frac{A}{cm^2 \cdot K^2}\right)$	$\bar{\phi}_b$ **(eV)**	σ **(eV)**	$\ln(A^*)$	$A^*\left(\frac{A}{cm^2 \cdot K^2}\right)$
A	1.65 ± 0.006	3.88 ± 0.17	48.4	1.58 ± 0.06	0.112 ± 0.009	0.377 ± 0.926	1.45
B	1.61 ± 0.003	4.21 ± 0.09	67.6	1.57 ± 0.03	0.130 ± 0.004	0.884 ± 0.497	2.41
C	1.80 ± 0.003	2.17 ± 0.07	8.76	1.74 ± 0.02	0.130 ± 0.003	0.733 ± 0.317	2.08

4.6 DISCUSSION

The parameters from the fit were examined in terms of their relation to the band gap of each sample, and the crystal composition of each sample. E_g and crystal composition were the only two characteristics that could be determined independently by material analysis. Since the operational theory for the source of barrier height inhomogeneity was related to compositional fluctuations, the ultimate goal was to evaluate the extent to which $\bar{\phi}_b$, σ, and A^*

vary with E_g and/or crystal composition. Furthermore, the main mechanism for control during epitaxial growth is crystal composition. For this section, keep in mind the following:

1. Samples A and B are compositionally disparate, with B having much larger X_{InN} and X_{AlN}, but have nearly identical band gap energies
2. Samples B and C are compositionally similar, but C has a larger E_g by 0.2 eV

4.6.1 Average Schottky barrier height

Comparing $\bar{\phi}_b$ values in TABLE II with the sample data available in TABLE I, there is a clear correlation between $\bar{\phi}_b$ and E_g: sample C, with the largest E_g, displayed a larger $\bar{\phi}_b$ than samples A and B. Furthermore, samples A and B had nearly identical E_g and $\bar{\phi}_b$ values in spite of significantly higher X_{InN} and X_{AlN} in sample B. There was no clear relationship between $\bar{\phi}_b$ and crystal composition. Juxtaposing with samples A and B that were compositionally disparate with similar $\bar{\phi}_b$ values, samples B and C were compositionally similar with a disparity in $\bar{\phi}_b$ values. These pieces of information confirm that $\bar{\phi}_b$ is unrelated to the precise chemical makeup of the AlInGaN alloy, and is instead related to the E_g of the material. This also implies that all AlInGaN of the same band gap, regardless of composition, can be predicted to have the same $\bar{\phi}_b$ to nickel.

The observation of increasing SBH to a given metal with increasing E_g has two likely explanations. The first is from a difference between the metal work function and semiconductor electron affinity[7]:

$$\phi_b = \phi_m - \chi, \tag{4.11}$$

where ϕ_m is the metal work function and χ is the semiconductor electron affinity. As the band gap of AlInGaN increases, it is expected that its electron affinity will decrease, thus increasing

the magnitude of the difference in equation (4.11). The second is due to pinning of the Fermi level near the semiconductor surface, $E_{F,S}$, by a deep level. The energy state of a deep level is not coupled to the valence or conduction band of the semiconductor. If the energy level of a deep trap state is considered as a fixed reference point then, as the band gap increases, the energy difference between the conduction band edge and the trap level can increase, and yield a larger SBH. Such an explanation would require evidence of a trap level with a large density of states in a narrow energy range to be capable of pinning $E_{F,S}$.

To distinguish between these two cases for SBH formation, the electron-affinity-related barrier height was calculated with equation (4.11). Depending on agreement with these calculations and experimental results, SBH formation due to work function difference may be supported or ruled out. The work function for nickel is 5.01 eV[32] and, the electron affinity for AlInGaN was estimated using Vegard's law and the electron affinity values for the binary nitrides[8]. ϕ_b values from equation (4.11) are shown in TABLE 4.3, which are quoted alongside the barrier height values obtained from the polynomial fit extraction.

TABLE 4.3. Comparison of SBH as calculated from equation (4.11) and the quadratic fit to *J-V-T* data. The electron affinity-based calculation overestimates ϕ_b, and trends in ϕ_b do not match experimental observations.

Sample	E_g **(eV)**	ϕ_b **(eV)**	$\bar{\phi}_b$ **(eV)**
A	3.86	2.27	1.58±0.06
B	3.88	2.77	1.57±0.033
C	4.08	2.63	1.74±0.022

Not only does this yield barrier heights that are significantly overestimated, but $\phi_b(A)$ and $\phi_b(B)$ should be nearly identical, according to experimental data. Consequently, it is

necessary to conclude that the Fermi level at the surface of the semiconductor is not determined by a simple $\chi - \phi_b$ difference between it and the Schottky metal.

4.6.2 AlInGaN surface analysis for oxidation and Fermi level pinning

Strong Fermi level pinning has been reported in AlGaN HEMTs by Higashiwaki, *et al.*[33] In their study, it was found that annealing their AlGaN films at 800 C for one minute in a N_2 atmosphere in a rapid thermal annealing (RTA) tool yielded an oxidized surface. These oxidized AlGaN samples were measured by x-ray photoelectron spectroscopy (XPS), and were found to have surface potentials that were independent of AlGaN thickness, thus indicating that the Fermi level was pinned at a particular energy. Subsequent first-principles calculations confirmed that oxides which form under these conditions can yield a high density of donor states in a narrow energy range. Due to the fact that the samples in this study were annealed under similar conditions in the same exact RTA tool used by Dr. Higashiwaki, XPS analysis was performed on these samples to assess the presence of surface oxidation and estimate the surface barrier height of un-metallized AlInGaN surfaces. The data is summarized in Figures 4.7 and 4.8.

XPS scans of the AlInGaN surfaces were performed at a 60º angle to the incident x-ray beam. This was done to ensure the photoelectrons collected in the experiment originated from as close to the surface as possible[33]. This would allow for the discrimination of surface chemistry, and the position of the valence band maximum relative to $E_{F,S}$, from those of the bulk of the material. Figure 7 shows high-resolution XPS spectra of the aluminum, gallium, and indium bond chemistry at the surface of the sample. Fitting the asymmetric experimental data peaks revealed extensive oxidation of the aluminum and gallium sites near the surface, with significantly less oxidation of the indium sites. Furthermore, it should be noted that the

XPS signal strength of the metal-oxide bond was much stronger for 60º incidence than it was for normal incidence. Since the XPS signal is more localized to the surface for greater tilt away from normal incidence, this provided supporting evidence that the oxidation of the group-III sites in the crystal was confined to the surface of the material.

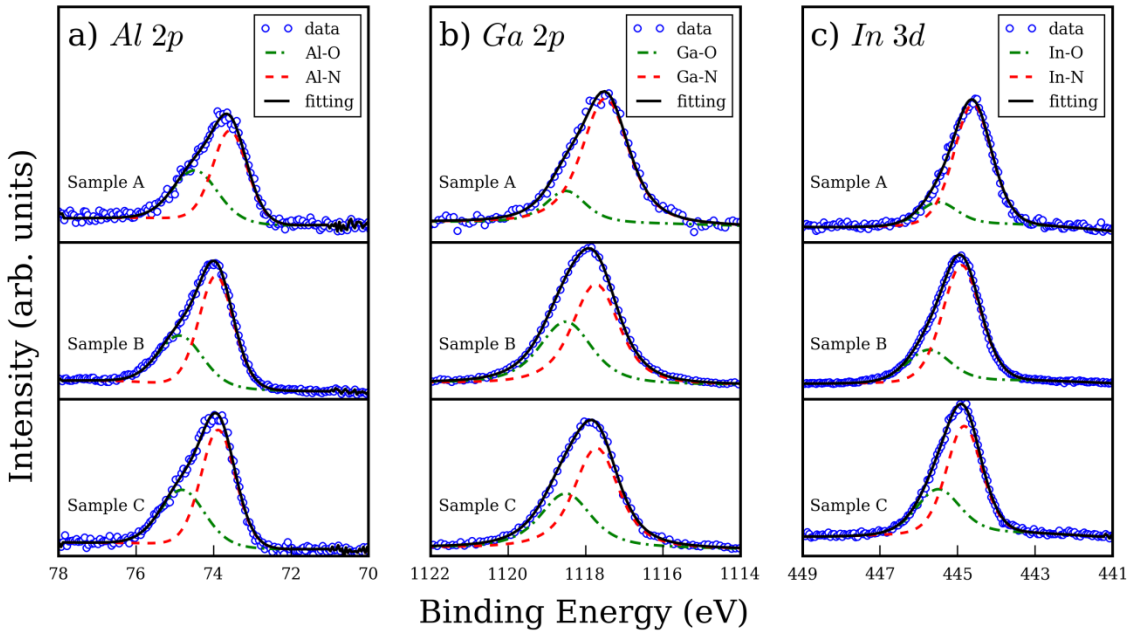

Figure 4.7. The XPS spectra taken for each Schottky diode sample at a 60° tilt to the X-ray source. The Al 2p (a) and Ga 2p spectra (b) for all three samples show extensive oxidation near the surface. The In 3d peaks (c) display a smaller amount of oxidation.

Figure 4.8 shows XPS spectra for the valence band edge of the AlInGaN samples. In Figure 4.8, $E_{F,S}$ is located at 0 eV. The position of the valence band maximum, E_V, was calculated by performing a linear fit to the falling edge of the XPS signal and calculating the intercept of the fit to the x-axis[33]. The approximate E_g for each of the samples is known (see TABLE 4.1), so it is possible to apply

$$E_g = (E_V - E_{F,S}) + (E_{F,S} - E_C), \tag{4.12}$$

where E_C is the position of the conduction band minimum. Since XPS a spectroscopic measurement of electron binding energy, E_V has a positive binding energy, $E_{F,S}$ has zero binding energy, and E_C would have a "negative binding energy".

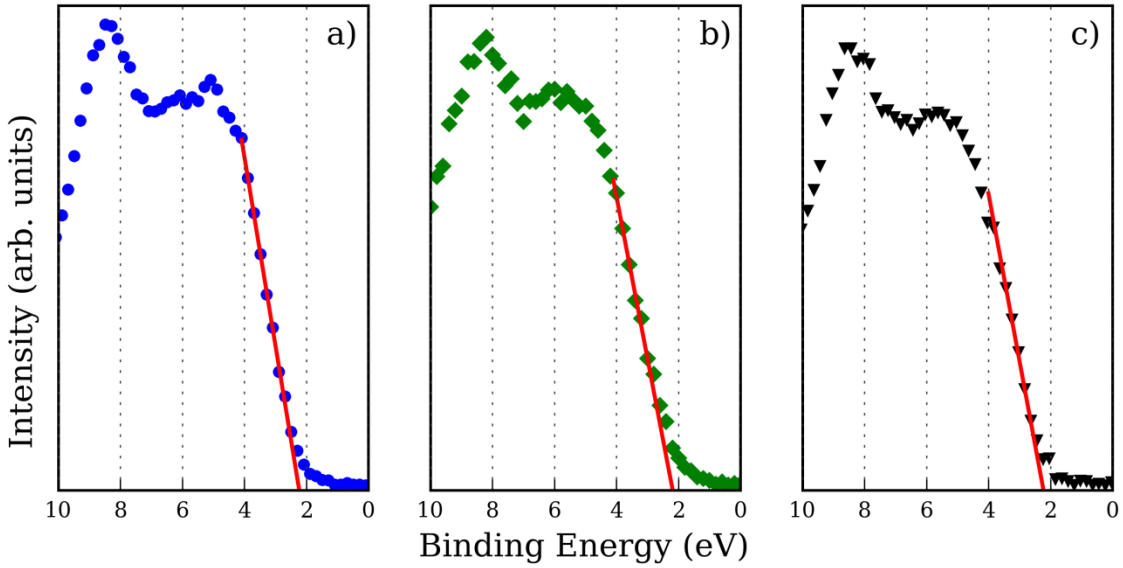

Figure 4.8 shows the linear fit to the trailing edge of the XPS spectra for each AlInGaN sample. 4.8a), 4.8b), and 4.8c) correspond to Schottky diode samples A, B, and C.

Due to the signage involved with quantities calculated from XPS, the surface barrier height is $\phi_{b,XPS} = E_{F,S} - E_C$, though the convention in the field of physical electronics is to write it as $\phi_b = E_C - E_{F,S}$. The quantities are identical. The barrier height of the free surface of the AlInGaN samples can then be determined by

$$\phi_{b,XPS} = E_g - (E_V - E_{F,S}), \tag{4.13}$$

which is the difference between the band gap energy and the amount of the band gap spanning from the position of the valence band maximum to the position of the Fermi level at the surface. The surface barrier height values calculated from XPS are summarized in TABLE 4.4.

TABLE 4.4. XPS surface barrier heights reported alongside $\overline{\phi}_b$ calculated from equation (4.9). The agreement in ϕ_b between methods shows that $E_{F,S}$ is pinned by a high density of donor states in a narrow energy range.

Sample	$\phi_{b,XPS}$ (eV)	$\overline{\phi}_b$ (eV)
A	1.59 ± 0.06	1.58 ± 0.06
B	1.54 ± 0.05	1.57 ± 0.033
C	1.85 ± 0.08	1.74 ± 0.022

It is apparent that the surface barrier height is constant regardless of the surface being metallized or un-metallized, due to the similarity of $\phi_{b,XPS}$ to $\overline{\phi}_b$. It can therefore be concluded that the surface oxide which exists on these AlInGaN samples introduced a high density of deep, donor-like states that have pinned the Fermi level at the surface at a particular energy below the conduction band of the materials.

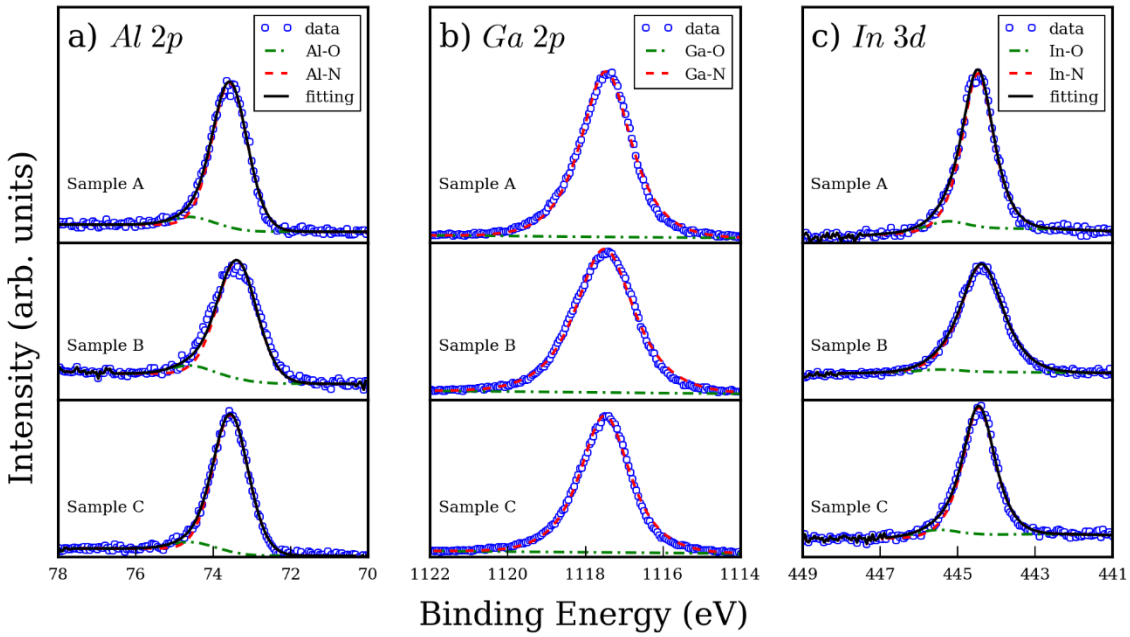

Figure 4.9 shows the effectiveness of HF at removing all metal-oxides from the AlInGaN surface.

The capabilities of two acid chemistries, HF and HCl, to remove the AlInGaN surface oxides and alter the Fermi level pinning position were evaluated. Two portions of each sample were separated for HF and HCl dips. The HF dip was performed for 1 minute in 48% concentrated HF. The standard pre-metallization HCl dip for Ga-polar GaN was utilized: 1 minute in a solution of 3:1 H_2O:HCl. After acid treatment, samples were vacuum sealed and quickly loaded into the XPS tool to minimize atmospheric oxidation.

It was found that HF could remove nearly all traces Al-O bonding, and was successful in completely eliminating all Ga-O and In-O bonding (Figure 4.9), at the expense of fluoridating the surface. Changes in the band bending at the surface were minor: 0.14 eV at maximum. HCl was only effective at removing Ga-O related bond signatures; In-O and Al-O remained (Figure 4.10).

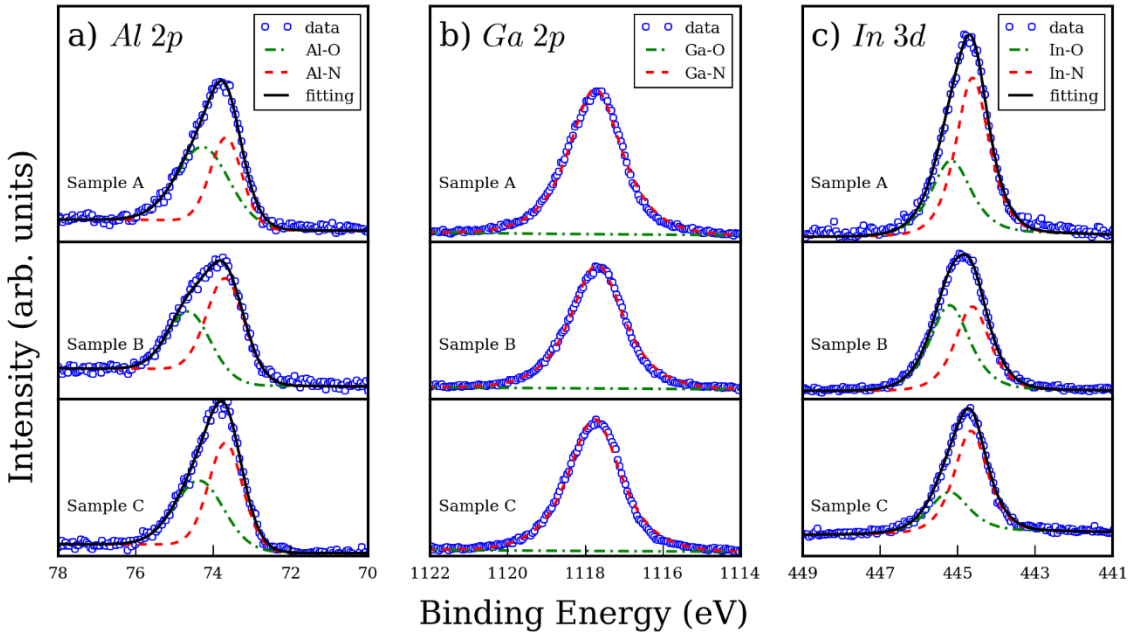

Figure 4.10 shows the result of HCl treatment on AlInGaN. Only Ga-O bonding is eliminated by this method.

Furthermore, HCl chlorinated the surface of the semiconductor, but the effect of HCl on ϕ_b was smaller than the effect of HF. This was likely due to the fact that much of the oxide,

and therefore the source of Fermi level pinning, was undisturbed in these samples by the acid dip. Results of ϕ_b modification are summarized in TABLE 4.5.

TABLE 4.5 shows the surface barrier heights of the AlInGaN samples as measured by XPS after HF and HCl treatments. Also included are the differences from the original XPS barrier heights, Δ_{HF} and Δ_{HCl}.

Sample	$\phi_{b,HF}$ **(eV)**	Δ_{HF} **(eV)**	$\phi_{b,HCl}$ **(eV)**	Δ_{HCl} **(eV)**
A	1.64 ± 0.14	+0.05	1.64 ± 0.10	+0.05
B	1.68 ± 0.19	+0.14	1.64 ± 0.10	+0.10
C	1.98 ± 0.12	+0.13	1.82 ± 0.11	-0.03

4.6.3 Effects of surface oxide on A*

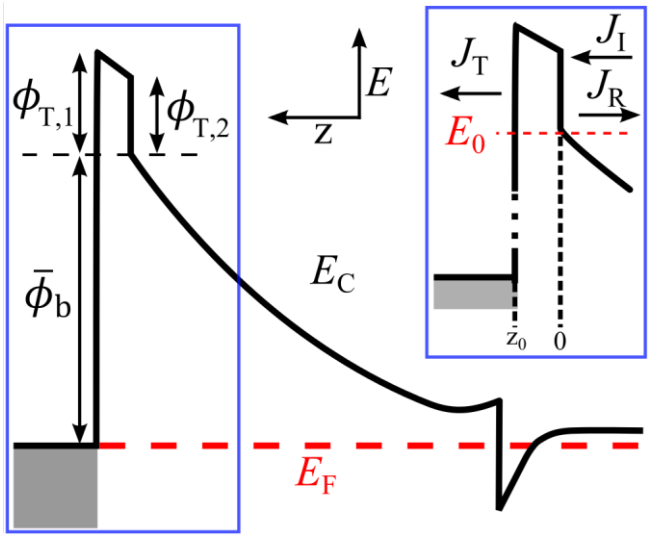

Figure 4.11. The band diagram of an AlInGaN/GaN heterojunction Schottky diode with a surface oxide interlayer. $\phi_{T,1}$ and $\phi_{T,2}$ indicate the potential energy barriers that determine transmission and reflection at the barrier. The inset of the figure displays the probability current densities that result from quantum mechanical scattering: J_I, J_R, and J_T, are the incident, reflected, and transmitted probability current densities, respectively.

From the XPS data acquired for these samples, it has become apparent that the oxidation of the sample only exists within the top monolayers of the sample surface. The presence of an oxide in such a position would introduce a very thin layer with a larger band gap and positive conduction band offset to AlInGaN, as illustrated in Figure 4.11. This thin oxide layer would then function as a tunneling barrier to current flow, consequently acting as a "current choke" and limiting the current density of the device.

A discontinuity in the bands due to a tunneling barrier should affect the population of thermal carriers traversing the interface at any bias. Thus, the magnitude of J_S should be affected, though there must also be a bias- and temperature-dependent element to the tunneling probability. Figure 4.2 shows that J_S*(AlInGaN)* is smaller than J_S*(GaN)* for all temperatures. A portion of the difference in J_S is the larger $\phi_{b,AlInGaN}$. If the difference in current were only due to an increase in barrier height (1.0 eV to ~ 1.3 eV), the value of $\ln(J_S/T^2)$ at room temperature for the AlInGaN diode should be about -45, according to the data in Figure 4.2. However, the actual value is much smaller at –50. This additional suppression in J_S between GaN and AlInGaN is likely due to tunneling through the surface oxide layer. Since model represented by equation (4.9) does not take tunneling of carriers into account, the impact of tunneling must be absorbed by one of the terms in the equation.

The inset to Figure 4.11 shows that an oxide interlayer can be treated from a quantum mechanical scattering approach. Consider the current density at the points $z = -\varepsilon$ and $z = z_0 + \varepsilon$, two points spaced an infinitesimal distance ε away from the barrier on either side. The transmitted probability density of a stream of particles can be related to the incident probability current density by

$$1 = \frac{J_R}{J_I} + \frac{J_T}{J_I} = \rho + \tau, \text{ and} \qquad (4.14a)$$

$$J_{\mathrm{T}} = \tau \cdot J_{\mathrm{I}}, \tag{4.14b}$$

where ρ is the reflection coefficient for the electrons incident upon the barrier, τ is the transmission coefficient, and J_{I}, J_{T}, and J_{R} are the incident, transmitted, and reflected probability current densities, respectively. Probability current density in one dimension is in units of particle flux, and can be equated to electrical current density in the device by scaling it with the electron charge[34]. From thermionic emission theory, J_{I} must be given by the portion of the diode current equation due to electrons moving from the semiconductor to the metal[7,10]. J_{T} can then be rewritten as

$$J_{\mathrm{T}} = \tau \cdot J_{\mathrm{S}} \cdot \exp\left(\frac{qV}{k_{\mathrm{b}}T}\right). \tag{4.15}$$

However, since tunneling should affect the transport of electrons across the barrier at any bias, the effect of τ should also be seen at $V = 0$, and impact J_{S} directly:

$$J_{\mathrm{T}} = \tau \cdot J_{\mathrm{S}} = \tau \cdot A^{*}T^{2} \exp\left(\frac{q\phi_{\mathrm{ap}}}{2k_{\mathrm{b}}T}\right) \tag{4.16a}$$

$$= \tau \cdot A^{*}T^{2} \exp\left[\frac{q}{2k_{\mathrm{b}}T} \cdot \left(\bar{\phi}_{\mathrm{b}} - \frac{q\sigma^{2}}{2k_{\mathrm{b}}T}\right)\right]. \tag{4.16b}$$

Equation (4.16b) shows that a tunneling probability < 1 will suppress the magnitude of saturation current extracted from diode measurements. Furthermore, the presence of τ slightly alters the result of equation (4.9):

$$\ln\left(\frac{J_{\mathrm{T}}}{T^{2}}\right) = \ln(A^{*} \cdot \tau) - \bar{\phi}_{\mathrm{b}}x + \frac{\sigma^{2}}{2}x^{2}, \text{ where } x = \frac{q}{k_{\mathrm{b}}T}. \tag{4.17}$$

Therefore, the consequence of a tunneling barrier at the metal-semiconductor junction is only reflected in one of the regression coefficients. For the model in equation (4.9), what is assumed to be an accurate measure of A^{*} is actually $A^{*} \cdot \tau$. However, since the transmission coefficient has no direct impact upon the x or x^{2} terms of equation (4.17), the extracted values of $\bar{\phi}_{\mathrm{b}}$ and σ are reliable.

Before the extent of the impact of tunneling on current density can be evaluated, it is necessary to evaluate the magnitude of τ for several cases. First consider a GaN homojunction Schottky diode. Experimental data for this exists at $A^{*}\cdot\tau$ = 5.7 A/cm^2-K^2, A^{*} is known to be between 22.8-26.4, yielding τ = 0.22 – 0.25. Next, consider the results of a simulated GaN diode, which utilized the fully quantum mechanical software written by Trey Suntrup[26]. Simulated results provided $A^{*}\cdot\tau \sim$ 5.33 A/cm^2-K^2, yielding τ = 0.202-0.234. Given the excellent agreement between simulation and experimental results, simulations proceeded to AlInGaN diodes.

To provide an accurate estimation of $A^{*}\cdot\tau$ and τ without an oxide interlayer, an ideal homojunction band diagram (Figure 4.12) with a step function-like potential was used for the simulation.

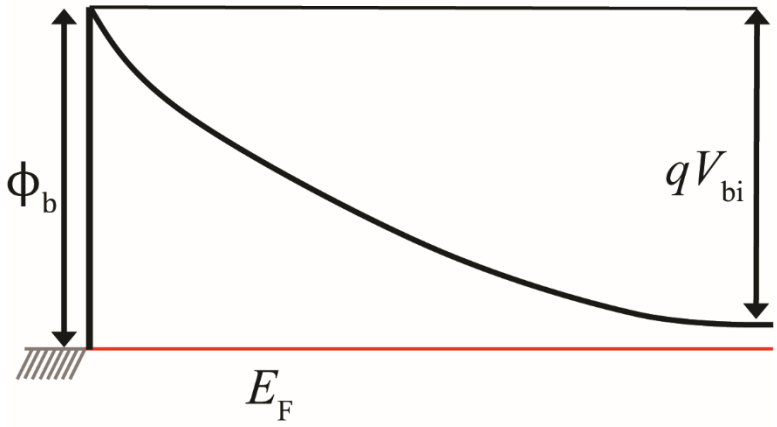

Figure 4.12. Ideal Schottky diode homojunction used for quantum mechanical calculations. At forward bias, this looks like a step down potential as seen in Chapter 2 of Kroemer's textbook *Quantum Mechanics*[34].

$A^{*}\cdot\tau$ was calculated using both ϕ_{ap} and $\bar{\phi}_b$ to provide the widest possible range of observable $A^{*}\cdot\tau$ values **in the absence of a tunneling barrier (oxide interlayer)**. The results are summarized in TABLE 4.6, and also include the calculated τ values from the experimental AlInGaN Schottky diodes.

TABLE 4.6 summarizes the experimental (expt) and computational (sim) calculations for $A^* \cdot \tau$ and τ. Experimental τ values vary between 13% - 32% of simulated values. $A^* \cdot \tau$ can be improved by at least a factor of 3 if adequate oxide removal techniques are implemented. All table entries are in units of A/cm^2-K^2.

Sample	$A^* \cdot \tau$ **(sim)**	$A^* \cdot \tau$ **(expt)**	τ **(sim)**	τ **(expt)**
GaN	5.33-6.89	5.7	0.22-0.30	0.20-0.23
A	9.48-9.95	1.45	0.34-0.36	0.046-0.053
B	7.59-11.84	2.41	0.26-0.41	0.069-0.084
C	7.00-12.97	2.08	0.24-0.44	0.059-0.071

From these results confirm that the value of τ is much smaller in the experimental AlInGaN Schottky diodes than in the simulated diodes with the ideal step-potential-like interface. This agrees with the trends in GaN vs. AlInGaN experimental $A^* \cdot \tau$ measurements, and is compatible with the other expectations of how an interfacial oxide should behave in these devices. These results also confirm the "current choke" effect of the oxide interlayer.

The difference in A^* between GaN and AlInGaN can ultimately be sourced to the processing steps prior to Schottky diode metallization. In both materials, a surface oxide was formed during Ohmic contact annealing. In the GaN sample, the surface was treated with HCl prior to Schottky contact metallization to remove the surface oxide. This was not possible in the AlInGaN sample. The surface oxide in the AlInGaN samples is primarily aluminum oxide, which would require HF for removal. However, the contact pads for these diodes were isolated by SiO_2, making it impossible to perform an HF dip on the diodes prior to metallization. Therefore, the Schottky contact had to be placed on top of the thin surface oxide layer.

Comparing the $A^* \cdot \tau$ results in TABLE 4.6 with the diode equation in equation (4.16b), it is clear that the AlInGaN diode forward bias current could be increased by at least 300% if proper oxide removal techniques are used in diode processing. Combined with their excellent reverse bias characteristics (Figure 4.1), achieving very high forward bias current density could make these devices quite technologically useful, especially for applications that would benefit from lattice-matched electronics. XPS results from section 4.6.2 show that the technological capability exists to appropriately remove the surface oxide via HF without significantly altering the Schottky barrier height. It is expected that the next generation of devices will yield larger forward bias current densities with comparable reverse bias leakage characteristics.

As evidenced by the results of our quantum mechanical diode simulations, the metal-semiconductor interface is subject to quantum mechanical reflections, even without a tunneling barrier at the surface. In order to better understand thermionic emission current and *A** better, *J-V-T* experiments were performed on isotype heterojunction diodes n-i-n, where the barrier is induced by an InGaN polarization dipole layer. Results from these experiments demonstrated an *A** of 24 A/cm^2-K^2 [35]. This observation fits in with the theory of quantum mechanical reflections affecting *A** and suppressing diode current. In a unipolar diode, both contacts are Ohmic. Furthermore, the barrier is induced by a polarization dipole, so the abrupt potential energy discontinuity in such structures (ΔE_c) is much smaller. With fewer interfaces that yield a smaller magnitude of quantum mechanical reflections, the expectation is that τ would be much closer to unity, and the regression coefficient $\ln(A^* \cdot \tau)$ is more accurately reflective of *A** itself. It may therefore be possible to demonstrate comparably low reverse bias current density but significantly larger, up to 4x larger, forward bias current density in isotype III-N

diodes as with Schottky diodes. If such a device is achieved, it may be able to replace the III-N Schottky diode in applications where maximizing forward bias diode current is a priority.

4.6.4 σ: *the standard deviation in* $\overline{\Phi}_b$

In this study, alloy composition fluctuations were parametrized by their effect on the distribution of Schottky barrier heights in diode samples. The standard deviation in the SBH distribution, σ, was put forth as a result of alloy composition fluctuations in the crystal, which are deviations from the average crystal composition. σ increased with increasing X_{InN} and X_{AlN}, yet did not seem to depend on the E_g of the sample. This observation was compatible with previous findings in ternary alloys, which mainly attributed spatial inhomogeneity in alloy composition to indium segregating into relatively X_{InN}-rich and X_{InN}-poor regions during growth, and there is also some evidence that alloy fluctuations exist in AlGaN alloys[36]. APT results suggest that indium content fluctuations are statistical in nature and take place over the scale of tens of nanometers. Furthermore, it is intuitive that the value of σ would be most sensitive to the phenomenon that results in the BHI, deviations in alloy composition from the mean, and not $\bar{\phi}_b$, which is instead related to E_g (and therefore the mean alloy composition).

Comparing samples A, B, and C revealed that B and C (similar composition, different E_g) had similar values for σ, while sample A (smaller X_{AlN} and X_{InN}) had a smaller degree of barrier height fluctuation. The difference in σ between samples A and B was larger than the maximum possible experimental error between the two measurements of σ_A and σ_B. The sum of the standard error in σ was $\Delta\sigma_A + \Delta\sigma_B = 0.013$, while the difference in standard deviation values was $\sigma_A - \sigma_B = 0.018$. There is therefore a distinct increase in σ when comparing sample A to samples B and C. It is consequently implied that the magnitude of alloy fluctuations is greater in samples B and C than sample A. This means that the magnitudes of

fluctuations in $\bar{\phi}_b$ as well as alloy composition are larger in samples B and C than they are in sample A. Thus, as average X_{InN} and X_{AlN} increase, so do the deviations from the mean. From the point of view of statistics, E_g and $\bar{\phi}_b$ are both related to the first moment of the alloy composition distribution (the mean). Fluctuations in the E_g and the value of σ are related to the second moment of the alloy composition distribution (the variance).

The relationship between crystal composition, σ, and ϕ_{ap} can be applied to material selection in device design. Equation (4.8c), shows that the apparent barrier height, ϕ_{ap}, at any given temperature decreases as σ increases, while $d\phi_{ap}/dT$ increases as σ increases. Therefore, a material with a larger overall X_{InN} and X_{AlN} will display a lower barrier to conduction, as well as more variability in the apparent barrier with operating temperature, than a material with a relatively lower X_{InN} and X_{AlN}, even if they have identical E_g (i.e. samples A vs B; see Figure 4.11). This can be an important design factor for vertical electronic devices, but it can also affect material selection for HEMTs if the design constraints demand extremely low gate leakage, or operation over a wide temperature range.

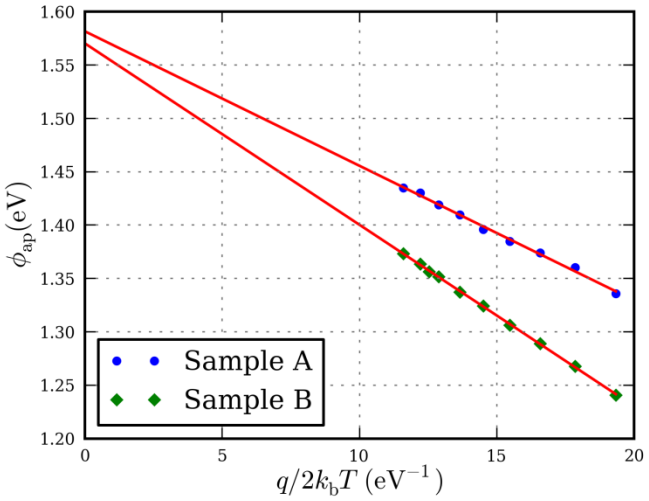

Figure 4.13 shows a plot of equation (4.8c) for samples A (blue circles) and B (green diamonds). In spite of nearly identical E_g and $\bar{\phi}_b$ values, the larger σ in sample B yields greater temperature variation in ϕ_{ap} (larger

slope). Likewise, ϕ_{ap} for sample B is lower than sample A for all temperatures because of the larger σ value.

4.6.5 Need for two "Schottky barrier heights"

An issue that presents itself with these AlInGaN diodes, and presumably any device that functions by barrier-limited transport over an inhomogeneous barrier, is the apparent dissociation between the electrostatic effects of the metal-semiconductor junction and the transport properties over the junction. Throughout the discussion, the quantities of interest that have been mentioned are the average barrier height, $\bar{\phi}_{\mathrm{b}}$, and the apparent barrier height of the diode, ϕ_{ap}, as well as the standard deviation in the barrier magnitude, σ. It has also been shown that $\bar{\phi}_{\mathrm{b}}$ is only dependent upon E_{g}, which is in turn related to the average alloy composition. It is therefore this $\bar{\phi}_{\mathrm{b}}$ that will determine the overall shape of the band diagram of the structure, as well as the built-in voltage of the junction, and other electrostatic position-average phenomena, such as two-dimensional electron gas (2DEG) density at the AlInGaN/GaN interface. While the 2DEG density may vary with position on a small scale, as alloy fluctuations take place over a small length scale, the average 2DEG density that one can measure will be due to the position-averaged $Q_{\pi}(net)$, and thus average alloy composition.

However, electron transport at a single operation temperature will be governed by $\phi_{\mathrm{ap}}(T)$. Charge carriers in barrier-limited transport will always seek out the lowest available barrier to travel over; this principle is manifested in equation (4.8c). These transport considerations must be taken into account for devices of any size, since thermal electron transport will not obey average barrier calculations. So as an addendum to the earlier section regarding material selection for device design: $\bar{\phi}_{\mathrm{b}}$ must be used as a design parameter for general band engineering, and for electrostatic effects like 2DEG density, while ϕ_{ap} and σ

must be used as design parameters for transport requirements of the device. For example, HEMT gate leakage, diode turn-on voltage at a proposed operation temperature, barrier height or current variation with temperature, and carrier confinement in quantum wells for optoelectronic devices will all be affected by ϕ_{ap} (i.e. deviations from $\bar{\phi}_b$).

In the case of optoelectronic devices, inhomogeneous barriers may be an enabling technology. Auger recombination in III-N optoelectronic devices is the most likely source of efficiency droop at high current density. Auger recombination is known to be related to the cube of the charge density in the quantum wells of the device[37,38], and quantum wells in a multiple quantum well structure are not uniformly pumped during operation. If electrons (or holes) are able to escape a quantum well with a larger electron (hole) population and enter a well with a lower carrier density, then the per-quantum well carrier concentration will decrease, and the Auger recombination rate will decrease. Since average barrier heights are the primary determinants of the potential energy distribution in the device, but distribution in the barrier height will determine the effective barrier to thermal transport, AlInGaN layers replace the GaN quantum well barriers to advantageous effect. AlInGaN can be tailored to provide the same average barrier as GaN to the InGaN quantum wells, but do so with a more severe barrier height inhomogeneity. The standard deviation in the barrier height will then promote transport between quantum wells, which would have the effect of decreasing peak carrier concentration, and ensuring that the quantum wells are utilized more uniformly and efficiently.

To compare thermionic emission in a homogeneous vs inhomogeneous quantum well structure, consider Figure 4.14. Figure 4.14a) shows the most ideal case: a homogeneous barrier and well. However, it is known that this does not reflect reality, and observations report an indium clustering effect that results in a band diagram more similar to Figure 4.14b). This

case actually shows the maximum possible thermionic emission barrier between well and barrier. An electron which thermalizes to the deepest point of the well will either have to directly overcome a large barrier, or engage in multiple energy transitions from the deepest to the shallowest part of the quantum well, and then into the barrier. This is the most likely case when GaN is used as the barrier material.

Now in Figure 4.14c), the homogeneous (GaN) barrier is replaced with an inhomogeneous (AlInGaN barrier). The result is that there are regions of barrier lowering due to the compositional fluctuations, which can result in a smaller effective barrier to electron transport out of the well. As an additional benefit, AlInGaN can reduce the magnitude of the Quantum Confined Stark Effect. Replacing GaN quantum well barriers with AlInGaN can provide two beneficial changes to device performance simultaneously.

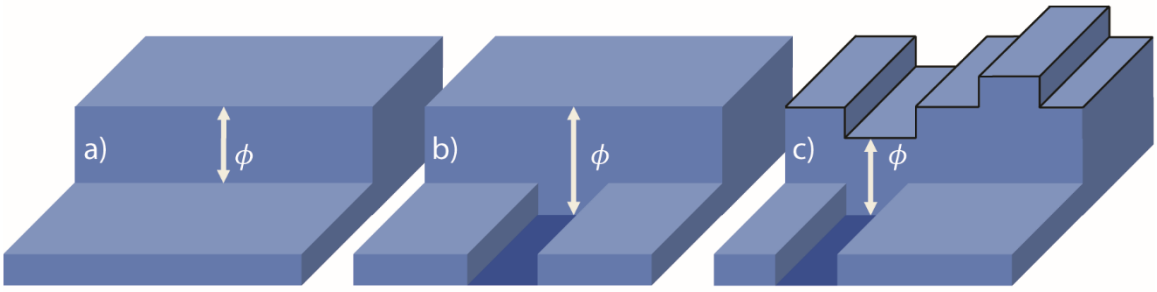

Figure 4.14a) shows a quantum well junction with its barrier with a homogeneous potential energy distribution. 4.14b) shows the case that is believed to accurately reflect state-of-the-art InGaN-GaN quantum wells. The inhomogeneity in InGaN composition results in localized wells within the overall quantum well. 4.14c) shows the replacement of GaN with AlInGaN. The inhomogeneity in AlInGaN can provide enhanced transport between quantum wells and reduce carrier concentration while maintaining overall carrier confinement.

4.7 CONCLUSIONS

The excellent agreement in $\bar{\phi}_b$ between a widely accepted empirical extraction method and the quadratic fit extraction in this study has important implications for understanding vertical current transport in III-N materials. Implications of the results of this study are many and varied:

1. The mathematical analysis does not factor in non-thermionic conduction mechanisms, thus the high quality of the fit in Figure 4.5 proves that the main conduction mechanism is thermionic emission. This is reinforced by the near-unity ideality factors of all diodes involved in this study.
2. The quadratic fit of the data is only valid for a Gaussian distribution of barrier heights. Due to the quality of the fit, it must be concluded that the SBH distribution is Gaussian and rooted in alloy composition fluctuations of the material.
3. Point 2 agrees with a related study on unipolar diodes in which the barrier was induced by the polarization sheet charge from an InGaN interlayer[35]. Thus, the effect of alloy fluctuations on current transport may be common to barrier-limited transport across any heterojunction involving low-temperature or indium-containing III-N alloy.
4. $\bar{\phi}_b$ is primarily related to the material band gap, but is determined by the position of a deep level that is connected to a surface oxide formed during processing. This may be controlled by the proper acid treatment prior to metallization and a surface passivation.

5. σ is primarily related to material composition. Consequently, the standard deviation in barrier height, and therefore $\phi_{ap}(T)$, can be designed for within the constraints of the proposed device or experiment.
6. Fermi level pinning at the surface of the AlInGaN samples is likely caused by defects in the oxide, or near the surface of the semiconductor.
7. With oxide removal by HF, the magnitude of band bending at the surface as measured by XPS, increases by a small amount (up to 0.14 eV).
8. HCl is only effective for the removal of Ga-O complexes, and yields smaller changes in ϕ_b than HF treatment.
9. Changes in the surface potential are likely caused by chlorination or fluoridation of the surface. Since HF is superior at oxide removal, passivation of surface states is more apparent, yielding a larger ϕ_b, which is closer to the value predicted by equation (4.11).
10. A^* for these AlInGaN diodes is lower than that of the GaN Schottky diode data from Figure 4.2, which is due to the presence of a surface oxide tunneling barrier in the AlInGaN samples.
11. The presence of a tunneling barrier is confirmed as a "current choke" in the AlInGaN devices, which suppresses the probability of electron transmission across the heterojunction interface, and therefore J_S.
12. Many factors can affect the extraction of A^*. Due to the nature of the fit, $\bar{\phi}_b$ and σ can still be extracted with good accuracy, even if the extracted A^* value is influenced by quantum mechanical reflections and tunneling.

4.8 REFERENCES

[1] S. Heikman, S. Keller, Y. Wu, J.S. Speck, S.P. DenBaars, and U.K. Mishra, J. Appl. Phys. **93**, 10114 (2003).

[2] A.C. Schmitz, A.T. Ping, M.A. Khan, Q. Chen, J.W. Yang, and I. Adesida, Semicond. Sci. Technol. **11**, 1464 (1996).

[3] S.M. Sze, J. Appl. Phys. **37**, 2690 (1966).

[4] S. Rajan, H. Xing, S. DenBaars, U.K. Mishra, and D. Jena, Appl. Phys. Lett. **84**, 1591 (2004).

[5] N. Ketteniss, L.R. Khoshroo, M. Eickelkamp, M. Heuken, H. Kalisch, R.H. Jansen, and A. Vescan, Semicond. Sci. Technol. **25**, 075013 (2010).

[6] Y. Liu, H. Jiang, T. Egawa, B. Zhang, and H. Ishikawa, J. Appl. Phys. **99**, 1 (2006).

[7] S.M. Sze and K.K. Ng, Phys. Semicond. Devices, 3rd Ed. John Wiley Sons, Inc.; NJ 164 (2007).

[8] Ioffe, *NSM Archive - Physical Properties of Semiconductors* (http://www.ioffe.ru/SVA/NSM/Semicond/, 2015).

[9] S. Elhamri, R. Newrock, D. Mast, M. Ahoujja, W. Mitchel, J. Redwing, M. Tischler, and J. Flynn, Phys. Rev. B **57**, 1374 (1998).

[10] U.K. Mishra and J. Singh, *Semiconductor Device Physics and Design* (Springer, Dordrecht, The Netherlands, 2008).

[11] S. Doğan, S. Duman, B. Gürbulak, S. Tüzemen, and H. Morkoç, Phys. E Low-Dimensional Syst. Nanostructures **41**, 646 (2009).

[12] L.S. Yu, Q.J. Xing, D. Qiao, S.S. Lau, K.S. Boutros, and J.M. Redwing, Appl. Phys. Lett. **73**, 3917 (1998).

[13] M. Ke, J. Vac. Sci. Technol. B Microelectron. Nanom. Struct. **13**, 1684 (1995).

[14] J.L. Freeouf, T.N. Jackson, S.E. Laux, and J.M. Woodall, Appl. Phys. Lett. **40**, 634 (1982).

[15] R.T. Tung, Phys. Rev. B **45**, 13509 (1992).

[16] R.F. Schmitsdorf, J. Vac. Sci. Technol. B Microelectron. Nanom. Struct. **15**, 1221 (1997).

[17] C. Kenney, K.C. Saraswat, B. Taylor, and P. Majhi, IEEE Trans. Electron Devices **58**, 2423 (2011).

[18] Y.-R. Wu, R. Shivaraman, K.-C. Wang, and J.S. Speck, Appl. Phys. Lett. **101**, 083505 (2012).

[19] D. Browne, B. Mazumder, Y.-R. Wu, and J.S. Speck, J. Appl. Phys. **117**, 185703 (2015).

[20] E. Ahmadi, R. Shivaraman, F. Wu, S. Wienecke, S.W. Kaun, S. Keller, J.S. Speck, and U.K. Mishra, Appl. Phys. Lett. **104**, (2014).

[21] R. Shivaraman, Y. Kawaguchi, S. Tanaka, S.P. Denbaars, S. Nakamura, and J.S. Speck, Appl. Phys. Lett. **102**, 2011 (2013).

[22] F.F. Krause, J.-P. Ahl, D. Tytko, P.-P. Choi, R. Egoavil, M. Schowalter, T. Mehrtens, K. Müller-Caspary, J. Verbeeck, D. Raabe, J. Hertkorn, K. Engl, and A. Rosenauer, Ultramicroscopy **156**, 29 (2015).

[23] R.B. Chung, J.S. Speck, and S.P. Denbaars, (n.d.).

[24] M.A. Laurent, G. Gupta, S. Wienecke, A.A. Muqtadir, S. Keller, S.P. Denbaars, and U.K. Mishra, J. Appl. Phys. **183704**, 0 (2014).

[25] E. Sakalauskas, B. Reuters, L.R. Khoshroo, H. Kalisch, M. Heuken, A. Vescan, M. Röppischer, C. Cobet, G. Gobsch, and R. Goldhahn, J. Appl. Phys. **110**, 1 (2011).

[26] D.J. Suntrup III, Transport Properties of III-N Hot Electron Transistors, University of California, Santa Barbara, 2015.

[27] Z. Lin, H. Kim, J. Lee, and W. Lu, Appl. Phys. Lett. **84**, 1585 (2004).

[28] J. Lee, D. Liu, H. Kim, and W. Lu, Solid. State. Electron. **48**, 1855 (2004).

[29] N. Subramaniyam, M. Sopanen, H. Lipsanen, C.H. Hong, and E.K. Suh, Jpn. J. Appl. Phys. **50**, 1 (2011).

[30] M.R. Spiegel, J. Schiller, and R.A. Srinivasan, *Probability and Statistics*, Third Ed. (McGraw Hill, New York, 2009).

[31] S. Chand and J. Kumar, J. Appl. Phys. **80**, 288 (1996).

[32] P.A. Tipler and R.A. Llewellyn, *Modern Physics*, 3rd ed. (W.H. Freeman, 1999).

[33] M. Higashiwaki, S. Chowdhury, B.L. Swenson, and U.K. Mishra, Appl. Phys. Lett. **97**, 1 (2010).

[34] H. Kroemer, *Quantum Mechanics: For Engineering, Materials Science, and Applied Physics* (Prentice Hall, 1994).

[35] D.J. Suntrup, G. Gupta, H. Li, S. Keller, and U.K. Mishra, Appl. Phys. Lett. **107**, 173503 (2015).

[36] D.N. Nath, Z.C. Yang, C.-Y. Lee, P.S. Park, Y.-R. Wu, and S. Rajan, Appl. Phys. Lett. **103**, 022102 (2013).

[37] Y.C. Shen, G.O. Mueller, S. Watanabe, N.F. Gardner, A. Munkholm, and M.R. Krames, Appl. Phys. Lett. **91**, 141101 (2007).

[38] K.T. Delaney, P. Rinke, and C.G. Van de Walle, Appl. Phys. Lett. **94**, 191109 (2009).

Chapter 5

SUMMARY AND FUTURE WORK

5.1 SUMMARY

The work presented in this dissertation represents the first concerted effort at UCSB toward the understanding of both the growth and electrical properties of AlInGaN materials and heterojunctions. The Chapter 2 focused on providing a comprehensive summary of the optimization processes necessary for developing the growth of a new semiconductor material system. The goal of Chapter 2 was to provide future students with a growth handbook for further development of AlInGaN growth techniques. As such, it contained a thorough discussion of compositional and morphological dependences upon user inputs to the MOCVD reactor, as well as a summary of the points of failure of the recipes. Hopefully with a clear distinction of what makes these materials unsuitable for use in solid-state devices, future researchers will be able to overcome the various trade-offs present in the growth of these materials to create future advancements in the field.

With the material growth aspect established, the rest of the dissertation was aimed toward establishing a device design toolbox. To do so, the plan was to originally characterize $Q_{\pi}(net)$, ϕ_b at metal-semiconductor junctions, and ΔE_c. Due to practical considerations and equipment failure, Chapter 3 is devoted to understanding $Q_{\pi}(net)$ and polarization in these materials, and Chapter 4 is devoted to understanding vertical transport and characterizing the Schottky barrier height to nickel. It must be left to future work to continue characterizing the SBH as a function of crystal composition, and to a wider variety of metals. It will also be left

to future work to characterize the ΔE_c of AlInGaN epilayers to GaN, but an experimental procedure will be provided as a road map to future students.

The findings of Chapter 3 were quite remarkable in the very close agreement of experimental results with theoretical calculations by Bernardini, *et al.*[1] This was a huge step forward for the quaternary design toolbox, and was successfully coupled with a commercial software suite, nextnano++[2]. It is my opinion that these material constants and this software will pave the way for future innovation in AlInGaN-based devices.

Chapter 4 was extremely far-reaching and useful for characterizing the Schottky barrier height, an electrostatic design parameter, the BHI in the Schottky barrier, which we uncovered as an important transport-related design parameter, and the role of quantum mechanical reflections as a major source of nonideality in real-world Schottky diodes. While a great deal of knowledge has been generated, and tools have been established for device engineering, the culmination of this work only scratches the surface of the promise that AlInGaN materials hold for the entire field of III-N research and development.

5.2 FUTURE WORK: MOCVD GROWTH

Two main areas for future research should be for growth on the nitrogen-polar $(000\bar{1})$ plane, and eliminating the non-crystallographic features seen embedded in the sample surfaces under highly non-equilibrium conditions. Other fruitful areas may include characterizing the effects of kinetics versus mass transport on surface morphology (particularly for thick films), and thoroughly characterizing impurity concentrations over a larger range of growth conditions. To facilitate future experiments, a summary of all of my growth recipes, including run number and brief description, are included in Appendix A.

In the case of nitrogen-polar (N-polar) growth, all work to date has been focused on achieving an acceptable surface morphology. Devices are yet out of reach. Due to extremely low surface mobility of adatoms on growing aluminum-rich surfaces at low temperature, AlInGaN films are very susceptible to hexagonal hillock formation during growth. Initial N-polar AlInGaN results revealed that it was necessary to utilize an extremely low combined $f_{TMAl} + f_{TEGa}$ flow rate of 1.72 umol/min, and a low V-III ratio of 2399 (NH3 flow rate = 1 slm) just to reduce, and not entirely eliminate, the hexagonal surface features on the film.

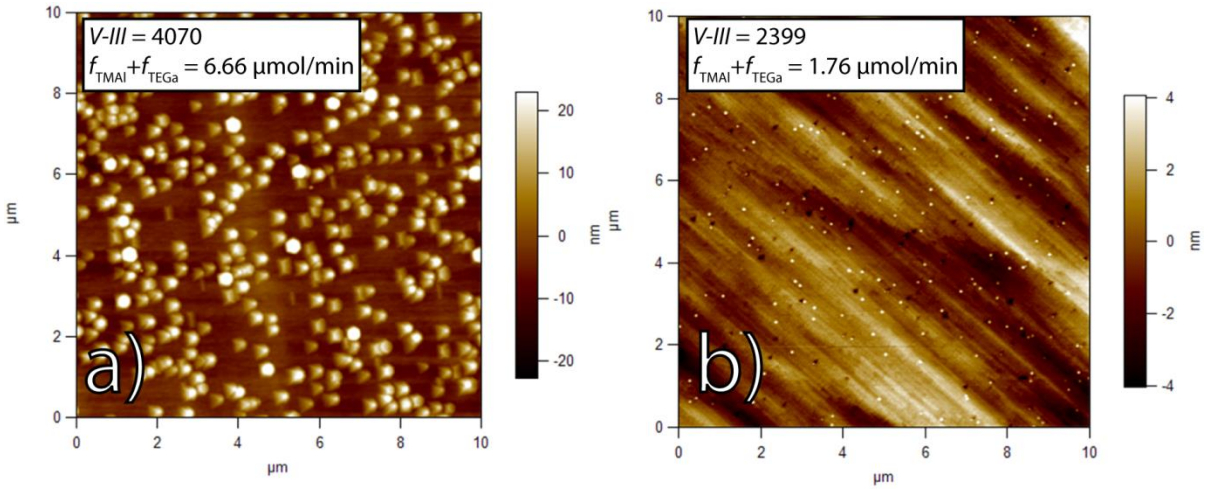

Figure 5.1 shows AFM images of inital N-polar AlInGaN growth attempts. Very low V-III ratios and low group-III injection are necessary to maintain adequate surface morphology.

Figure 5.1a shows the high density of large hexagonal features on the surface with the initial growth conditions in the inset text box. Figure 5.1b was greatly improved in terms of surface morphology, but required a shift to growth conditions that are at the limit of the acceptable region of Ga-polar growth (very low NH_3 flow). Standard N-polar InAlN growth recipes utilize 2 slm NH_3. Further improvements in surface morphology were achieved by flowing 100-200 sccm of H_2 during growth, as seen in Figure 5.2, but this came at the expense

of indium incorporation into the crystal. This cannot be a viable technology for AlInGaN growth, since the inclusion of H_2 flow impairs control of the crystal composition.

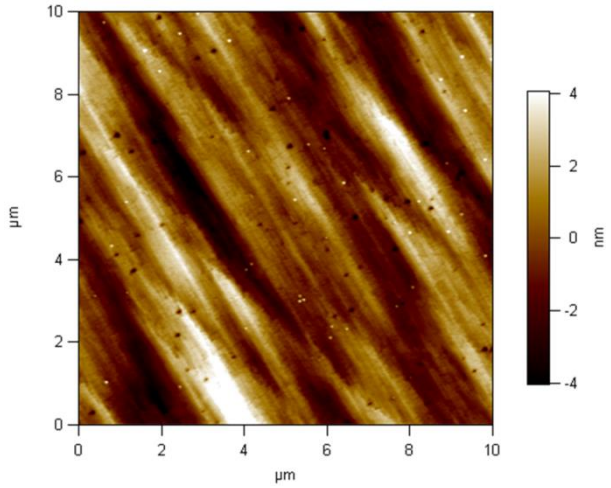

Figure 5.2 shows the improvement in surface morphology over Figure 5.1b by the addition of 100 sccm H_2 flow during growth. This unfortunately results in a penalty in successful indium incorporation into the crystal.

It was originally thought that this 75% reduction in $f_{TMAl} + f_{TEGa}$ injection would result in extremely slow growth rates, but subsequent experiments on AlGaN/GaN superlattices showed that the AlGaN growth rate was about 2x larger than identical recipes grown on Ga-polar. Consequently, the samples represented in Figure 5.1a and 5.2 had a growth rate of 0.7 nm/min, not the expected 1.4 nm/min. For reference, the most commonly used growth rate for N-polar InAlN is 0.83 nm/min, so this reduction in group-III injection was actually a move into the acceptable growth window. Efforts must be made to find acceptable growth conditions at an NH_3 flow of 2 slm.

Even if the capability to grow smooth AlInGaN is achieved, there are still strict thickness limitations with N-polar versus Ga-polar growth. This makes composition measurements of AlInGaN films infeasible with current techniques. Measuring the composition must be done with bulk techniques (RBS or SIMS), which require films that

exceed 50 nm in thickness. RBS realistically requires films that are 100 nm or greater for clear results. 50 nm is the bare minimum thickness advisable for SIMS. The problem lies in the fact that the films in Figures 5.1b and 5.2 were in the 30 nm range, but already appeared to be on the threshold of hexagonal hillock formation! Future work must focus on developing compositional measurements for thin films with less than 50 nm thicknesses.

The other area that requires concerted growth effort is the elimination or avoidance of non-crystallographic features embedded in the surface. These seem to be the first signs of failure for indium-rich growth and process robustness. As mentioned in section 2.4.3, they occur under a variety of conditions. Experiments with introducing trace amounts of H_2 gas during growth shows that this process modification can reduce or eliminate such features, but can also have a negative impact on indium incorporation into the crystal. Due to the sensitivity of these non-crystallographic features to hydrogen gas, it is believed that they are either indium-rich regions of AlInGaN, or some indium metal alloy compound. If they are indeed indium rich, then it may be possible to remove them with HCl, as is done for removing metal droplets from the surface of MBE films grown under metal-rich conditions.

Another tactic may be simple avoidance. After all, the formation of these features may not be simply a consequence of "too cold" or "too much indium" or "too high of a *V-III*". It is more realistic that the formation of these features is a consequence of too many factors during growth that simultaneously contribute to poor surface kinetics, or drive the growth very far from thermodynamic equilibrium (borrowing from the language of BCF theory[3]). Given the excellent surface morphologies of films grown in the range of 2-3 slm NH_3 flow (and a *V-III* ratio of 2000-7000), this may be considered the most optimal process window. Not only have films with high X_{AlN} and X_{InN} been demonstrated under these conditions, but the Schottky diode

sample C from Chapter 4 (grown with 3 slm NH_3) also showed truly excellent vertical transport properties. Therefore, if a wide range of compositions are accessible and electrical performance is not sacrificed, yet the formation of non-crystallographic features embedded into the surface is avoided, then the low-*V-III* ratio region of the growth space should be characterized in greater detail.

Lastly, the nature of AlInGaN relaxation should be investigated in detail. The work for this thesis focused on establishing a reliable growth regime for AlInGaN materials. However, when attempting to push the boundaries of the established growth window, relaxation effects must be dealt with. Figures 2.4 and 2.5 show compressively and lightly strained films relieve stress similarly to InGaN by roughening and V-defect formation. With a small amount of strain, it was possible to grow films of 300 nm with very small amounts of observed relaxation (Figure 2.5). However, on some films with tensile strain, the early stages of relaxation were observed as surface cracks in Figure 5.3[4,5]. Due to the ability to grow films in compressive, tensile, and no strain, different mechanisms of relaxation will be observed.

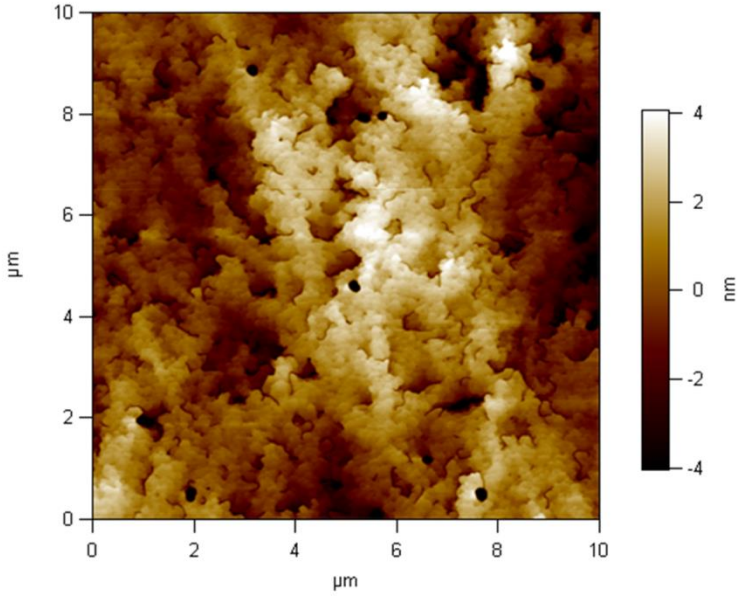

Figure 5.3. This tensile-strained AlInGaN film shows evidence of cracking in addition to V-defect formation.

5.3 FUTURE WORK: COMPLETING THE DESIGN TOOLBOX

The next logical step in AlInGaN development is to complete the electrical device design toolbox. The first step in doing so is to repeat the methodology presented in Chapter 3 over a wider range of AlInGaN compositions. Most importantly, this study must be done in a compositionally systematic order. Two separate growth series must be measured: an X_{InN} series with constant X_{AlN}, and an X_{AlN} series with constant X_{InN}. This will provide a database of $\overline{\phi}_b$ and σ values for device design and, from a scientific perspective, can be useful in distinguishing the role of indium vs aluminum on alloy and barrier height inhomogeneity.

The second step in completing the electrical design toolbox is to characterize the conduction band offset, ΔE_c, between AlInGaN and GaN as a function of alloy composition. It is especially critical to characterize this on the polar planes of the III-N material system, but previous work has shown that *C-V* analysis is very inaccurate for determining potential energy offsets in Ga-polar AlGaN/GaN heterojunctions[6]. Consequently, a hybrid approach utilizing the *C-V* analysis from Chapter 3 and the *J-V-T* analysis from Chapter 4 has been developed to calculate ΔE_c. Consider the schematic diagram in Figure 5.4. This is identical to the device structure utilized in Chapter 3 for calculating Q_π*(net)*, but this time it is going to be used for both charge (and electric field) analysis and thermionic J-V-T analysis. Thinking back to Chapter 3, equation (3.7) that there is a direct relationship between the 2DEG charge and GaN cap thickness:

$$qV_1 = \frac{q^2 n_s}{\epsilon_{GaN}} \cdot d_{GaN}. \tag{5.1}$$

Therefore, if d_{GaN} is known via MOCVD calibration, *C-V* or gated Hall measurements can be used to calculate the voltage drop V_1.

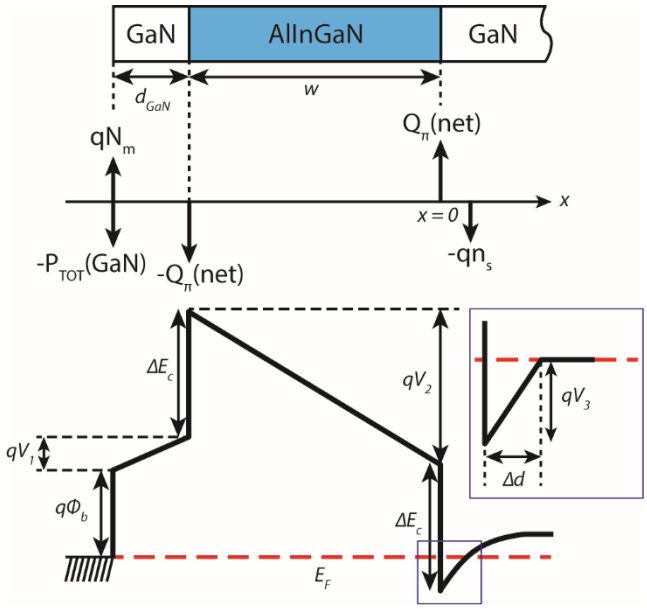

Figure 5.4. Schematic of HEMT layer structure, charge distribution and band diagram. The inset contains the two-dimensional electron gas quantum well drawn under the triangular well approximation, as is common in HEMT analysis[7].

The *J-V-T* analysis comes in to measure the total thermionic emission barrier height:

$$q\phi_{\mathrm{TE}} = q\phi_{\mathrm{b}} + qV_1 + \Delta E_{\mathrm{c}} \tag{5.2}.$$

In equation (5.2), ϕ_{b} is the Schottky barrier height to GaN, which was established at the beginning of Chapter 4, and qV_1 is the voltage drop calculated by equation (5.1). This just leaves a single unknown in the equation:ΔE_{c}.

Though the analysis is straightforward, great care must be taken with the measurements, and the following constraints must be followed:

1. The *J-V-T* analysis will only probe the maximum barrier height. For this analysis, that point must be located at the GaN/AlInGaN junction closest to the metal contact.
2. AlInGaN can take on a wide range of band gap and polarization values, but the first constraint demands that these *J-V-T* measurements be restricted to AlInGaN compositions with a positive ΔE_{c} to GaN

3. Narrow band gap AlInGaN layers are unsuitable for this because a negative ΔE_c will not appear directly in ϕ_{TE}.

5.4 FUTURE WORK: POLARIZATION

Polarization engineering with AlInGaN is an opportunity to take advantage of the unique properties of the III-N system, while simultaneously utilizing the enhanced design freedom of the AlInGaN design space. The umbrella term "polarization engineering" can encompass a wide variety of heterojunction and device designs, but it ultimately boils down to the following: using polarization charge discontinuities between III-N alloys to manipulate the band diagram of an epilayer structure. In Chapter 3.6, the concept of polarization engineering was demonstrated with near-lattice-matched graded layers designed to affect either a high-conductivity n-type layer, or a current blocking layer.

5.4.1 Graded AlInGaN layers

The examples from Chapter 3 only scratch the surface of what can be accomplished with polarization engineering in graded layers. If one considers Figure 5.5, taken from reference [6], one can see that there exist contours of constant polarization and constant band gap in the parameter space of crystal composition. Therefore, it is possible to think of a grade as a vector between the beginning and ending compositions. Then, if the grade is constructed properly, it is possible to achieve a charge-neutral grade, as in Figure 5.5a, or a grade in which the resolved polarization charge is maximized, as in Figure 5.5b. Furthermore, the grades parallel and perpendicular to the contours of constant polarization are just the limits of the

charge state of the grade. It is also possible to construct a grading vector in-between the grades in Figure 5.5, which means that the resolved $Q_{\pi}(net)$ in the grade can be controlled epitaxially.

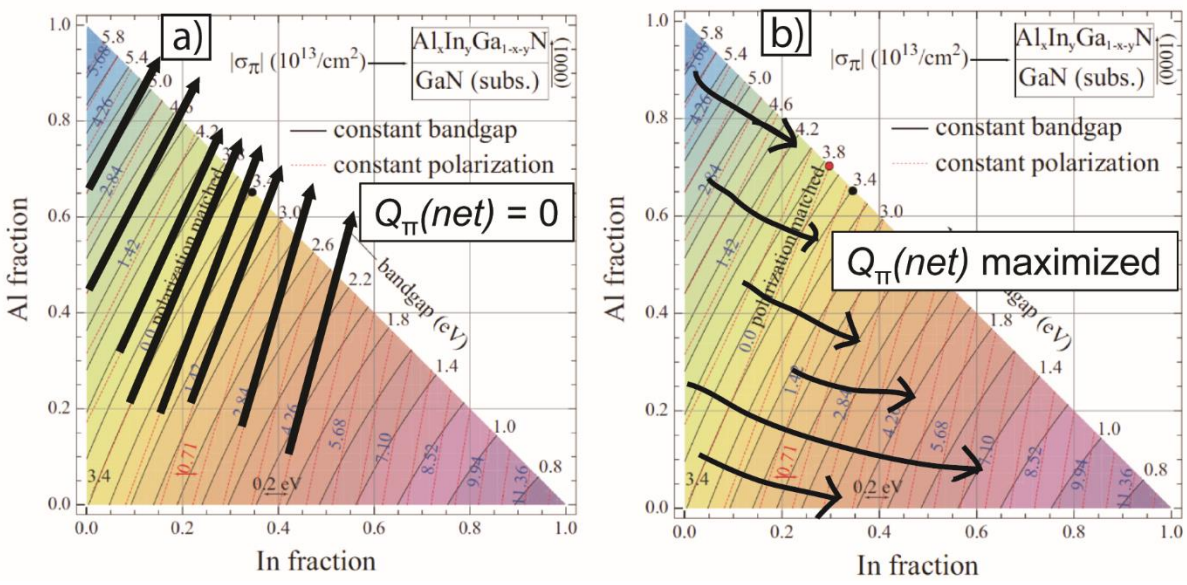

Figure 5.5 shows different methods of grading to achieve varying magnitudes of resolved net polarization charge. Figure 5.5a shows grading parallel to the contours of constant polarization, which would yield a zero-charge grade, whereas grading perpendicular to these contours would yield the maximum magnitude of space charge in the grade. Figure 5.5 is adapted from D. Jena, *et al*., Phys. Stat. Solidi A **208**, 7, 1511 (2011)[8].

5.4.2 Polarization engineering with abrupt heterojunctions

Polarization engineering is not limited to graded layers or distributions of polarization charge. Exercising control over interfacial charges can also be used to engage in band engineering with abrupt heterojunctions. First of all, from analyzing Figure 5.5, it becomes obvious that it is possible to engineer the magnitude of the 2DEG at a heterointerface. There is another way to interpret this: since $Q_{\pi}(net)$ represents a discontinuity in the electric field at the interface, careful choices in alloy composition at the heterojunction can be used to shape the electric field in a device structure. An obvious application of this is the reduction of the Quantum Confined Stark Effect in c-plane optoelectronics. This has been demonstrated, but

not optimized[9,10]. Unfortunately, the results of this experiment can be conflated with barrier height inhomogeneity effects that AlInGaN can also introduce into LED device structures, such as with the experiments from RPI. More work in this area is needed.

Another effective way to utilize polarization engineering in the nitride system is to create abrupt-interface heterojunction unipolar diodes. Bulk layer, heterojunction-based n-i-n diode structures did not prove to be successful as standalone diodes, nor as components for the Hot Electron Transistor (HET)[11,12]. A polarization diode structure proved to be very successful for HET development, and produced transistors with current gain greater than unity (Figure 5.7a)[13,14].

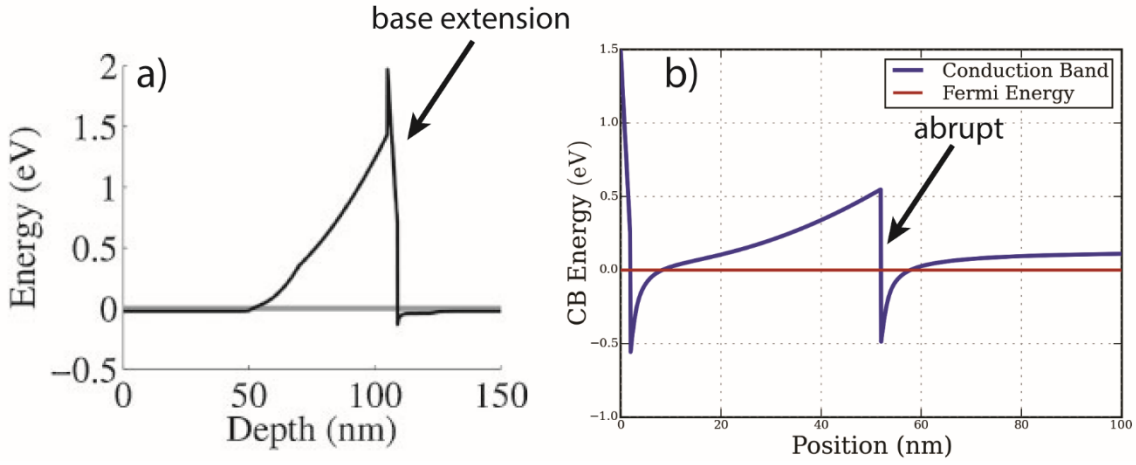

Figure 5.6a) shows the band diagram of a hot electron transistor utilizing polarization-induced barriers (figure borrowed from reference [9]). Figure 5.7b) shows an alternative diode design that utilizes the AlN polarizztion dipole near the surface of the device to shape the electric fields in the barrier material.

It is also possible to create a polarization-engineered diode where the polarization dipole is moved from the barrier-formation interface to the surface (Figure 5.7b). In this case, an InAlN layer establishes the 0.5 eV potential barrier, and an AlN dipole layer at the surface sets the electric field in the device. The AlN cap layer need not be removed, as it is possible to make very efficient Ohmic tunneling contacts at an AlN-Al metal junction. Furthermore, if

Figure 5.5 is once again referenced, a polarization-mismatched (but band gap matched) interlayer can be placed at the InAlN-GaN heterojunction to modify the 2DEG density. This consequently allows for barrier height tuning.

Recent work in our group showed that a GaN/InGaN/GaN unipolar diode exhibited larger A* values than any of the Schottky diodes presented in Chapter 4. The device structure in Figure 5.7b could therefore be an extremely high-current-density device, and could fulfill any applications that require very high on-current values.

5.5 FUTURE WORK: DEVICE ENGINEERING

Future work in AlInGaN device can be targeted in several different areas, but needs to focus on the idea of leveraging the unique or superior material properties inherent to this material system.

1. The trade-offs between the magnitude of $\bar{\phi}_b$ and σ with regard to impact on vertical transport should be investigated.
2. Utilize the HF surface treatment from Chapter 4 prior to Schottky contact (or transistor gate) metallization to eliminate the surface oxide. This will maximize $A^* \cdot \tau$, and therefore current density, of AlInGaN Schottky diodes. An experimental reference for the maximum achievable $A^* \cdot \tau$ will be a good point of reference for distinguishing applications for Schottky diodes versus n-i-n unipolar diodes.
3. The large parameter space of the AlInGaN system involving electron mobility, 2DEG density, $\bar{\phi}_b$, σ, and surface layer properties can be explored to maximize charge control and output current of HEMTs

4. Of particular interest is maximizing $n_s \cdot \mu$ (charge – mobility product) for both Ga- and N-polar AlInGaN HEMTs. This can help determine if they will be competitive versus AlGaN and/or InAlN HEMTs.
5. Quaternary alloys and graded layers can be a useful vehicle for understanding dopant incorporation and activation in ultra-wide band gap semiconductors.

5.6 FUTURE WORK: HOPES AND DREAMS

This section is devoted to the riskiest, but potentially most interesting ideas I have for the material system. These concepts are impractical for implementation in the near future, but could be very interesting areas for long-term study. A dream for the future of the III-N system is the development of a native substrate. This area has been extremely active in recent years toward the development of bulk GaN boules. However, my desire is for bulk quaternary layers. A bulk substrate with a band gap of E_g ~ 3.8 eV (same as $Al_{0.2}Ga_{0.8}N$) and a lattice constant of a ~ 3.23Å (same as $In_{0.1}Ga_{0.9}N$) would be an extremely versatile substrate (Figure 5.9).

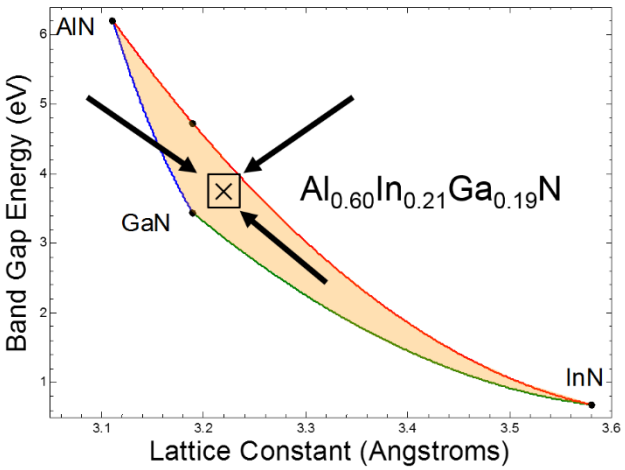

Figure 5.7 the ideal native substrate for the III-N material system should enable heterojunctions of all kinds: positive and negative ΔE_c, both senses of strain, and both senses of polarization charge.

It could still yield HEMT structures with a (tensile-strained) GaN channel, and would also be extremely useful for the development of long-wavelength optoelectronic devices. Furthermore, it would represent the maximization of design freedom for heterojunctions in the III-N material system, which has been a recurring theme of this dissertation. As Prof. DenBaars has pointed out, there are substrate lift-off technologies that could be applied to a structure such as this[15]. Since bulk growth of AlInGaN alloys is an unlikely reality, these substrates could be grown heteroepitaxially by MOCVD, and then lifted off as their own freestanding substrates.

Another interesting research direction for AlInGaN is in a class of devices that has fascinated me for some time: the quantum cascade laser. It is a unipolar laser that requires large energy transitions between quantum wells for photon emission (Figure 5.10). On paper, this is an extremely attractive device for the III-N system, as it would be convenient to avoid p-type material for light emitters, and the material system already demonstrates very deep quantum wells. Proof-of-concept of a nitride QC device has been demonstrated in the 1-3 THz frequency range (149 microns)[16].

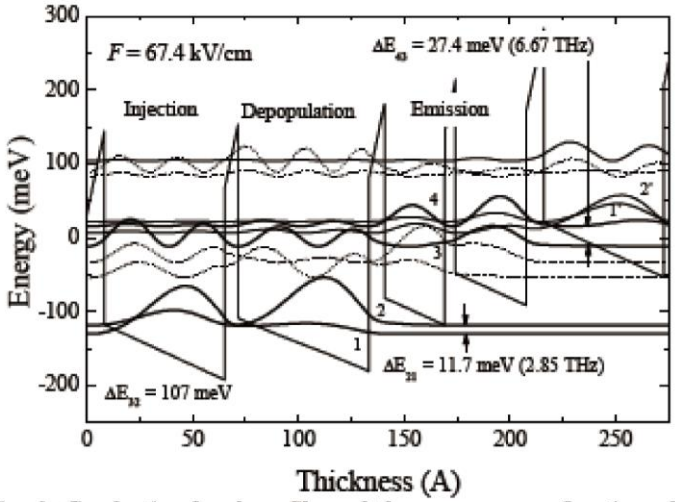

Fig. 1. Conduction band profile and the square wave functions for a GaN/AlGaN QC structure grown on an AlN template emitting at 6.67 and/or 2.85 THz under a biased external electric field of 67.4 kV/cm.

Figure 5.8 shows the sophisticated band engineering and many heterojunction interfaces required to fabricate a quantum cascade device. This image is taken from reference [14], a device demonstrated by Terashima, *et al*. at the 2013 Conference on Lasers and Electro-Optics Pacific Rim (CLEO-PR)[16].

However, the current devices are extremely low power, and the desired frequency range for such devices would be much higher – in the mid-infrared, for example. Current devices also utilize AlGaN/GaN quantum wells, which is a significant design inhibitor. Quantum cascade lasers require very sophisticated band engineering, and often quite thick layer stacks. The value of AlInGaN/GaN alloys here is unquestionable. They could be incorporated for a wide range of band gap values while maintaining lattice-matching (or very slight strain) to the GaN substrate. This allows for the engineering of electrical transitions in these devices, and could be a huge springboard forward for III-N quantum cascade lasers.

5.7 FINAL THOUGHTS

After having the opportunity to understand the growth and characterize the electrical properties of AlInGaN materials and heterojunctions, I believe that proper utilization of these materials will be a major component of the future of III-N device engineering. Future researchers could have the opportunity to improve upon the performance of already-existent device types, such as with the promising application of AlInGaN barriers to HEMTs, but there is also enormous potential for developing novel devices, or multi-device systems. The AlInGaN system was too young during the years of my PhD research for me to engage in sophisticated device engineering. I believe that the time is near for a concerted effort to be put forth in AlInGaN-based devices, and I hope that the information contained in this thesis will prove useful for the next students.

5.8 REFERENCES

[1] F. Bernardini and V. Fiorentini, Phys. Rev. B **64**, 085207 (2001).

[2] S. Birner, *Nextnano - Semiconductor Software Solutions* (http://nextnano.com/, 2015).

[3] W.K. Burton, N. Cabrera, and F.C. Frank, Philos. Trans. R. Soc. A Math. Phys. Eng. Sci. **243**, 299 (1951).

[4] H. Li, S. Keller, S.P. DenBaars, and U.K. Mishra, Jpn. J. Appl. Phys. **53**, 095504 (2014).

[5] J.A. Floro, D.M. Follstaedt, P. Provencio, S.J. Hearne, and S.R. Lee, J. Appl. Phys. **96**, 7087 (2004).

[6] C.A. Hurni, Characterization of Polar, Semi-Polar, and Non-Polar P-N Homo and Hetero-Junctions Grown by Ammonia Molecular Beam Epitaxy, University of California, Santa Barbara, 2012.

[7] U.K. Mishra and J. Singh, *Semiconductor Device Physics and Design* (Springer, Dordrecht, The Netherlands, 2008).

[8] D. Jena, J. Simon, A. Wang, Y. Cao, K. Goodman, J. Verma, S. Ganguly, G. Li, K. Karda, V. Protasenko, C. Lian, T. Kosel, P. Fay, and H. Xing, Phys. Status Solidi Appl. Mater. Sci. **208**, 1511 (2011).

[9] S.-H. Park and D. Ahn, IEEE J. Sel. Top. Quantum Electron. **19**, 1901308 (2013).

[10] M.F. Schubert, J. Xu, J.K. Kim, E.F. Schubert, M.H. Kim, S. Yoon, S.M. Lee, C. Sone, T. Sakong, and Y. Park, Appl. Phys. Lett. **93**, (2008).

[11] G. Gupta, M.A. Laurent, J. Lu, S. Keller, and U.K. Mishra, Appl. Phys. Express **7**, 014102 (2014).

[12] G. Gupta, M. Laurent, D.J. Suntrup, E. Acuna, S. Keller, and U.K. Mishra, IEEE Electron Device Lett. **36**, 23 (2015).

[13] G. Gupta, M. Laurent, H. Li, D.J. Suntrup, E. Acuna, S. Keller, and U. Mishra, in *72nd Device Res. Conf.* (IEEE, 2014), pp. 255–256.

[14] G. Gupta, E. Ahmadi, K. Hestroffer, E. Acuna, and U.K. Mishra, IEEE Electron Device Lett. **36**, 439 (2015).

[15] S.P. Denbaars and M.A. Laurent, (2015).

[16] W. Terashima and H. Hirayama, Conf. Lasers Electro-Optics Pacific Rim 8 (2013).

Appendix A

SUMMARY & DESCRIPTION OF MAJOR AlInGaN RECIPES

V130221AA	InAlN calibration based on V120406BA. Part of temperature series for X_{InN}. I_{set} = 58.6.
V130221BA	InAlN calibration. Temperature series. I_{set} = 59.6
V130221CA	InAlN calibration. Temperature series. I_{set} = 60.6
V130303BA	Lattice-matched InAlN. I_{set} = 61.63. X_{InN} too high because half-wafer susceptor runs cold.
V130303CA	AlGaN @ InAlN conditions w/TEGa. I_{set} = 61.13.
V130310AA	Repeat previous, increase growth time 2x. XRD --> 20.6 nm. Relaxed in AFM.
V130310BA	From previous, increase TEGa DD 2x. 21.4 nm w/ 24% Al. Film not relaxed.
V130310CA	LT-AlGaN/GaN superlattice calibration sample. Modified V130310BA to be a superlattice.
	Note: since binary growth rates scale linearly w/flow, and there are no pre-reactions, we can use the MO4 AlGaN superlattice calculator.
V130318AA	AlGaN TMAl flow rate series. ~24% Al
V130318BA	AlGaN TMAl flow rate series. Extensive cracking.
V130318CA	AlGaN TMAl flow rate series. Lowest composition.
V130318DA	AlGaN TMAl flow rate series. ~36% Al. Partial relaxation?

V130319AI	InGaN calibration. Based on InAlN conditions. I_{set} = 58. TEGa molar flow for ~1 nm/min GR
V130402AI	InGaN calibration. Based on V130319AI. Doubled TMIn flow. Only slight increase in X_{InN}
V130402AI	InGaN calibration. Increased TMIn molar flow to 480 sccm. No change in X_{InN}
V130402CI	From V130319AI, increased TEGa molar flow 2x. X_{InN} increased to 8.25%, GR @ 2.33. Morphology OK. Probably too fast for films w/high X_{AlN}
V130403AI	From V130319AI, decreased TEGa molar flow 2x. X_{InN} stayed at 5%, GR didn't change either. Weird.
V130411AI	From V130319AI, decreased TMIn by 2x. No real change in X_{InN} --> we must be in the indium incorporation saturation regime.
V130411CQ	**FIRST QUATERNARY GROWTH. N-polar co-load all hexagoney.**
V130423AA	AlGaN calibration check.
V130423CQ	**SECOND QUATERNARY. Repeated V130411CQ, grew it thicker for RBS analysis. 152 nm.**
V130507AQ	Thickness series with V130423CQ and V130411CQ. 302 nm.
V130508AQ	**Using V130423CQ as reference: TMAl flow rate series. Increased TMAl flow.**
V130508BQ	Using V130423CQ as reference: TMAl flow rate series. Increased TMAl flow to 3 *μmol*/min. Relaxed.
V130508CQ	**Using V130423CQ as reference: TMAl flow rate series. TMAl = 1.53 *μmol*/min**

V130513AQ	From V130508BQ, halved the growth time. STILL RELAXED.
V130513BQ	**Using V130508AQ as reference: TEGa growth series. This has double the TMAl, TEGa flow of V130423CQ, 2x growth rate, same X_{AlN}.**
V130513CQ	Using V130508AQ as reference: TEGa growth series. Decreased TEGa flow to 3.072 μmol/min
V130514AQ	**Using V130508AQ as reference: temperature series. Decreased I_{set} by 1 amp to 58.87.**
V130514BQ	Using V130508AQ as reference: temperature series. Increased I_{set} by 1 amp to 60.87.
V130603AQ	**Quaternary Schottky diode. X_{AlN} = .34; X_{InN} = 0.12**
V130603BQ	Quaternary Schottky diode. X_{AlN} = .44; X_{InN} = 0.12. TMAl/TEGa ratio series.
V130607AQ	**Quaternary Schottky diode. X_{AlN} = 0.54; X_{InN} = 0.11. TMAl/TEGa ratio series. Also part of V-III ratio series. NH_3 = 4slm**
V130607BQ	Quaternary Schottky diode. V-III series. Too hot: T increased when decreasing NH_3. NH_3 = 2 slm.
V130608AQ	Quaternary Schottky diode. V-III series. From previous, decreased temp.
V130608AQ	Quaternary Schottky diode. V-III series. NH_3 = 1 slm. ELECRICAL SHORT.
V130610AQ	Quaternary Schottky diode V-III series. NH_3 = 5 slm. ELECTRICAL SHORT. BAD MORPHOLOGY.
V130610BQ	**n-GaN regrowth for SIMS analysis**
V130615AQ	Final temperature series point. Quaternary Schottky diode. I_{set} = 61.87.

V130615BQ	Quaternary Schottky diode. V-III series. NH_3 = 3 slm. Did not conserve gas flow - composition is not right. EXCELLENT DIODE.
V130707ANQ	**N-polar quaternary. 2 slm NH_3, using group III flow from V130423CQ. HEXAGONS.**
V130712BNQ	N-polar quaternary. From previous, halve NH_3, TMAl and TEGa. HEXAGONS (but smaller).
V130712BNQ	From previous: drop N_2 flow to decrease total flow. No effect.
V130714ANQ	From V130712BNQ: halve TEGa flow. Slower growth rate (and thinner film) --> very small hexagons (but they are still there)
V130715BNQ	From previous: decreased total flow by 2slm (N_2). Hexagons are more sparse, but larger.
V130719ANQ	From V130714ANQ: include 100 sccm H_2. ELMINIATED HEXAGONS, BUT DECREASED X_{InN}.
V130720AQ	Repeat of V130608AQ. Slower growth rate.
V130725AH	**AlInGaN HEMT for $Q_{\pi}(net)$ calculation. X_{AlN} = 0.54; X_{InN} = 0.12. 30 nm. Based on V130607AQ. Slower GR to try to decrease carbon and oxygen incorporation.**
V130725BH	AlInGaN HEMT. From previous: decrease growth time for 15 nm quaternary.
V130726AH	AlInGaN HEMT. 5 nm channel. NO CHARGE.
V130726BH	AlInGaN HEMT. ~10 nm channel. WE HAVE CHARGE.
V130727AH	AlInGaN HEMT. ~22 nm (actually 18.5)
V130728AH	AlInN HEMT. No AlN interlayer. NO MODULATION.

V130829AQ	**AlInGaN V-III series. 5 slm NH_3, 200 sccm H_2 during last 1/3 of layer. Decreased metal inclusion size/density. MUST BE INDIUM-RELATED.**
V130922BQ	AlInGaN V-III series. 5 slm NH_3, 200 sccm H_2 during entire layer. Decreased metal inclusion size/density. Also decreased X_{InN}. MUST BE INDIUM-RELATED.
V131001AQ	AlInGaN HEMT. 26 nm.
V131008BH	AlInGaN HEMT. 15.4 nm.
V131009BH	AlInGaN HEMT. 12.5 nm.
V131023AQ	Quaternary retrograde.
V131023BNA	LT-AlGaN/GaN superlattice on N-polar
V131024AH	AlInGaN HEMT. 18 nm quaternary, 1 nm AlN. Mobility = 1239.
V131024BNQ	Quaternary superlattice based on V131023BNA. XRD peaks are shifted to greater compressive strain.
V140218BQ	Quaternary calibration. Repeat of V130423CQ.
V140411BQ	Quaternary retrograde with doping. Eg still dips below GaN
V140414AQ	Emitter-base HET diode w/quaternary grade. Sample looked yellow. Poor morphology.
V140421AQ	Quaternary retrograde with temperature ramp. Better composition and Eg profile.
V140422AQ	Quaternary unipolar diode w/improved grade. Poor surface morphology --> over-doping with silicon?

V140423AQ	Quaternary unipolar diode with better doping and shorter growth interrupts. Still rough.
V140423BQ	Quaternary unipolar diode. Decrease NH_3 flow. Still rough.
V140618AA	LT-AlGaN superlattice calibration
V140930BA	Graded AlInGaN w/recalibration. However there was a strong compositional inhomogeneity w/wafer position (radially)
V141031CQ	Quaternary Schottky diode w/low temp. I_{set} = 55.75. Poor morphology due to hemispherical hillocks.
V141106BQ	AlInGaN diode temperature series.
V141203DQ	AlInGaN calibration to V130615BQ - very good match.
V141206AQ	AlInGaN diode - hemispherical hillocks
V141206BQ	AlInGaN diode - hemispherical hillocks
V141208AG	n-GaN - hemispherical hillocks
V150609AQ	Quaternary polFET. Graded (not retrograded) quaternary. Low charge/mobility.